

Doctoral Dissertation

Study on umbilical artery blood signal analysis and classification

臍帶動脈血流信号解析と分類に関する研究

March 2024

令和6年3月

Yu Kaijun

俞凱君

Graduate School of Science and Technology for Innovation

Yamaguchi University

山口大學創成科學研究科

Contents

| | |
|---|-----------|
| ABSTRACT | 1 |
| Chapter 1 Introduction | 1 |
| 1.1 Background | 1 |
| 1.2 Overview | 3 |
| 1.2.1 Conventional analysis methods of umbilical artery blood signal | 3 |
| 1.2.2 Study of nonlinear analysis of umbilical artery blood signal | 4 |
| 1.2.3 Current state of medical diagnosis research based on machine learning | 5 |
| 1.3 Aim and organization of this dissertation | 6 |
| 1.4 References | 7 |
| Chapter 2 Acquisition of umbilical artery blood signal | 11 |
| 2.1 Fetal Hemodynamics | 11 |
| 2.1.1 Fetal blood circulation | 11 |
| 2.1.2 Placental development process | 12 |
| 2.1.3 Umbilical cord structure and characteristics | 13 |
| 2.2 Umbilical artery wave dynamics | 14 |
| 2.2.1 Constant pressure-flow relationship | 15 |
| 2.2.2 Poiseuille's pressure-flow relationship | 16 |
| 2.2.3 Input impedance | 16 |
| 2.2.4 Pulse wave propagation and wave velocity | 17 |
| 2.3 Conventional diagnostic parameters of umbilical artery blood | 18 |
| 2.4 Detection of umbilical artery blood signal | 22 |
| 2.4.1 Doppler effect of moving sound sources | 22 |
| 2.4.2 Ultrasonic Doppler velocimetry | 23 |
| 2.4.3 Detection of umbilical artery blood signal | 25 |
| 2.5 Acquisition of umbilical artery blood signal | 26 |
| 2.5.1 Acquisition equipment | 26 |
| 2.5.2 Signal acquisition process | 27 |
| 2.5.3 Ethics | 29 |

| | |
|--|-----------|
| 2.5.4 Database of umbilical artery blood signal | 29 |
| 2.6 Problems with conventional parameters | 31 |
| 2.7 Summary | 32 |
| 2.8 References | 33 |
| Chapter 3 Fractal characterization of umbilical artery blood signal | 35 |
| 3.1 Foundations of fractal theory | 35 |
| 3.1.1 Definition of fractal | 35 |
| 3.1.2 Classical fractal structure | 36 |
| 3.1.3 Fractal dimension | 38 |
| 3.2 Fractal dimensions of umbilical artery blood signal | 45 |
| 3.2.1 Box dimensional analysis of umbilical artery blood signal | 45 |
| 3.2.2 Correlation dimensional analysis of umbilical artery blood signal | 49 |
| 3.3 Signal analysis of umbilical artery blood based on Hurst index | 55 |
| 3.3.1 Hurst Index | 56 |
| 3.3.2 R/S analysis method | 56 |
| 3.3.3 A comparative study of R/S classic analysis method | 58 |
| 3.3.4 Hurst exponent analysis of umbilical artery blood signal | 61 |
| 3.4 Summary | 63 |
| 3.5 References | 64 |
| Chapter 4 Chaotic characterization of umbilical artery blood signal | 66 |
| 4.1 Chaos theory | 66 |
| 4.1.1 Origin and development of Chaos | 66 |
| 4.1.2 Basic concept of Chaos | 68 |
| 4.2 Phase space reconstruction | 68 |
| 4.2.1 Takens' theorem and reconstructed phase space | 69 |
| 4.2.2 Determination of phase space reconstruction parameters | 69 |
| 4.3 Chaotic characteristic recognition of umbilical artery blood signal | 71 |
| 4.3.1 Phase diagram method | 71 |
| 4.3.2 Maximum Lyapunov Exponent method | 78 |
| 4.3.3 Box plot and ROC of MLE | 80 |
| 4.4 Summary | 81 |
| 4.5 References | 82 |

| | |
|--|------------|
| Chapter 5 Composite multi-scale feature extraction and diagnosis for umbilical artery blood | 85 |
| 5.1 Introduction to machine learning..... | 85 |
| 5.2 Datasets and classifiers | 86 |
| 5.2.1 Definition | 86 |
| 5.2.2 Classifier performance | 86 |
| 5.3 Multi-scale feature extraction and diagnosis for umbilical artery blood signal | 88 |
| 5.3.1 SVM | 88 |
| 5.3.2 SVM classification of umbilical artery blood signal with conventional parameters | 93 |
| 5.3.3 PSO-SVM classification of umbilical artery blood signal with conventional parameters | 94 |
| 5.3.4 PSO-SVM classification of umbilical artery blood signal with nonlinear parameters | 96 |
| 5.4 Summary | 97 |
| 5.5 References..... | 97 |
| Chapter 6 Conclusions and prospects | 99 |
| 6.1 Conclusions | 99 |
| 6.2 Prospects | 100 |
| Acknowledgment | 101 |

Abstract

In China, there are about 800,000 congenital diseases among 20 million newborns, of which nearly 200,000 fetuses have serious defects or diseases. The birth of these sick fetuses brings serious economic burden and social problems to the family and even the society. It is therefore important to carry out early fetal monitoring in order to detect fetal defects and diseases as early as possible. Umbilical artery blood signals contain important information about fetal growth and development, reflecting various problems during pregnancy, such as intrauterine growth retardation (IUGR), hypoxia and maternal hypertension, which can be determined by umbilical artery blood signals. Therefore, the analysis of umbilical artery blood signals is important for prenatal monitoring and fetal health status diagnosis.

The acoustic spectral parameter method is a conventional technique for analyzing the umbilical artery blood signals and consists of three parameters that serve as clinical diagnostic criteria: resistance index (RI), pulsatility index (PI) and maximum systolic/end-diastolic umbilical flow velocity (S/D). However, these parameters ignore phase properties of the signal, such as phase delay, phase frequency and phase mode, and focus only on the fundamental statistical parameters of blood velocity, such as maximum, minimum and mean values. This may lead to clinical misdiagnosis.

Umbilical artery blood signals have complicated structures and nonlinear characteristics in addition to changes in signal amplitude. This paper presents a comprehensive new approach for characteristics parameter extraction and classification of umbilical artery blood signals using fractal theory and Chaos theory in order to handle these complex structures and nonlinear properties of the signal. First, by focusing on the fractal characteristics of umbilical artery blood signals, the fractal dimension (BD) and the correlation dimension (CD) are obtained to verify that BD is positively correlated with the gestational week and CD is effective in discriminating normal from abnormal. Next, we obtain the maximum Lyapunov exponent (MLE) of the chaotic characteristics of umbilical artery blood time series, and verify its effectiveness in distinguishing normal signals from abnormal signals. Finally, a diagnostic model is proposed by applying particle swarm optimization-support vector machine (PSO-SVM) to the conventional feature parameters (RI, PI, S/D) and newly obtained parameters (BD, CD, MLE) to classify and diagnose the umbilical blood signals in the four statuses (normal, oligohydramnios, umbilical cord around neck, fetal malposition).

This doctoral dissertation consists of 6 chapters.

Chapter 1 introduces the background and means of umbilical artery blood study as well as reviewing the current research situation. The outline of this dissertation is also given.

In chapter 2, the fundamentals of fetal hemodynamics are described. The clinical significance and

normal reference values of umbilical artery blood signal parameters are outlined. Details of the umbilical artery signal acquisition equipment, data classification and acquisition process are explained.

In chapter 3, the fractal dimension box-counting method (BD) and the correlation dimension (CD) are used to investigate the nonlinear characteristics of the umbilical artery blood signals based on fractal theory. First, the BD of the umbilical artery blood signals is calculated and the fractal characteristics of the signals are analyzed. Results show a positive relationship between the fractal dimension of umbilical artery blood signals and gestational weeks. Abnormal and normal umbilical artery signals are then classified into abnormal group and normal group. The Grassberg-Procaccia algorithm (GP algorithm) is used to calculate and analyze the CD of the two groups. The overall CD of normal umbilical artery blood signals is greater than that of abnormal signals. CD is significantly better at discriminating the normality of the umbilical artery blood signal compared to conventional parameters. Furthermore, the Hurst exponent of umbilical artery blood signal is calculated and analyzed by Lo method. The results show that umbilical artery blood signal belongs to non-stationary signal and show obvious “1/f fluctuation” characteristics.

In chapter 4, chaotic phase space diagram method and maximum Lyapunov exponent (MLE) are used to determine the chaotic characteristics of umbilical artery blood signals from qualitative and quantitative perspectives. The attractor reconstruction of umbilical artery blood signals is performed in three-dimension (3D) and two-dimension (2D) phase space. The results show that the chaotic phase diagram of the time series for abnormal umbilical artery signals show a jumbled “ball of wool” state and the chaotic “shape” appears to converge. Application of the receiver operating characteristic (ROC) curve to the obtained maximum Lyapunov exponent (MLE) shows that the rate of discrimination of normality of the umbilical artery blood signal is significantly better than the conventional feature parameters.

In chapter 5, an artificial intelligent classifier is proposed to classify the four states of umbilical artery blood signals (normal, oligohydramnios, umbilical cord around neck and fetal malposition). The support vector machine (SVM) classifying method is constructed based on the conventional parameters, S/D, PI and RI. The particle swarm optimisation-support vector machine (PSO-SVM) classifier is also constructed using the fractal dimension (BD), correlation dimension (CD) and maximum Lyapunov exponent (MLE) derived in Chapters 3 and 4 as feature parameters. The results of the classification tests show that the PSO-SVM classifier is more accurate, confirming the usefulness and effectiveness of the proposed classification method.

In Chapter 6, summary of this dissertation and future work are described.

要 旨

中国では、2000万人の新生児のうち約80万人に先天性疾患があり、そのうち20万人近くの胎児に深刻な欠陥や病気がある。これらの病気の胎児の誕生は、家族、さらには社会に深刻な経済的負担と社会問題をもたらす。したがって、胎児の欠陥や病気をできるだけ早期に発見するために、早期胎児モニタリングを実施することが重要である。臍帯動脈血信号には胎児の成長と発育に関する重要な情報が含まれており、子宮内発育遅延(IUGR)、低酸素症、母体の高血圧など妊娠中の様々な問題を、臍帯動脈血信号によって判断することができる。したがって、臍帯血信号の分析は、出生前のモニタリングと胎児の健康状態の診断にとって重要である。

超音波を用いた音響スペクトルパラメータ法は、臍帯動脈の血液信号を分析するための従来の手法であり、臨床診断基準となる3つのパラメータ、抵抗指数(RI)、脈動指数(PI)、および収縮期/拡張期臍帯血流速の最大値(S/D)から構成される。しかし、これらのパラメータは、位相遅延、位相周波数、位相モードといった信号の位相特性を無視し、最大値、最小値、平均値といった血流速度の基本的な統計パラメータのみに焦点を当てている。これは臨床的な誤診をもたらすことがある。

臍帯動脈の血液信号には、信号の振幅揺らぎに加えて、信号の複雑な構造と非線形特性も含まれている。本研究では、これらの信号の複雑な構造と非線形特性に着目し、フラクタル理論とカオス理論を用いて、胎児臍帯動脈血の測定信号に対して特徴パラメータの抽出および分類を包括的に行う新しい方法を提案する。まず、臍帯血信号のフラクタル特徴に着目し、フラクタル次元(BD)と相関次元(CD)を求め、BDは妊娠週数と正の相関があり、CDは正常と異常の判別に有効であることを検証する。次に、臍帯血時系列のカオスの特徴に対して、最大リャプノフ指数(MLE)を求め、同様に正常と異常判別への有効性を確認する。最後に、従来の特徴パラメータ(RI, PI, S/D)と新たに得られたパラメータ(BD, CD, MLE)に対して粒子群最適化-サポートベクターマシン(PSO-SVM)を適用し、4つの状態(正常、羊水過少、首周りの臍帯、胎児位置異常)における臍帯血信号の分類・診断モデルを提案する。

この博士論文は6章からなる。

第1章では、臍帯血研究の背景と手段を紹介し、現在の研究状況を概説する。また、本論文の概要を述べる。

第2章では、胎児血行動態の基礎を述べ、臍帯血信号パラメータの臨床的意義と正常基準値を概説する。臍帯動脈信号収集装置、データ分類、収集プロセスを概説する。

第3章では、フラクタル理論に基づき、フラクタル次元ボックスカウント法(BD)と相関次元(CD)を用いて臍帯動脈血信号の非線形特性を調べる。まず、臍帯血信号のフラクタル次元を計算し、その信号のフラクタル特性を解析する。結果として、臍帯動脈血信号のフラクタル次元と妊娠週数との間には正の相関があることが示された。次に、異常な臍帯動脈信号と正常な臍帯動脈信号を異常群と対照群に分類した。Grassberg-procaccia アルゴリズム(G-P アルゴリズム)を用い

て、2つのグループのCDを計算・分析する。正常臍帯血流信号のCDは異常信号のCDよりも全体的に大きい。CDは、従来の特徴パラメータに比べ、臍帯血流信号の正常性判別に有意的に優れている。さらに、臍帯血流信号のハースト指数をLo法により計算・解析する。その結果、臍帯血流信号は非正常信号に属し、明らかな「1/fゆらぎ」特性を示すことがわかった。

第4章では、カオス位相空間図法と最大リアプノフ指数(MLE)を用いて、臍帯血信号のカオス特性を定性的・定量的に決定する。臍帯動脈血信号のアトラクター再構成を3次元(3D)および2次元(2D)位相空間で行う。その結果、異常な臍帯動脈信号の時系列のカオス位相図は、「毛糸玉」のようなごちゃごちゃした状態を示し、カオスの「形」は収束するように見えることがわかった。求めた最大リアプノフ指数(MLE)に対してROC曲線(ROC)を適用した結果、臍帯血流信号の正常性を識別する率が従来の特徴パラメータよりも有意に優れていることを示された。

第5章では、臍帯血信号の4つの状態(正常、絨毛膜羊膜症、臍帯頸部周囲、胎児位置異常)を分類する人工知能分類法を提案する。従来の特徴パラメータであるS/D、PI、RIに対してサポートベクターマシン(SVM)による分類器を構築する。また、第3章と第4章で導出したフラクタル次元(BD)、相関次元(CD)、最大リアプノフ指数(MLE)を特徴パラメータとして、粒子群最適化-サポートベクターマシン(PSO-SVM)分類器を構築する。分類テストの結果から、PSO-SVM分類器の方が精度高く、本提案の分類法の有用性と有効性が確認された。

第6章では、本論文のまとめと今後の課題について述べる。

Chapter 1

Introduction

1.1 Background

In China, of the nearly 20 million newborns born each year, about 800,000 are born with congenital diseases, and nearly 200,000 of them have serious defects and diseases [1]. The birth of these sick fetuses brings serious economic burdens and social problems to families and even to society.

In 2022, China's neonatal mortality rate will be 3.1 per 1,000 and maternal mortality rate will be 0.157 per 1,000[2]. The Chinese government aims to reduce the national maternal mortality rate to below 0.12 per 1,000 and the national neonatal mortality rate to below 3.0 per 1,000 by 2030 respectively [3].

World Health Organization (WHO) has issued two reports which state two points, the first being high maternal mortality in undeveloped countries [4], and the second being stalling progress in improving maternal and newborn survival [5].

At present, the main methods of real-time dynamic evaluation of intrauterine development and health status of the fetus for fetal monitoring are fetal cardiac monitoring, ultrasonography, fetal oxygen saturation monitoring, fetal scalp stimulation test and observation of amniotic fluid properties [6].

The umbilical cord is the only link between mother and fetus, and its umbilical artery blood signal contains a wealth of maternal and infant information, and its blood status can reflect fetal development, maternal blood pressure and intrauterine hypoxia [7-8]. Therefore, the study and analysis of the characteristics of the umbilical artery blood signal can achieve timely and dynamic monitoring of fetal health status, and its application to prenatal fetal monitoring is of great theoretical and social significance in predicting and reducing the birth rate of fetuses with hereditary and congenital diseases.

The current method of clinical monitoring of the fetus is Doppler ultrasonography of the umbilical artery [9]. Doppler ultrasound-based signal acquisition and analysis of umbilical artery blood information

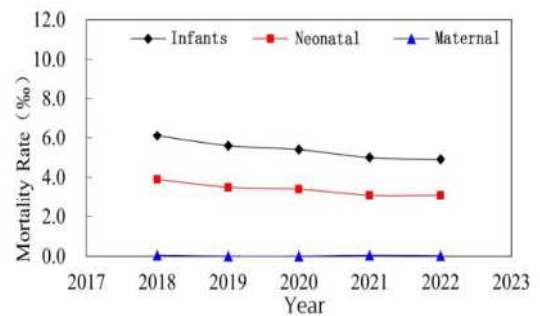


Fig.1-1 Mortality rates of maternal, infant, and neonatal

consists of: ① extraction of the short-time Fourier transform of the umbilical artery blood signal; ② calculation of the acoustic parameters to display the signal spectrogram; and ③ making a clinical diagnosis.

Most signals in nature are non-linear, and the complexity of life mechanisms leads to stochastic and non-linear biological systems, and the umbilical artery blood signal, which contains fetal vital signs is a non-linear signal [10]. Current clinical methods of fetal monitoring and umbilical artery Doppler ultrasound detection lack much of the information contained in the original signal, resulting in a lack of valid information [11]. Therefore, it is difficult to accurately diagnose fetal health based solely on Doppler signal detection. For this reason, appropriate non-linear processing methods and tools are important to accurately analyse the umbilical blood signal and detect the fetal health status.

As biological systems are strongly non-linear, the development of biomedical fields such as brain science, physiology and cardiac systems has benefited from the integration of biomedical and non-linear dynamics. As Glaick et al. [12] pointed out in 1988, the new mathematical tool of chaos theory will give rise to a new kind of physiology that will help researchers gain insight into complex human systems that are independent of local details. The application of chaos theory to the study of irregular complex dynamics in biomedicine has become inevitable.

The application of non-linear kinetic systems to physiological, pathological, and clinical research is of great significance. It not only provides a rich theoretical basis and experimental data for nonlinear theory, but also allows the exploration of the nature of various complex physiological phenomena and pathological processes through nonlinear theory, such as the application of nonlinear dynamics to the study and diagnosis of the cardiac system and the prediction of the severity of cardiovascular diseases. As chaotic characteristic parameters are more sensitive than traditional physiological monitoring parameters, their application as a non-invasive and quantitative tool in the diagnosis of cardiovascular diseases has been highly appreciated by researchers [13].

The paper uses fractal and chaos theory and machine learning methods to analyze and extract features from umbilical artery blood signals, with a view to accurately monitoring the growth of the fetus, detecting potential fetal diseases as early as possible and taking appropriate measures for timely management, reducing the rate of perinatal disability and mortality, and safeguarding the health of mothers and infants. By analyzing the fractal and chaotic characteristics of the umbilical artery blood signal, we can determine the difference between healthy and pathological blood signals and the characteristics of aberrant signals from both qualitative and quantitative perspectives, form a theoretical system for non-linear analysis of umbilical artery blood signals, and reveal the correlation between abnormal umbilical artery blood signals and maternal and fetal diseases, so as to build a

real-time monitoring mechanism for maternal and fetal health with higher accuracy and greater robustness. This will provide a more reliable, efficient, and scientific diagnostic index system for fetal development, and provide a theoretical basis and implementation method for improving the existing fetal monitoring and diagnosis methods.

1.2 Overview

The umbilical cord is the sole conduit for fetal nutrient acquisition, gas exchange with the mother and excretion of metabolic products. Alterations in cord hemodynamics are manifested as resistance to cord-placental blood flow circulation, which directly reflects certain physiological or pathological changes in the placenta, fetus, and mother [14]. The collection and analysis of umbilical artery blood signals can yield important information about fetal growth and development [15].

1.2.1 Conventional analysis methods of umbilical artery blood signal

In 1957, Satomura [16] first used Doppler to assess blood flow. In 1983, Campbell et al [17] first used Doppler velocimetry to measure uterine artery blood flow, resulting in a safe and non-invasive method for the analysis of uterine artery blood flow during pregnancy, which has led to ongoing research to date. In clinical obstetric diagnosis, ultrasound Doppler is often used to obtain information on fetal heart sounds and umbilical artery blood to detect fetal anomalies early and take action to reduce the probability of congenital diseases by early intervention [18].

Umbilical artery blood signals have complex time-varying characteristics and are typically non-stationary. The traditional methods of analysis of umbilical artery blood signals are acoustic spectral parameter method [19-20].

Doppler spectral parameters can be used to determine whether the umbilical blood signal is abnormal. Common spectral parameters include: maximum systolic umbilical flow velocity/end-diastolic umbilical flow velocity (S/D) [21]; Resistance Index (RI); and Pulsatility Index (PI), which are clinical diagnostic criteria. Hima [22] calculated the acoustic parameters of the middle cerebral artery and umbilical artery Doppler flow signals in pregnant women with intrauterine growth retardation (IUGR) versus normal pregnant women and found that the umbilical artery flow signals were better for the diagnosis of IUGR disease. Blanco et al. [23] extracted umbilical artery Doppler flow signals and calculated acoustic spectral parameters to detect pregnancy abnormalities, which can effectively provide information for fetal health assessment; Dai et al. [24] showed that the acoustic spectral parameters S/D values, PI and RI of umbilical artery blood were lower in pregnant women with acute intrauterine distress.

1.2.2 Study of non-linear analysis of umbilical artery blood signal

Most linear signals in nature are only somewhat approximate and are strictly non-linear. Complex biological signals are mainly characterized by strong background noise, nonlinearity, and stochasticity, while the human body is a typical nonlinear dynamical system [25]. In contrast to earlier experiments and observations on biosignals based on linear theory, the development of nonlinear theory has given a strong theoretical foundation and technical support for the study of nonlinear properties of organisms.

As an important discipline for solving nonlinear problems, fractal and chaos theory has achieved good research results and practical applications in engineering, materials, chemistry, biology, and medicine, especially in biomedical signal processing [26-27]. Fractal and chaos theories have been applied to the detection of physiological signals, medical image analysis, aided functional diagnosis and protein structure prediction [28-29]. Shang et al [30] found a positive correlation between the degree of cranial artery narrowing and the maximum Lyapunov index value of the flow signal based on chaos theory. Sladana et al.[31] calculated the Higuchi fractal dimension of cortical signals in the brain before and after damage and obtained the result that the fractal dimension of EEG signals changed with changes in brain alertness. Etehadtavakol et al. [32] compared the chaotic non-linear dynamics of breast temperature spectra of normal and abnormal lesions, showing that the Lyapunov index reflects the reliability of temperature recordings for breast tumor detection and can also differentiate between different types of breast lesions. Bogaert et al. [33] compared the correlation dimension of heart rate variability signals in heart transplanted patients and normal subjects and showed that the correlation dimension can clearly reflect the gender and physiological differences of patients with heart rate variability signals; Feng Yinbo et al. [34] analyzed the lumbar vertebral cancellous bone region images and calculated the fractal dimension of the grey-scale texture of lumbar cancellous bone CT images. metamorphosis, suggesting that fractal theory can be used for quantitative medical diagnosis based on CT images.

In summary, fractal and chaos theory can be applied to scientific medical diagnosis through the analysis of typical non-linear biomedical features such as Electrocardiography (ECG), arterial Doppler flow signals and Electroencephalography (EEG), i.e. the implicit information based on fractal and chaotic features can be obtained. Fractal and chaos theoretical analysis methods are more accurate and robust than traditional parametric methods, which are more powerful in processing non-linear information and provide a more complete picture of the deeper information in the signal, not only qualitatively but also quantitatively. Therefore, the analysis of umbilical artery flow Doppler signals using fractal and chaos theory is of great theoretical importance and application for real-time monitoring of maternal and fetal health status.

In the study of fractal theory for the analysis of umbilical artery blood signal, Chang et al. [35] calculated the fractal dimension of umbilical artery blood signal and explored its application value in fetal monitoring, which showed that the fractal dimension of umbilical artery blood signal in pathological state characterized the self-similarity of its digital signal, therefore, the fractal dimension can reflect the changes of umbilical artery blood in a more detailed and objective way than the traditional S/D value, and reflect the complex characteristics of umbilical artery hemodynamics. To demonstrate that the fractal dimension can better reflect the umbilical artery blood parameters, Wu et al. [36] analyzed the umbilical blood signals of 118 fetuses by comparing the fractal dimension of the Doppler audio signal during the cardiac cycle with the acoustic spectrum method.

Latifoğlu et al. [37] recorded umbilical artery Doppler signals from 20 normal pregnant women at 18 to 20 weeks' gestation and calculated fractal dimension curves using the Hurst index; RI, PI and S/D indices were calculated from the maximum frequency envelope of the Doppler sonogram and the fractal dimension curve, respectively, showing that the Doppler indices obtained from the fractal dimension curve had the same sensitivity as those obtained from the maximum velocity curve and that the PSD (Hurst) index was more sensitive than conventional Doppler indices in detecting changes in umbilical artery blood.

At present, the application of chaos theory to blood flow Doppler signals is rare. Pallavi et al. [38] proposed an algorithm to identify the umbilical and uterine arteries from a set of four different maternal and fetal arteries using Doppler features and correlation dimensions. To distinguish between these arteries, 132 Doppler signals were collected from pregnant women between 24 and 40 gestational weeks, filtered and de-noised, with a sensitivity and specificity of >95% for the identification of uterine arteries.

1.2.3 Current state of medical diagnosis research based on machine learning

Over the years, many statistical and machine learning methods have been used for medical data classification and disease diagnosis, including Linear Discriminant Analysis (LDA), Classification and Regression Tree (CART), Support Vector Machine (SVM), Artificial Neural Network (ANN), Radial Basis Function Neural Networks (BFNN), Multilayer Perceptron Neural Networks (MLPNN) and Random Forest (RF) algorithms, etc., and has achieved many innovative research results.

In the field of medical diagnosis, different machine learning methods are used to process datasets based on the classification of data features to make real-time predictions of diseases and achieve assisted diagnosis functions [39].

Based on the experimental results of ECG data from the European ST-T database, Jinho et al. proposed

an SVM and Kernel Density Estimation (KDE)-based ECG method for detecting ischemia. 355 ST-segment ischemia samples were successfully identified from 367 using the SVM classifier, and their sensitivity and specificity were 0.941 and 0.923, respectively. 0.923 [40]. For patients with Alzheimer's disease, Joao Maroco et al used seven nonparametric classifiers such as multilayer perceptron MLPNN, SVM, BFNN and RF and three traditional classifiers such as LDA and logistic regression to analyze the neuropsychological test data of the patients, and the results showed that the sensitivity, specificity, and accuracy of LDA algorithm and RF algorithm were better than other algorithms [41]. Baek et al. [42] used SVM and logistic regression to predict the onset of diabetic nephropathy based on clinical data from 292 diabetic patients, and the study showed that SVM showed the best results in predicting the onset of diabetic nephropathy. Liu Hongbo et al. [43] conducted research on early diagnosis of colorectal cancer with early colorectal cancer diagnostic data and developed an SVM-based laser-induced early colorectal cancer assisted diagnosis system with good clinical practice results. Wang Gang et al. [44] proposed a hepatitis diagnosis algorithm based on the UCI dataset (University of California Irvine, UCI), and the results showed that the algorithm based on SVM, and rough set has better diagnostic accuracy than neural network and SVM alone. Cai Dongmei et al. [45] proposed an epileptic EEG detection algorithm based on Hurst index and SVM, and the accuracy of automatic detection of epileptic brain waves reached 98.75%. Zhang Huimin et al. [46] established diagnostic models based on SVM, BP neural network and RBF neural network for predictive diagnosis of Alzheimer's disease, and the analysis results of clinical data prediction: SVM has good adaptability in predictive diagnosis compared with BP neural network and RBF neural network methods. Sang Xiu li et al. [47] established Least Squares Support Vector Machine (LS-SVM) parsing model for classification and diagnosis of breast tumors on 1569 breast cancer patient data based on neighborhood rough set simplification and obtained better clinical diagnosis results. Wu Cui ying et al. [48] proposed a new trimodal computer-aided diagnosis method based on integrated SVM for positron emission computed tomography/electron computed tomography of lung tumors.

Although machine learning has been widely used in medical diagnosis with good results, it has not yet been applied to fetal monitoring and fetal health prediction.

1.3 Aim and organization of this dissertation

Fractals and Chaos have been widely used in different fields as important mathematical tools for non-linear analysis. Fractal methods can quantitatively describe the intrinsic laws of things in nature. Chaos and fractals are both different and related: chaos is fractal in time, while fractals are chaotic in space, fractal dimension is a quantitative method to describe the characteristics of chaotic motion [49], and fractals are a

geometric language to describe chaotic motion.

Therefore, this study will use fractal and Chaos theories to perform a systematic and comprehensive non-linear characterization of the umbilical artery blood signal to obtain the box dimension, CD, MLE and chaotic time series feature parameters in the implied umbilical artery blood signal and the correlation with the fetal health status. Based on this, an artificial intelligence algorithm is used to classify and evaluate the clinical data of umbilical artery blood to build an intelligent diagnostic model, providing a theoretical basis and a way to implement clinical diagnosis of fetal health. The outline of the dissertation is shown in Figure 1-2.

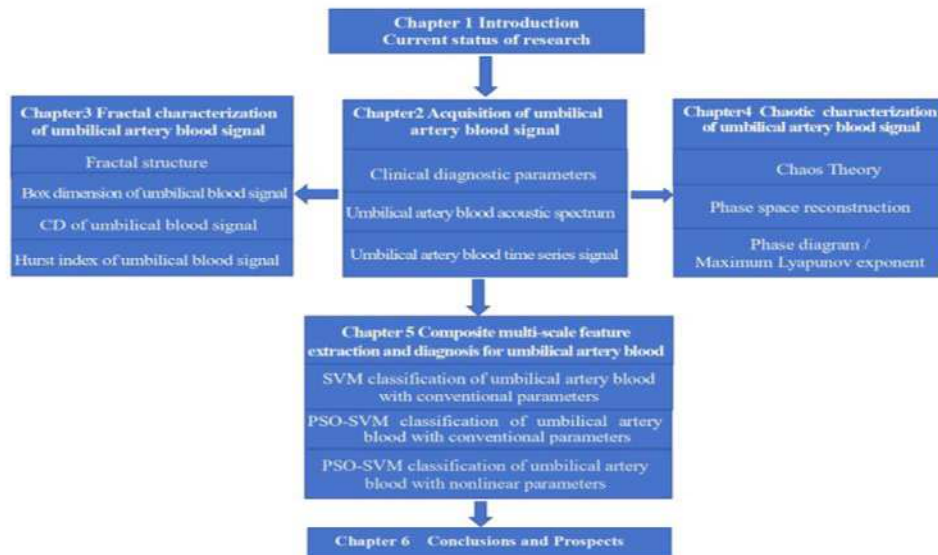


Fig.1-2 The outline of this dissertation

1.4 References

- [1] China Statistical Yearbook of the People's Republic of China [EB/OL]. [2020-12-20].<http://www.stats.gov.cn/tjsj/ndsj/2017/indexch.htm> .
- [2] National Health Commission of the People's Republic of China: Maternal and Infant Mortality Rates, etc., to be Reduced to Historic Low in 2022 [EB/OL]. (2023-03-19) [2023-06-12].<http://baijiahao.baidu.com/s?id=1767398140040162422&wfr=spider&for=pc>.
- [3] Circular of the Health and Health Committee of the People's Republic of China on the issuance of the Implementation Plan for the Implementation of the Outline for the Development of Chinese Women and Children for the Period 2021-2030[EB/O L]. (2022-04-08) [2020-01-08].

-
- <http://www.nhc.gov.cn/fys/s7900/202204/acaaffe2e44964a9b14fddd173cfa.shtml>.
- [4] Trends in maternal mortality 2000 to 2020 [EB/OL]. [2023-11-19].<https://www.who.int/China/publications-detail/9789240069251>.
- [5] Progress and challenges in women's, children's, and adolescent health [EB/OL]. [2023-11-19]<https://www.who.int/zh/news/item/25-05-2023-seventy-sixth-world-health-assembly---daily-update--25-may-2023>.
- [6] Zhong M, Huang YY. Evaluation of common fetal monitoring methods[J]. *Guangdong Medicine*, 2010,31(17): 2199-2200.
- [7] Trudinger B J, Giles W B, Cook C M. Uteroplacental blood flow velocity-time waveforms in normal and complicated pregnancy[J]. *Bjog An International Journal of Obstetrics & Gynaecology*, 2010,92(1): 39-45.
- [8] Fleischer A, Schulman H, Farmakides G, et al. Umbilical artery velocity waveforms and intrauterine growth retardation[J]. *American Journal of Obstetrics and Gynecology*, 1985,151(4): 502-505.
- [9] Sebire N J. Umbilical artery Doppler revisited: pathophysiology of changes in intrauterine growth restriction revealed[J]. *Ultrasound in Obstetrics and Gynecology*, 2003,21(5): 419-422.
- [10] Wu X F. Research on nonlinear characteristics of ultrasound Doppler blood flow signal and its application[D]. Fudan University, 1998.
- [11] Liu Z, Chang C, Wang YY, et al. Clinical application of multiple methods for evaluation of umbilical artery Doppler signals[J]. *Chinese Journal of Ultrasound Imaging*, 2002, 11(9): 540-542.
- [12] Gleick J, Hilborn R C. Chaos, Making a New Science[J]. *American Journal of Physics*, 1988, 56(11): 1053-1054.
- [13] Huang R S, Huang H. Chaos and its applications (2nd ed.) [M]. Wuhan: Wuhan University Press, 2006.
- [14] Wang Y, Wang T, Chen H. The use of umbilical artery flow testing in the prognosis of fetal growth restriction[J]. *Chinese Family Planning and Obstetrics and Gynecology*, 2013,5(4): 43-45.
- [15] Zhang Z J, Wang H. Exploration of ultrasonic Doppler measurement of umbilical artery flow[J]. *Chinese Journal of Obstetrics and Gynecology*, 1990,25(4): 212-214.
- [16] Satomura S. Ultrasonic Doppler method for the inspection of cardiac function [J]. *The Journal of the Acoustical Society of America*, 1957,29(11): 1181-1185.
- [17] Campbell S, Griffin DR, Pearce JM et al. New Doppler technique for assessing uteroplacental blood flow[J]. *The Lancet*, 1983,321(8326): 675-677.
- [18] Fan C Y, Lu C M, Qi Z Q. Exploring the relationship between colour Doppler ultrasound umbilical hemodynamic measurements and pregnancy outcomes[J]. *Biomedical Engineering and Clinical*, 2015,19(02): 136-139.
- [19] Blanco P G, Vercellini R, Rube A, et al. Evaluation of Feline Uterine and Umbilical Arteries Blood Flow in a Pharmacologically Induced Abnormal Gestation Model[J]. *Theriogenology*, 2016,86(9): 2323-2327.

- [20] Malcus P, Andersson J, Marsál K, et al. Waveform Pattern Recognition--a New Semiquantitative Method for Analysis of Fetal Aortic and Umbilical Artery Blood Flow Velocity Recorded by Doppler Ultrasound[J]. *Ultrasound in Medicine & Biology*, 1991,17(5): 453-460.
- [21] Kara S, Latifoglu F, Guney M. Fractal Analysis of Umbilical Artery Doppler Signals from Normal Pregnant Subject Using Hurst Exponent[C]// *Frontiers in the Convergence of Bioscience & Information Technologies*, Fbit. IEEE Computer Society, 2007.
- [22] Hima B T. Cerebral and Umbilical Arterial Blood Flow Velocity in Normal and Growth Retarded Pregnancy[J]. *Journal of Obstetrics & Gynecology of India*, 2009,59(1): 47-52.
- [23] Blanco P G, Vercellini R, Rube A, et al. Evaluation of Feline Uterine and Umbilical Arteries Blood Flow in a Pharmacologically Induced Abnormal Gestation Model[J]. *Theriogenology*, 2016,86(9): 2323-2327.
- [24] Dai W, Xu Y, Ma X W, et al. Ultrasonic Characteristics and Clinical Significance of Umbilical Cord Blood Flow in Acute Fetal Distress[J]. *Journal of Acute Disease*, 2016,5(6): 483-487.
- [25] Ning X B. Preface: A study of nonlinear dynamics of physiopathological signals[J]. *Journal of Nanjing University (Natural Sciences)*, 2008,44(4): 8-10.
- [26] Cai W, Chen W, Xu W X. Characterizing the Creep of Viscoelastic Materials by Fractal Derivative Models[J]. *International Journal of Non-Linear Mechanics*, 2016,87(12): 58-63.
- [27] Heymans O, Fissett J, Vico P, et al. Is Fractal Geometry Useful in Medicine and Biomedical Sciences[J]. *Medical Hypotheses*, 2000, 54(3): 360-366.
- [28] Hu Z Y, Du D P, Du Y C. Generalized polynomial chaos-based uncertainty quantification and propagation in multi-scale modeling of cardiac electrophysiology[J]. *Computers In Biology And Medicine*, 2018,102(11): 57-74.
- [29] Liu X F, Ye Z Q, Liu Q F. Fractal characterization of heart rate variability during anesthesia[J]. *Journal of Biomedical Engineering*, 2006,23(3): 10-13.
- [30] Shan H N, Wang Z Q, Wang J, et al. Comparison and Analysis of the Lyapunov Exponents of Blood Flow Signal of Healthy and Stenotic Artery[C]// *IEEE: Icarcv 2004 8th Control, Automation, Robotics and Vision Conference*, 2004.
- [31] Spasic S. Surrogate Data Test for Nonlinearity of The Rat Cerebellar Electrocardiogram in the Model of Brain Injury[J]. *Signal Processing*, 2010, 90(12):3015-3025.
- [32] Etehadtavakol M, Ng E Y K, Lucas C, et al. Nonlinear Analysis Using Lyapunov Exponents in Breast Thermograms to Identify Abnormal Lesions[J]. *Infrared Physics & Technology*, 2012,55(4): 345-352.
- [33] Bogaert C, Beckers F, Ramaekers D, et al. Analysis of Heart Rate Variability with Correlation Dimension Method in a Normal Population and in Heart Transplant Patients[J]. *Autonomic Neuroscience Basic & Clinical*, 2001,90(2): 142-147.
- [34] Feng Y B, Fang F M, Chen H W, et al. Study on the application of fractal dimension in CT lumbar cancellous bone images[J]. *Journal of Tongji University Medical Edition*, 2016,37(3): 107-111.
- [35] Chang C Wu X F. The value of fractional dimensional measurement of fetal umbilical artery Doppler signals[J]. *Chinese Journal of Obstetrics and Gynecology*, 1998,36(3): 145-147.

- [36] Wu X F, Wang W Q, Yu J G, et al. Study on the fractal characteristics of ultrasonic Doppler audio signals[J]. Chinese Journal of Biomedical Engineering, 1999,018(4): 389-394+432.
- [37] Latifoğlu F, Kara S, Güney M. Determining fractal dimension of umbilical artery Doppler signals using Hurst exponent[J]. Journal of Medical Systems[J], 2007,31(6): 529-536.
- [38] Pallavi V, Gupta L, Naik S K, et al. Doppler based identification of uterine artery and umbilical artery for monitoring pregnancy[C]//International Conference of the IEEE Engineering in Medicine & Biology Society. PubMed, 2010:6300-6303.
- [39] Dayle L. Sampson, Tony J. Parker, Zee Upton, et al. A Comparison of Methods for Classifying Clinical Samples Based on Proteomics Data: A Case Study for Statistical and Machine Learning Approaches[J]. Plos One, 2011, 6(9):1-11.
- [40] Jinho Park, Witold Pedrycz, Moongu Jeon. Ischemia Episode Detection in ECG using Kernel Density Estimation, Support Vector Machine and Feature Selection[J]. Biomedical Engineering Online, 2012, 11(1): 1-17.
- [41] Maroco J, Silva D, Rodrigues A, et al. Data mining methods in the Prediction of Dementia: A real-data comparison of the accuracy, sensitivity and specificity of linear discriminant analysis, logistic regression, neural networks, support vector machines, classification trees and random forests[J]. BMC Research Notes 2011,4: 1-14.
- [42] Cho B H, Yu H, Kim K W, et al. Application of irregular and unbalanced data to predict diabetic nephropathy using visualization and feature selection methods[J]. Artificial Intelligence in Medicine, 2008, 42(1): 37-53.
- [43] Liu H B, Tang Z F, Yang Y L, et al. Identification and classification of high risk groups for Coal Workers' Pneumoconiosis using an artificial neural network based on occupational histories: a retrospective cohort study[J]. BMC Public Health, 2009, 09(1): 1-8.
- [44] Wang G, Liu Y N, Chen HW, et al. Application of rough sets and support vector machines in hepatitis diagnosis[J]. Journal of Jilin University (Engineering Edition), 2011, 41 (C1): 160-164.
- [45] Cai D M, Zhou W D, Liu K, et al. An EEG detection method for epilepsy based on Hurst index and SVM[J]. Chinese Journal of Biomedical Engineering,2010,29(06):836-840.
- [46] Zhang H. Research on intelligent diagnosis of Alzheimer's disease based on SVM[J]. Journal of Nanjing Normal University (Engineering Technology Edition), 2016,16(02): 86-92.
- [47] Sang X L, Li Z, Lv L. Breast tumor classification diagnosis based on NRS and improved LS-SVM parsing model[J]. Statistics and Decision Making, 2017,33(01): 84-86.
- [48] Wu C Y, Zhou T, Lu H L, et al. A three-modality computer-aided diagnosis method for PET/CT of lung tumors based on integrated SVM[J]. Biomedical Engineering Research, 2017, 36(03): 207-212.
- [49] Wang X Y, Meng J. Fractal geometry and applications [M]. Beijing: Science Press, 2016.

Chapter 2

Acquisition of umbilical artery blood signal

2.1 Fetal Hemodynamics

Hemodynamics is the study of the physics of flowing blood and all the solid structures through which it flows [1]. Blood is a heterogeneous fluid with high viscosity, and the solid structures through which it flows include the heart and blood vessels at all levels. Blood vessels are elastic tubes that can contract and dilate, and the factors that affect their diameter are mainly blood pressure, blood pH, oxygen partial pressure and the diastolic activity of the smooth muscles of the walls, whose flow is characterized by pulsatile non-stability [2].

2.1.1 Fetal blood circulation

Figure 2-1 shows the fetal blood circulation. In the fetal circulation, a large amount of blood returns to the fetal heart and contains a large amount of nutrients, and at different locations, venous and arterial blood converge to varying degrees. Fetal blood circulation differs from adult blood circulation in that two umbilical veins and one umbilical artery are connected to the placenta, and the umbilical vein and inferior vena cava are connected to the intrahepatic venous catheter. Fetal blood flows from the right atrium to the left atrium through the foramen ovale in the atrial septum, and the aorta is connected to the pulmonary artery trunk by an arterial canal portal [4].

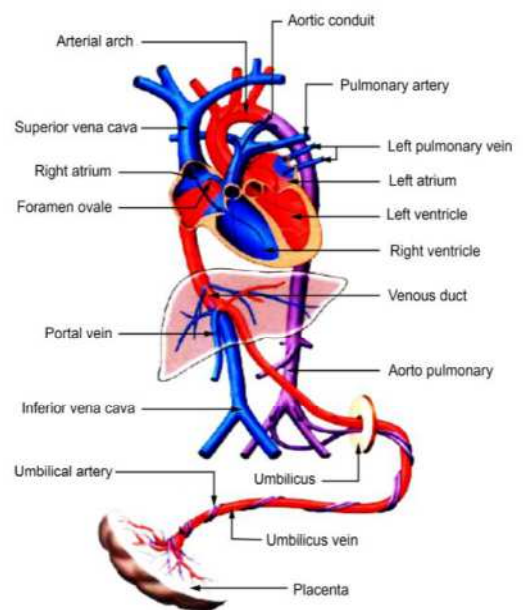


Fig.2-1 Fetal blood circulation [3]

2.1.2 Placental development process

During pregnancy, the placenta develops to meet the growing metabolic needs of the fetus, which is achieved through the transfer of nutrients and oxygen from the mother and the transfer of metabolic waste from the fetus. In addition, the placenta protects the fetus from the maternal immune system and secretes hormones and growth hormones to regulate the physiological functions of the pregnant woman during pregnancy [5-6].

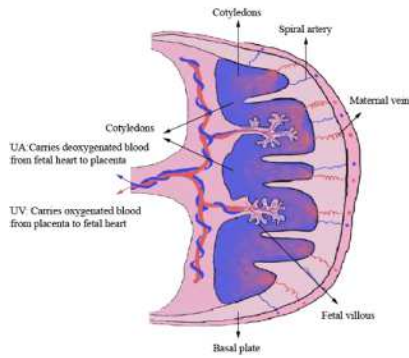


Fig. 2-2 Placental composition

Anatomically, the human placenta can be divided into three components: the uterine placenta (maternal part), the fetal placenta and the substrate [7], as shown in Figure 2-2. Oxygen-rich maternal blood passes through the uterine artery into the uteroplacental vessels, forming spiral arteries that increase in diameter as gestation increases and as the chorionic gaps widen, increasing the flow of blood to the uterine artery [8-9]. The intervillous space is a large interconnected area consisting of a pool of maternal blood, separated from the fetal placental vessels by the substrate [10]. The maternal vasculature in the basal plate region contains trophoblast cells, and these placenta-specific cells are involved in vascular reconstruction and hormone secretion. Although both fetal and maternal uterine placental vessels develop as low resistance vascular beds during gestation, the structure of the fetal placenta differs significantly from that of the uterine placenta [11]. The circulation of the fetal placenta is as follows: the hypoxic blood pumped from the fetal heart flows along the descending aorta into each branch of the internal iliac artery, and these branches converge to form a single umbilical artery [12], and two umbilical arteries surround the umbilical vein and branch into repeating functional umbilical cords called cotyledons. Within each cotyledon, the umbilical arteries continue to bifurcate into dichotomous/fractal arteries of progressively smaller diameter, the smallest of which form capillaries. The embryonic trophoblast prevents the mixing of fetal and maternal blood due to the microvilli it contains, allowing the fetus to draw additional nutrients from maternal blood [13].

In addition, the capillaries between the villi and chorion form a maternal-fetal exchange zone where the waste products expelled by the fetus diffuse back into the Figure 2-2 Composition of the placenta blood in the maternal uterine veins and oxygen and nutrients are transported to the trophoblastic layer of the uterus (the villi) and into the venous vessels of the placental villi. These vessels eventually enter the umbilical vein, which delivers nutrient-rich blood to the fetal organs. Finally, the umbilical cord and the cotyledons (15-28 per placenta) form the disc-shaped fetal placental vascular system.

2.1.3 Umbilical cord structure and characteristics

The diameter, length and average length of the umbilical cord are: 1-2.5 cm, 30-80 cm and 54-61cm respectively [14]. The umbilical cord is considered too short when it is less than 30cm and too long when it is more than 80cm. The white amniotic membrane covers the surface of the umbilical cord and the arteries and veins inside the cord are surrounded by a translucent matrix called Wharton jelly. The umbilical vein surrounds the umbilical artery as it is longer than the umbilical artery. Unlike the isolated, atrophied umbilical cord, which has been completely emptied of blood, the umbilical cord is full of blood vessels in the living body and the veins are particularly thick because of the internal flow of blood [15].

2.2 Umbilical artery wave dynamics

An understanding of umbilical artery wave mechanics is required prior to studying the detection of Doppler ultrasound signals in the umbilical artery. The waveform of blood flow velocity observed in the umbilical artery is determined by the function of the fetal heart and the placenta. When the fetal heart contracts, the umbilical artery generates a positive waveform that moves along the umbilical artery. When this positive waveform crosses the blood flow waveform of the vessels downstream of the placenta, a portion of the positive waveform is reflected due to a mismatch with the impedance of the fetal placental vessels. Thus, the observed umbilical artery Doppler velocity waveform is a superimposed waveform of reflected waves (placental action) moving in the forward direction (cardiac function action) and moving in the reverse direction (cardiac function action). It is possible to isolate the placenta-specific Doppler signal for the purpose of detecting placental vascular abnormalities using wave dynamics theory.

2.2.1 Constant pressure-flow relationships

The cardiovascular system transports nutrients and oxygen to the body and carries metabolites from the body's cells through blood circulation. The engine of the circulation is the heart, which pumps blood rhythmically into the heart in an oscillating pressure gradient to ensure that the cells are always adequately nourished and that their metabolic needs are met. The pressure-flow relationship in the arterial part of the circulatory system is usually described based on Poiseuille's law [16]:

$$Q = \Delta p \pi r^4 / 8\eta L \quad (2-1)$$

Where: Q is the intravascular blood flow; Δp is pressure difference; L is vascular length; r is vascular radius; η is blood viscosity.

Rewriting Equation (2-1) as a proportional relationship between pressure gradient and flow rate:

$$\frac{\Delta p}{Q} = \frac{8\eta L}{\pi r^4} \quad (2-2)$$

It is possible to better understand Poiseuille's law, which states that the pressure difference required to drive a fluid through a vessel is related to the geometrical parameters of the vessel and the physical properties of the fluid. The pressure-flow ratio is related to the degree of vascular resistance to flow, which is expressed by the parameter R , defined as vascular resistance :

$$R = \frac{\Delta p}{Q} \quad (2-3)$$

Where: R is the flow resistance of blood in a given segment of blood vessel, also known as peripheral resistance, derived from elastic shear stress.

From Equation (2-2) and Equation (2-3), we have:

$$R = \frac{\Delta p}{Q} = \frac{8\eta L}{\pi r^4} \quad (2-4)$$

From Equation (2-4), the radius of the blood vessel has a large effect on the resistance to flow: the resistance is proportional to the inverse of the fourth power of the vessel radius.

The resistance to flow characterizes the dissipation of energy, with the viscous friction between the blood and the wall of the tube preventing the flow of blood resulting in a loss of energy [17].

Although resistance of computational hemodynamic can help to provide a comprehensive understanding of the pathology for the disease, it is assumed that the resistance of Equation (2-4) is only valid under conditions of constant, fully developed laminar flow with a rigid vessel wall. When the flow is predominantly pulsation-driven and the vessel wall is elastic, wave propagation and reflection in the arterial system will occur and Poiseuille's law will not be valid [18].

Due to the elasticity of the vascular wall, the vessel dilates in response to an increase in intravascular pressure P and the corresponding volume V increases. To express the relationship between vascular pressure and volume, the vascular compliance parameter C was introduced. Vascular volume has the property of increasing pressure but not rupture and is defined as the volume of the vessel corresponding generally to a change in pressure units.

$$C = \frac{dV}{dP} \quad (2-5)$$

Where: dV is the volume variable; dP is the pressure change.

From above definition, C is the vascular volume corresponding to a change in unit pressure and is an indicator describing the dilatable capacity of the vascular; a larger C indicates greater Vaso dilatability [19].

2.2.2 Poiseuille's pressure-flow relationship

According to Poiseuille's law, if the velocity of blood flow does not change over time at a particular location in the vascular, it is constant flow. Conversely, if the blood flow exhibits unstable or pulsatile flow, the flow velocity at a fixed location in the vessel varies with time and becomes non-constant.

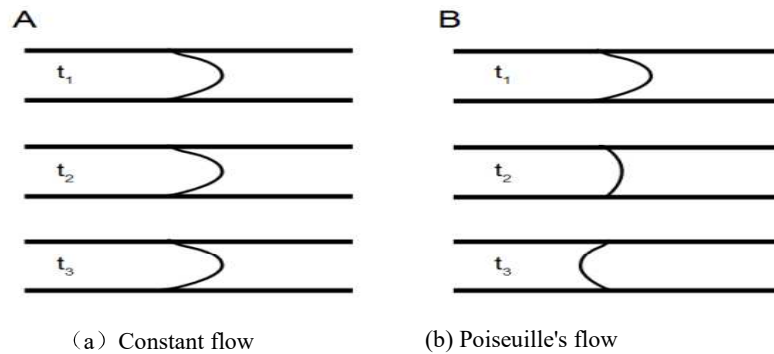


Fig. 2-3 Pressure-flow relationship

As seen in Figure 2-3 (a): the flow profile is constant at a fixed position along the vascular at different time points (t_1 , t_2 , t_3); whereas in the pulsatile flow of Figure 2-3 (b), the variation in blood velocity makes the flow unstable and oscillatory, due to the systolic-diastolic cycle caused by rhythmic contraction of the heart.

When the oscillatory pressure difference increases, there is a time lag before the blood flow rate increases, i.e., the peak blood flow lags the peak pressure. This is caused by fluid inertia resisting the pressure changes that drive fluid flow, and it is a form of resistance called inertia.

In addition, the elasticity of the arterial vessels allows Doppler waves to propagate and be reflected. In elastic vascular, the increase in local pressure caused by ventricular ejection during systole causes the vessel wall to dilate outwards; accordingly, the elasticity of the vascular wall resists the change in pressure. As the pressure decreases during diastole, the vascular protrudes less outwards and blood flows forward along the vascular wall. As the vascular dilate and contract with each heart rate cycle, the pressure and hence the flow propagates through the arterial system at a finite rate like a wave, as shown in Figure 2-4.

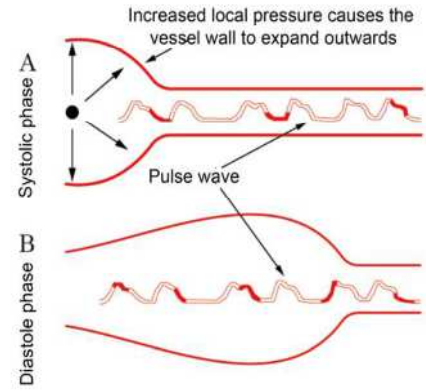


Fig. 2-4 Intravascular pulse wave propagation

As can be seen in Figure 2-4(A), during systole, the increase in local pressure at one end of the elastic vessel drives the blood vessel wall outward, while in diastole, as the pressure decreases, the locally dilated vessel contracts, and advances at a limited rate. With the continuous systolic-diastolic oscillatory pressure cycle, a series of pulse waves propagate along the vessel. In addition, physical properties such as vessel diameter, elasticity, vessel bifurcation and blood viscosity change as the pulse wave travels along the vessel, and a portion of the wave is reflected. These changes in the physical properties of the vessel determine the resistance and reactance of the system, where resistance represents the resistance to flow due to the viscous friction of the blood along the vessel wall. On the other hand, reactance represents the impedance to which the wave is subjected as it travels along the vessel and is caused by the combined effect of the inertia of the fluid and the elasticity of the vessel.

The combination of impedance and reactance is known as impedance, in other words, the reflection of a wave occurs in the presence of impedance, i.e. when the physical properties of the vessel and blood change. Because impedance exists for wave propagation, viscous frictional resistance causes impedance and reflection of waves, and therefore vascular impedance occurs at a random frequency [20].

2.2.3 Input impedance

In hemodynamics, the ratio of pulsating pressure to flow in the presence of a reflected wave is called the input impedance (Z_i):

$$Z_i(f) = \frac{P_m(f)}{Q_m(f)} \quad (2-5)$$

Where: f is the frequency; P_m and Q_m are the measured pressure and flow respectively.

In contrast to characteristic impedance, which depends only on the local physical properties of the blood vessel (e.g., the radius or elasticity of the vessel), the input impedance is determined not only by the

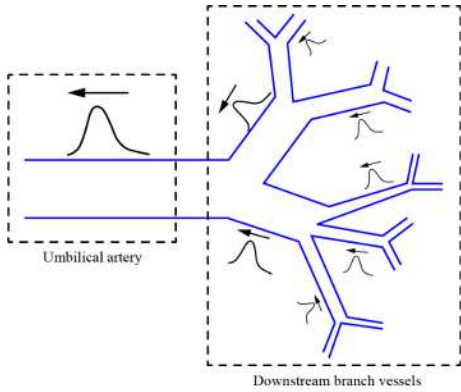


Fig. 2-5 Schematic of the placental vascular system

local conditions of the blood vessel in a given cross-section, but also by the physical properties of the blood vessel distant from the cross-section. For example, when the physical properties of the blood vessel in a continuous vessel segment change continuously in a branching blood vessel network, a mismatch in the characteristic impedance of the vessel will produce a reflected wave that propagates in the opposite direction towards the input vessel. If the impedances of the blood vessels are matched, no reflected waves are generated.

Thus, as the cardiac pressure wave generated by the fetal heart moves forward along the umbilical artery, a continuous mismatch of vascular impedance along the fractal network will generate multiple reflected waves as it encounters a fractal network of smaller placental artery diameters, as shown in Figure 2-5.

In Figure 2-5, these reflected waves combine to form a composite wave in the opposite direction to the forward net flow wave. Thus, a single reflected wave in the umbilical artery feeding into the placental system provides information about the placental artery vasculature downstream of where the reflected wave is generated. The composite reflected wave in the umbilical artery Figure 2-5 Schematic diagram of the placental vascular system represents the sum of multiple reflected pulse waves that occur at sites of impedance mismatch in the fetal placental vascular system, with arrows indicating the direction of pressure wave propagation.

2.2.4 Pulse wave propagation and wave velocity

The speed of propagation of a pulse wave along a vessel is denoted as PWV and it depends mainly on the elasticity size of the vessel, the relationship is usually expressed by the Moens-Korte Weg Equation [17], where the wave speed PWV is defined as:

$$PWV = \sqrt{\frac{Eh}{2\rho r}} \quad (2-6)$$

Where: E is the Young's modulus, i.e. the ratio of stress to strain; ρ is the fluid density; h is the vessel wall thickness and r is the vessel radius. As can be seen from (2-6), for stiffer blood vessels (i.e. high Young's modulus), the pulse propagates at high velocity along the vessel wall. Studies have shown that the aorta in humans becomes less elastic with age and PWV increases. In general, PWV in the human arterial

system decreases from 6m/s-8m/s in the aorta to 2m/s in the pulmonary arteries. In fetal sheep, PWV of the umbilical artery is close to 6m/s, like the value in the human aorta [21].

Another way to estimate PWV is not to measure elasticity directly, but to estimate it from the characteristic impedance and plasticity of the vessel [22]. The magnitude of the characteristic impedance Z_c value depends on the physical properties of the local vessel and is defined as the ratio of pressure to flow in the absence of wave reflection:

$$Z_c = \Delta P / \Delta Q \quad (2-7)$$

In addition, the plasticity of blood vessels C is the ratio of the change in cross-sectional area of blood vessels ΔA to the change in pressure ΔP :

$$C = \Delta A / \Delta P \quad (2-8)$$

The relationship between the plasticity of the blood vessels C and Z_c is as follows

$$Z_c = \sqrt{\frac{\rho}{A} \cdot \frac{1}{C}} \quad (2-9)$$

Where: ρ is the blood density; A is the cross-sectional area of the blood vessel. Because of the presence of reflected waves, direct measurement of Z_c is not possible and measurement of pressure changes requires insertion of a catheter. Substituting Z_c into Equation (2-7), the plasticity expression is as follows:

$$Z_c \Delta Q = \Delta P \quad (2-10)$$

$$Z_c \Delta P = \Delta A / C \quad (2-11)$$

$$Z_c = \Delta A / C \Delta Q \quad (2-12)$$

$$\sqrt{\frac{\rho}{A} \cdot \frac{1}{C}} = \frac{\Delta A}{C \Delta Q} \quad (2-13)$$

$$C = \left(\frac{\Delta A}{\Delta Q} \right)^2 \cdot \frac{A}{\rho} \quad (2-14)$$

Since the relationship between plasticity and PWV is as follows:

$$PWV = \sqrt{\frac{A}{\rho} \cdot \frac{1}{C}} \quad (2-15)$$

Substituting equation (2-14) into Equation (2-15) yields PWV versus change in flow rate ΔQ and change in area ΔA :

$$PWV = \frac{\Delta Q}{\Delta A} \quad (2-16)$$

PWV can therefore be estimated by measuring the slope of the flow area curve during the reflection-free period. It is generally assumed that there are no reflected waves early in the contraction.

2.3 Conventional diagnostic parameters of umbilical artery blood

Upstream and downstream of the umbilical arteries vessels are the fetal heart and the umbilical cord lateral

placental vascular bed, which travels in the amniotic fluid, respectively. Under normal conditions, the umbilical artery measures placental blood flow velocity decreases with the progression of pregnancy, whereas the uterine and umbilical arteries are more abundantly vascularized and have relatively fast blood velocity during contraction, which ensures normal fetal growth. When pregnancy is abnormal, the uterine and umbilical artery flow is decreased during diastole and there is also antegrade flow during diastole. Additionally, there is a substantial heavy waveform trace during systole [23]. The umbilical artery blood velocity waveform is shown in Figure 2-6.

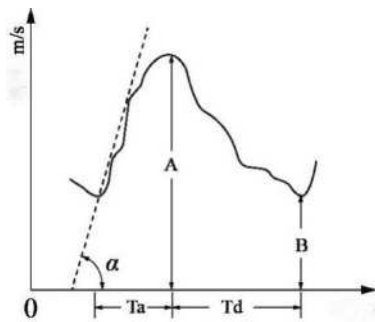


Fig.2-6 Schematic diagram of umbilical artery blood velocity waveform

In Figure 2-6, the highest point of systole is A and the lowest point of end-diastole is B. B greater than zero means that there is still positive blood flow at end-diastole. T_a indicates systolic acceleration time and T_d indicates diastolic time. The slope of the acceleration wave at the beginning of systole with respect to the baseline is the acceleration angle α , which is related to the intensity of myocardial contraction [24].

2.3.1 Clinical diagnostic parameters for umbilical blood signals

The most used three diagnostic parameters for umbilical artery blood velocity are defined as flowering Figure 2-7. This schematic diagram is derived from the envelope of the spectrogram of the umbilical artery blood signal (see section 2.5.2).

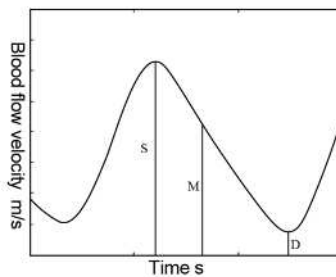


Fig.2-7 Schematic diagram of the definition of the umbilical artery blood velocity index

1. S/D :

$$S/D = V_p / V_d \quad (2-17)$$

In the Equation (2-17), S/D indicates the peak-to-valley ratio(the maximum systolic/end- diastolic umbilical flow velocity); V_p is the highest systolic peak; V_d is the end-diastolic peak; the value S/D reflects the magnitude of the change in blood flow velocity during the cardiac cycle and reflects vascular compliance. Normal values are shown in Figure 2-8.

It is generally accepted that the S/D value decreases gradually with increasing gestational weeks in normal pregnancy. As the gestational week progresses, the S/D ratio decreases rapidly under the influence of the dual factors of gradually decreasing placental blood flow resistance and increasing umbilical blood flow velocity at the end of diastole. Before 24 weeks of gestation, $SD \leq 4$; at 30 weeks of gestation, SD decreases to 2.7; after 30 weeks of gestation, $SD < 3$, and in late gestation, $SD < 2.2 \pm 0.3$, with an upper limit of 3.01 as the normal value [25].

Clinically high S/D value can occur in hyperemesis, hydramnios, intrauterine growth retardation (IGUR) and tangled or short umbilical cords.

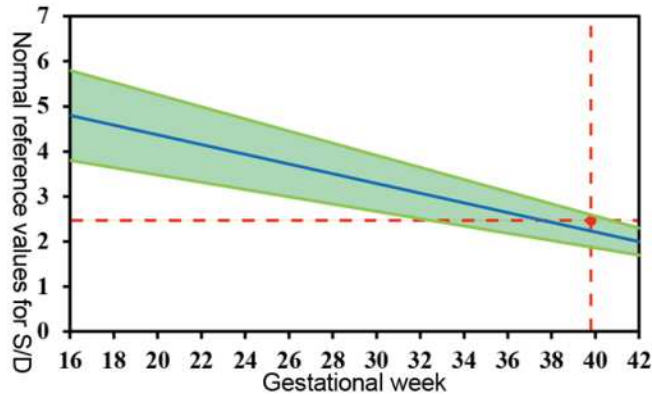


Fig. 2-8 Normal reference values for S/D

In Figure 2-8, the horizontal coordinate is gestational week, the vertical coordinate is S/D value, and the green area is the normal reference value.

2. PI

$$PI = (S - D) / M = (V_p - V_d) / V_m \quad (2-18)$$

Where PI indicates the beating index; V_m is the mean value of frequency change. PI reflecting vascular elasticity, the more disparate the ratio of the drop in diastolic blood flow velocity to the average velocity of the heart, the greater the PI value.

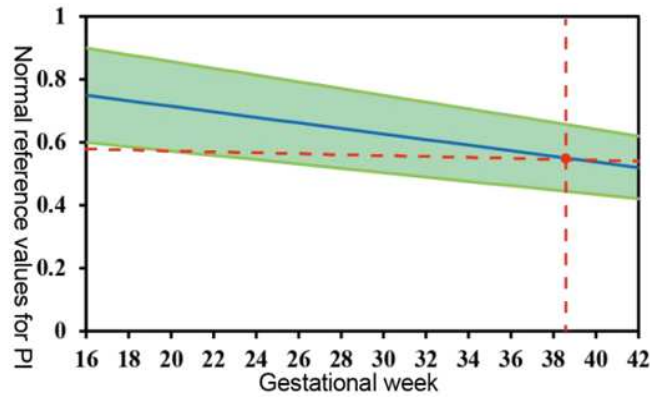


Fig.2-9 Normal reference values for PI

In Figure 2-9, the horizontal coordinate is gestational week the vertical coordinate is PI value, and the green area is the normal reference value.

3. RI

$$RI = (S - D) / S = (V_p - V_d) / V_p \quad (2-19)$$

A resistance index called RI denotes peripheral resistance. When there is a low impedance cycle, RI shows that the blood flow velocity fluctuations have an amplitude that is getting close to the maximal end-systolic blood flow velocity.

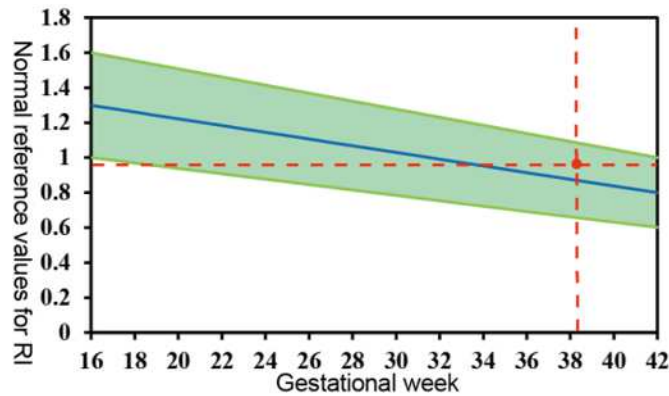


Fig.2-10 Normal reference values for RI

In Figure 2-10, the horizontal coordinate is gestational week, the vertical coordinate is RI value, and the green area is the normal reference value.

4. FVR fast blood flow ratio

$$FVR = Q_1 / Q \quad (2-20)$$

Where: Q is the total blood flow in a single cardiac cycle, reflecting the preload and pumping function of the heart; Q_1 refers to the rapid ejection phase blood flow, i.e., the blood flow contained when the velocity of blood flow is greater than 0.707 times the highest blood flow velocity at the end of systole.

2.4 Detection of umbilical artery blood signal

Direct measurement of fetal umbilical blood flow is mostly performed by ultrasound Doppler technique, i.e., the measurement of aortic blood flow. For blood vessels with a constant flow model, blood flow can be calculated by the formula $Q = VA$, where: V is the mean blood velocity and A is the cross-sectional area of the vessel. However, in obstetric applications, there are many factors that affect the accuracy of the measurement; therefore, direct measurement is not currently used to measure fetal blood flow.

2.4.1 Doppler effect of moving sound sources

When ultrasound waves emitted by a source at a fixed frequency encounter an active interface, there is a difference between the frequency of the returned sound waves and the fixed emitted frequency; that is: as the interface moves away from the vibrating source, the frequency of the returned sound waves decreases; conversely, the frequency increases [26]. Clinically, blood flow velocity can be measured according to the principle of the Doppler effect.

In Figure 2-11 below, the sound source S is moving in a uniform linear motion with a velocity vector V .

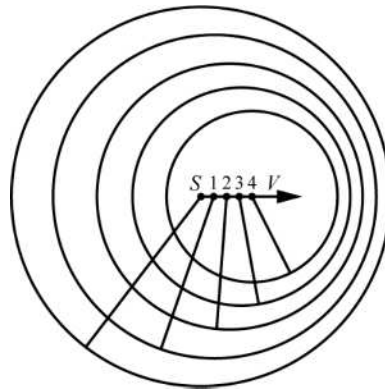


Fig. 2-11 Motion sound source

Let $t = 0$ be the time when the sound source is at the origin S and the phase of the vibration is zero. At time t' , the location of the sound source is $r' = Vt'$ and the phase of the vibration is $\phi = \omega_0 t'$. At time t , the vibration phase ϕ propagates to the point r , then:

$$|r - Vt'| = (t - t')c \quad (2-21)$$

The partial derivative of the phase with respect to time is the angular frequency, so the received frequency at the point r is $\omega = \frac{\partial \phi}{\partial t} = \omega_0 \frac{\partial t'}{\partial t}$, and the derivative of t' on both sides gives

$$-\frac{V \cdot (r - Vt')}{|r - Vt'|} \frac{\partial t'}{\partial t} = \left(1 - \frac{\partial t'}{\partial t}\right)c \quad (2-22)$$

If the angle between the vector $r - Vt'$ and V from the source to the receiver is θ , the left-hand side of the above equation is $\omega = \omega_0 + \omega_0\beta$. Here: $V = |V|$ is the motion velocity of the sound source. Thus $\frac{\partial t'}{\partial t} = \frac{1}{1 - \beta}$, where $\beta = V \cos \theta / c$ is substituted into the above equation to obtain:

$$\omega = \omega_0 / (1 - \beta) \quad (2-23)$$

The above equation is known as the Doppler equation.

In summary, the analysis shows that the frequency received is different from the frequency of the sound source due to its motion. The change in frequency is $\Delta\omega = \omega_0 V \cos \theta / c$, usually referred to as $f/2$ as the Doppler shift, which is proportional to the frequency and speed of the sound source. The Doppler shift is direction dependent, if the source is moving towards the receiving point, the frequency increases at $\theta > \frac{\pi}{2}$; if the source is moving back towards the receiving point, the frequency decreases at $\theta > \frac{\pi}{2}$; and when $\theta = \frac{\pi}{2}$, the distance between the source and the receiving point is constant, the frequency is also constant.

2.4.2 Ultrasonic Doppler velocimetry

Common measurements of blood flow velocity is as follows: the sound source emits sound, which travels through a fluid medium to a location and is reflected by an object and then received by the source. Some of this will be reflected in the external medium, mainly by red blood cells in blood, and the frequency shift Δf can be expressed as:

$$\Delta f = 2Vf_s / c \quad (2-24)$$

Where: V is the flow velocity, f_s is the emission frequency and c is the velocity of sound propagation in the medium. The sensor is placed outside the blood vessel and is oriented at an angle θ to the axial direction of the blood flow, the velocity measured by the sensor is only a component of the axial velocity of the blood flow, so a correction to the Doppler frequency shift equation is required:

$$\Delta f = 2Vf_s \cos \theta / c \quad (2-25)$$

To calculate the axial velocity of the blood flow, the Doppler frequency shift equation can be expressed as V :

$$V = \frac{\Delta f}{f_s} \frac{c}{2 \cos \theta} \quad (2-26)$$

or

$$\frac{V}{c} = \frac{\Delta f}{2f_s \cos \theta} \quad (2-27)$$

It can be obtained Equation (2-26) that the ratio of the reflected velocity to the sound wave velocity is proportional to the ratio of the frequency shift to the wave source frequency. From Equation (2-27), the frequency shift shifts upwards with the direction of relative motion, while the direction of relative motion shifts downwards, so the installation direction of the ultrasonic Doppler velocimetry device is selective. To facilitate the velocity information from the Doppler frequency shift waveform, the following processing of the received acoustic signal is required:

1. The received signal consists of a mixture of the transmitted signal and the frequency-shifted signal.

Figure 2-12 below shows the process of extracting the frequency-shifted information.

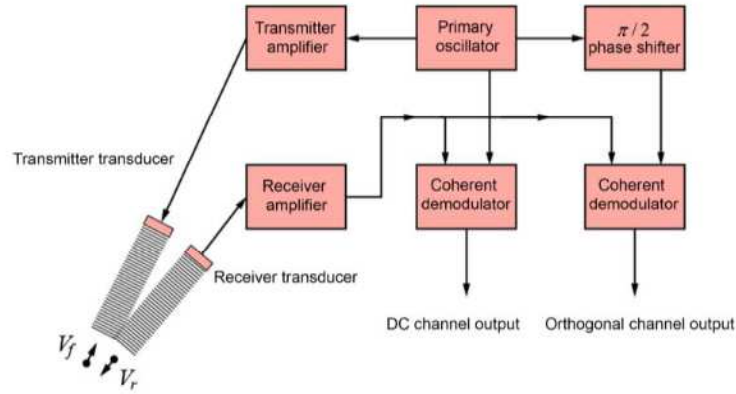


Fig. 2-12 Phase quadrature demodulation

In this process, many combinations of addition and subtraction of frequency signals are obtained, where the subtracted signal frequency does not exceed Δf , and the summed signal frequency does not exceed f_s . When all signals are passed through a low-pass filter, only the Doppler shift signal is retained.

2. Phase-domain demodulation allows the separation of frequency-shifted up-shifted signals from down-shifted signals.

3. Quantization calculation of the frequency of the analogue signal.

The three steps of the signal processing process can be achieved using zero crossing detection (ZCD) and the Fourier transform.

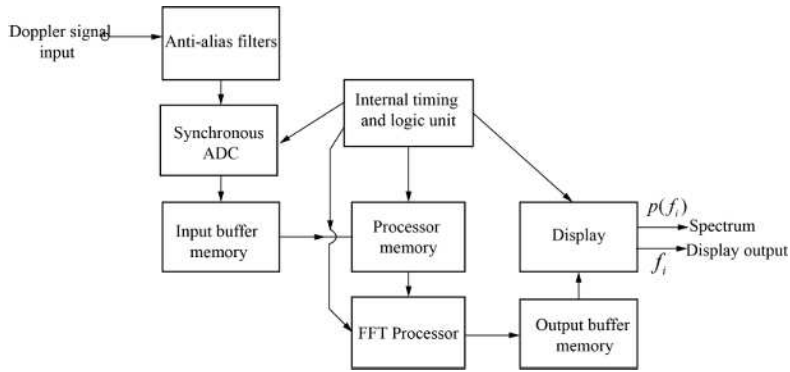


Fig. 2-13 Fast Fourier transform of Doppler signal

Continuous wave Doppler detection devices can transmit and receive signals continuously without spatial resolution, so that the location of the velocity measurement cannot be determined. Therefore, for a given continuous wave spectrum, the velocity needs to be presented over the entire supersonic range, so that peak signals can be read without regard to where the maximum value is obtained at the supersonic velocity.

2.4.3 Detection of umbilical artery blood signal

Using the Doppler effect of the relative motion of the blood flow and the probe, the angle of relative motion and the magnitude and sign of the frequency shift can be measured using an umbilical flowmeter with a 4MHz probe, which in turn can be used to derive the velocity and distribution of the umbilical artery blood, and finally, combined with imaging and digital signal processing techniques to form an acoustic spectrum of the umbilical artery blood [27]. The peak-to-valley ratio S/D, resistance index RI and pulsatility index PI of blood flow can be calculated according to hemodynamic theory and calculate the peak-to-valley ratio S/D, resistance index RI and pulsatility index of the blood flow according to the hemodynamic theory PI and other indicators.

The Doppler ultrasound probe emits an ultrasound signal with a frequency of ω_0 to the fetal umbilical artery and the probe receives an ultrasound echo signal of U , the superposition expression of this mixed signal is:

$$U = U_1 + U_2 = a \cos \omega_0 t + \sum_i b_i \cos(\omega_0 + \Omega_i)t \quad (2-28)$$

Where: a and b are the amplitudes of the signals ω_0 and $\omega_0 + \Omega_i$ respectively; Ω_i is the Doppler frequency; i represents the i th red blood cell in the umbilical artery. $U_1 = a \cos \omega_0 t$ is the acoustic and electrical leakage signal between the internal emission and reception of the probe and the

reflection from the human tissue interface; $U_2 = \sum_i b_i \cos(\omega_0 + \Omega_i)t$ is the Doppler shift signal of the umbilical artery blood [28].

A block diagram of the umbilical artery blood detection system is shown in Figure 2-14 below:

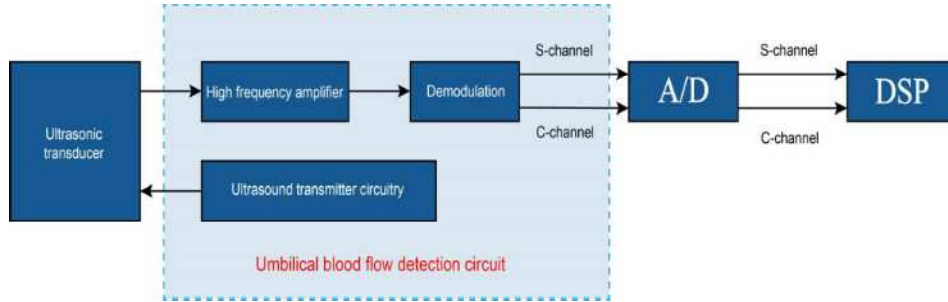


Fig. 2-14 Block diagram of umbilical artery blood monitor system

2.5 Acquisition of umbilical artery blood signal

2.5.1 Acquisition equipment

Clinical data were collected in Ehu Branch of Xishan People's Hospital, Wuxi, Jiangsu Province, China, using the MDF-OBM umbilical artery blood detecting device (Fig.2-15). The device includes umbilical blood detection software V2.3, a 4.0 MHz-CW continuous wave Doppler probe (Figure 2-16) and a high-performance PC with a sampling frequency of 11025 Hz.



(a) Side view



(b) Rear view

Fig. 2-15 Umbilical artery blood diagnostic system

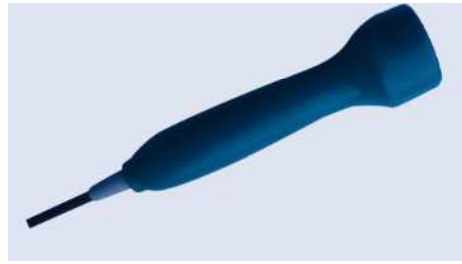


Fig. 2-16 4.0 MHz continuous wave Doppler probe

The continuous Doppler probe specification parameters are shown in Table 2-2.

Table 2-2 Probe Parameters

| No. | Parameters | Values |
|-----|--|------------------------------------|
| 1 | Nominal Frequency | 4.0MHz |
| 2 | Working frequency | (4.0±10%) MHz |
| 3 | Peak negative sound pressure | $P.<1\text{MPa}$ |
| 4 | Output beam sound intensity | $I_{ab}<30\text{mW/cm}^2$ |
| 5 | Spatial peak time-averaged sound intensity | $I_{spta}<200\text{mW/cm}^2$ |
| 6 | Ultrasonic output intensity | $I_{sata}<30\text{mW/cm}^2$ |
| 7 | Working mode | Continuous wave ultrasound Doppler |
| 8 | Effective ultrasonic emission area | (31.8±15%) mm ² |

2.5.2 Signal acquisition process

The umbilical artery blood signals of pregnant women with different ages, different gestational weeks and with or without pathological features were used as the study subjects. The acquisition process was as follows:

1. Preparation: turn on the detecting device and enter the measurement state.
2. Monitoring: The pregnant woman is in supine or semi-recumbent position with the abdomen exposed. Place the probe on the contralateral side where the stronger fetal heart sounds are heard and look for the umbilical artery site probe side. One strand of the umbilical artery is on the side of the fetal limb, and only by placing the probe in the best position can we obtain a good quality signal of umbilical artery blood signal.



Fig.2-17 Diagnostic chart of umbilical artery blood

3. Data acquisition

(1) In the real-time monitoring display section of the umbilical blood detection system MFM-OBM. A typical umbilical artery blood spectrogram appears on the screen and freezes this image. The peak - trough values of 10 consecutive wave patterns are measured, their average value is taken, and the value is automatically displayed.

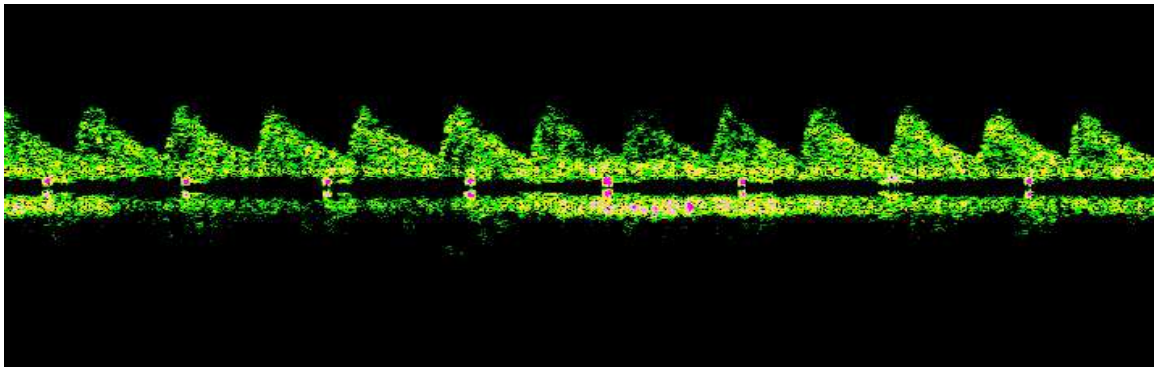


Fig.2-18 Acoustic spectrum of umbilical artery blood

In Figure 2-18 above, the umbilical artery blood sonogram display area shows the umbilical artery blood spectrum signal in real time, with the horizontal coordinate indicating the acquisition time (s) and the vertical coordinate indicating the umbilical artery blood velocity (cm/s).

The spectrum display area shows the searched umbilical blood spectrum as shown in Figure 2-19 below. The umbilical artery blood display box on the right will show the calculated parameters for the selected monitoring record, including S/D, PI, RI, FVR, FHR (fetal heart rate) and calculated cycles.

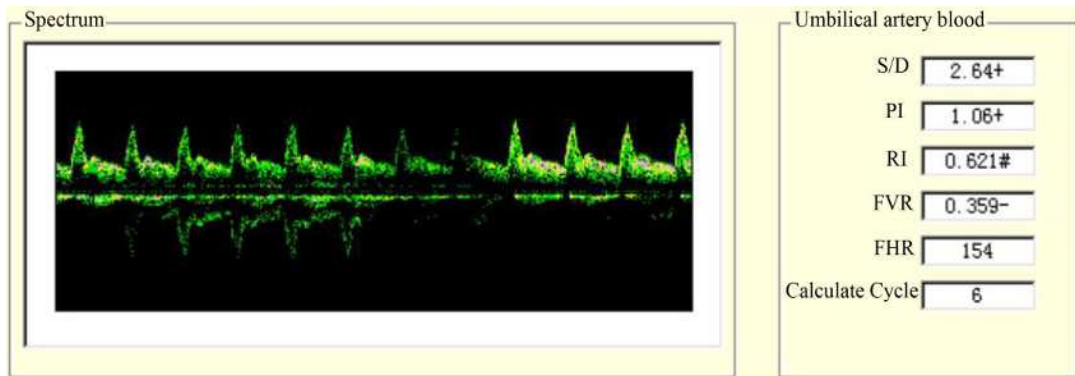


Fig2-19 Acoustic spectrum of umbilical artery blood with measured parameters

(2) Extraction of the envelope for umbilical artery blood sonograms

1. Convert the acquired colored sonograms to grey scale.
2. Scan the grey-scale sonograms point by point from left to right and from top to bottom to find the points with different pixels from the first adjacent point in each column.
3. Mark the coordinates of these points and connect all the points to obtain the outer envelope of the sonograms, as shown in Figure 2-20 below, which shows the umbilical artery blood velocity curve signal extracted by the above method.

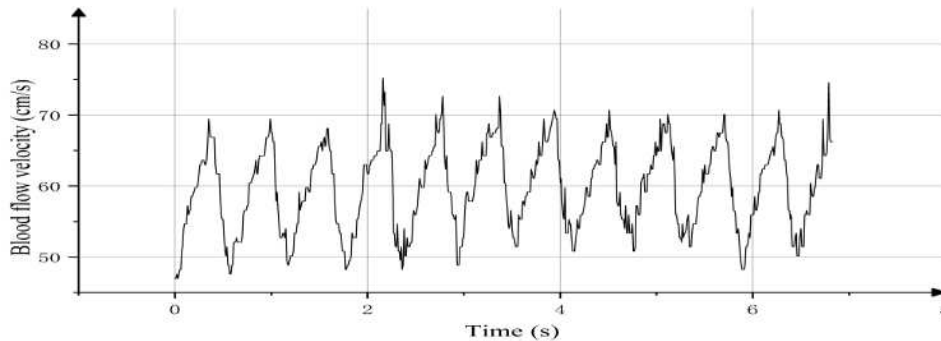


Fig. 2-20 Time series signal of umbilical artery blood

2.5.3 Ethics

This study was approved by the Clinical Ethics Committee of Ehu Branch of Xishan People's Hospital (2018-EHIRB-001), and written informed consent was obtained. All participants signed informed consent forms prior to the study.

2.5.4 Database of umbilical artery blood signals

According to the principle and method of umbilical artery blood signal acquisition, umbilical artery blood signals of 104 pregnant women aged between 22 and 43 years old and between 26 and 40 weeks of

gestation were collected from March to July 2020. Another 198 umbilical artery blood signals were collected from January 2021 - July 2021. The data collected were compared using a Philips IU-22 color Doppler ultrasound machine to derive the fetal health status. The signals are classified as normal, abnormal, and other unspecified conditions(12 cases), and the abnormal status was classified into three conditions: umbilical cord around neck, oligohydramnios, and fetal malposition. The number of cases for normal and abnormal signals is shown in the table 2-3 below.

Table 2-3 Number of signals for four conditions

| Lable | Status | Number of cases |
|--------------|----------------------------|------------------------|
| 1 | Normal state | 178 |
| 2 | Oligohydramnios | 38 |
| 3 | Umbilical cord around neck | 40 |
| 4 | Fetal malposition | 34 |

The normal fetal umbilical artery blood signal tracing chart and the abnormal fetal umbilical artery blood signal tracing chart are shown in Tables 2-4 and 2-5 below respectively.

Table 2-4 Sample of normal fetal umbilical artery blood signal tracking record sheet

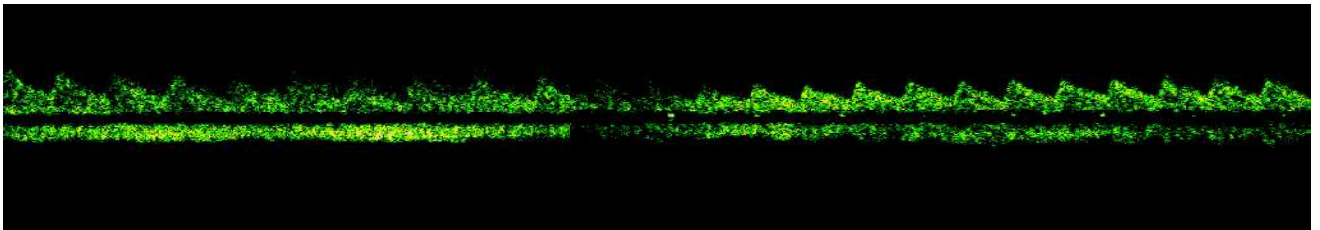
| No | Name | Gestation week | PI | RI | S/D | Acoustic Spectrogram No. | Signal Serial No. |
|-----------|-------------|-----------------------|-----------|-----------|------------|---------------------------------|--------------------------|
| 1 | 李** | 21 | | | | N1—21 | S1—21 |
| | | 22 | | | | N1—22 | S1—22 |
| | | 23 | | | | N1—23 | S1—23 |
| | | 24 | | | | N1—24 | S1—24 |
| | | 25 | | | | N1—25 | S1—25 |
| | | 26 | | | | N1—26 | S1—26 |
| | | 27 | | | | N1—27 | S1—27 |
| | | 28 | | | | N1—28 | S1—28 |
| | | 29 | | | | N1—29 | S1—29 |
| | | 30 | | | | N1—30 | S1—30 |
| | | 31 | | | | N1—31 | S1—31 |
| | | 32 | | | | N1—32 | S1—32 |
| | | 33 | | | | N1—33 | S1—33 |
| | | 34 | | | | N1—34 | S1—34 |
| | | 35 | | | | N1—35 | S1—35 |
| | | 36 | | | | N1—36 | S1—36 |
| | | 37 | | | | N1—37 | S1—37 |
| | | 38 | | | | N1—38 | S1—38 |
| | | 39 | | | | N1—39 | S1—39 |
| | | 40 | | | | N1—40 | S1—40 |

Table 2-5 Sample of abnormal fetal umbilical artery blood signal tracking record sheet

| No | Name | Gestation week | PI | RI | S/D | Acoustic Spectrogram No. | Signal Serial No. |
|----|------|----------------|----|----|-----|--------------------------|-------------------|
| 1 | 张** | 21 | | | | AN1—21 | AS1—21 |
| | | 22 | | | | AN1—22 | AS1—22 |
| | | 23 | | | | AN1—23 | AS1—23 |
| | | 24 | | | | AN1—24 | AS1—24 |
| | | 25 | | | | AN1—25 | AS1—25 |
| | | 26 | | | | AN1—26 | AS1—26 |
| | | 27 | | | | AN1—27 | AS1—27 |
| | | 28 | | | | AN1—28 | AS1—28 |
| | | 29 | | | | AN1—29 | AS1—29 |
| | | 30 | | | | AN1—30 | AS1—30 |
| | | 31 | | | | AN1—31 | AS1—31 |
| | | 32 | | | | AN1—32 | AS1—32 |
| | | 33 | | | | AN1—33 | AS1—33 |
| | | 34 | | | | AN1—34 | AS1—34 |
| | | 35 | | | | AN1—35 | AS1—35 |
| | | 36 | | | | AN1—36 | AS1—36 |
| | | 37 | | | | AN1—37 | AS1—37 |
| | | 38 | | | | AN1—38 | AS1—38 |
| | | 39 | | | | AN1—39 | AS1—39 |
| | | 40 | | | | AN1—40 | AS1—40 |

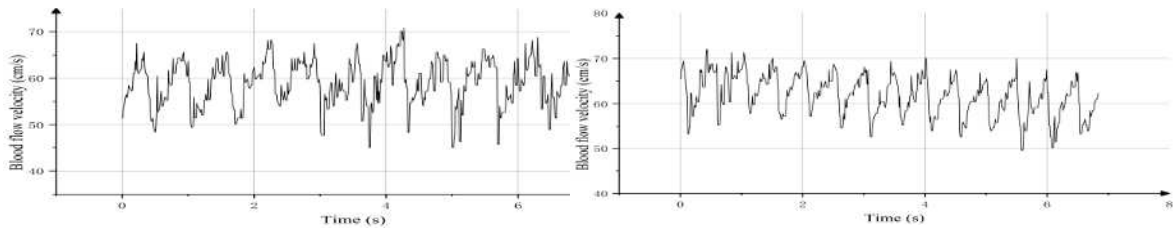
2.6 Problems with conventional parameters

Figure 2-21 below shows an example of two cases whose values for the three conventional parameters are shown in Table 2-6. According to the parameter reference criteria in the previous sections 2.3.1, the values of all three conventional parameters of (a) and (b) are within the normal range and both should be diagnosed as normal. However, the actual situation is that the left one is an abnormal case named umbilical cord around neck. This shows that it is not possible to fully distinguish between normal and abnormal by the conventional three parameters.



(a) Acoustic spectrum of abnormal case (umbilical cord around the neck)

(b) Acoustic spectrum of normal case



(c) Envelope curve of abnormal case (umbilical cord around the neck) (d) Envelope curve of abnormal case

Fig. 2-21 Normal and abnormal cases with similar parameter values

Table 2-6 Three conventional parameters values of abnormal case and normal case

| Parameter values of abnormal case | | | Parameters values of normal case | | |
|-----------------------------------|-------|-------|----------------------------------|-------|-------|
| S./D | PI | RI | S./D | PI | RI |
| 3.726 | 1.322 | 0.612 | 3.454 | 1.406 | 0.692 |

What could generate the clinical misclassification? These reasons are: 1. Conventional parameters only consider the maximum, minimum and average values of blood velocity within a certain period, ignoring the phase features of the signal: e.g., phase delay, phase frequency, phase mode; 2. The values derived from the S/D, RI and PI are independent of each other and do not integrate these phase features.

Physiological signals such as electrocardiograms (ECG) signals and electroencephalograms (EEG) signals are quasi-periodic time-varying signals that exhibit complex periodic variations, and that these signals are highly non-linear and non-stationary, i.e., their vibrational modes and amplitudes may change significantly in time. Currently, fractal theory and Chaos based on phase space reconstruction are widely used in the processing of physiological signals such as ECG and EEG with good results.

Considering fractal and chaotic analysis methods not only focuses on the amplitude change of blood velocity. By considering these phase features together, we can have a more comprehensive understanding of umbilical artery blood signals. A detailed description of the application of chaos theory and fractals to the study of umbilical artery blood signals is given in Chapter 3 to Chapter 5.

2.7 Summary

1. The fundamentals of fetal hemodynamics are described, including the fetal circulation, placental developmental processes and the physiological characteristics of the umbilical cord. A brief introduction to the mechanics of the umbilical artery waves that produce the umbilical velocity waveform.

2. The clinical means of umbilical artery blood signal parameters and normal reference values such as S/D, PI and RI are illustrated.

3. Acquisition of umbilical artery blood signals and monitoring data: The Doppler effect, the principle of ultrasound Doppler velocimetry and the principle of umbilical artery flow signal detection hardware are

described. Based on the discussion of umbilical blood acoustic spectrograms, details of the umbilical artery Doppler signal data acquisition equipment, data classification, acquisition process and the establishment of the umbilical artery blood signal and detection database are presented.

4.The problem of misdiagnosis caused by conventional parameters is raised and the rationale for analysing umbilical artery blood signals by fractal versus chaotic methods is described

2.8 References

- [1] Feng Y Z; translated by Dai K G. Biokinetics of blood circulation [M]. Changsha: Hunan Science and Technology Press, 1986.
- [2] Liu Z.R, Li S S. Principles and methods of hemodynamics [M]. Shanghai: Fudan University Press, 1997.
- [3] Sakai, KY, Hashimoto, Shōji. 3D human anatomy drawings [M]. Shenyang: Liaoning Science and Technology Press, 2013.
- [4] Yu X M, Yuan Y H. Fundamentals of anatomy [M]. Beijing: People's Military Medical Press, 2015: 241-242.
- [5] Cross J C, Simmons D G, Watson E D. Chorioallantoic Morphogenesis and Formation of the Placental Villous Tree[J]. Annals of the New York Academy of Sciences, 2010,995(1): 84-93.
- [6] Regnault T R H, Galan H L , Parker T A , et al. Placental Development in Normal and Compromised Pregnancies-A Review[J]. Placenta, 2002,23(supp-SA): S119–S129.
- [7] Wang Y, Shuang Z. Placental Blood Circulation - Vascular Biology of the Placenta- NCBI Bookshelf[J]. Morgan & Claypool Life Sciences, 2010.
- [8] Brosens I , Robertson W B , Dixon H G . The physiological response of the vessels of the placental bed to normal pregnancy[J]. The Journal of pathology and bacteriol, 1967,93(2): 569-579.
- [9] Kaufmann P, Black S, Huppertz B. Endovascular Trophoblast Invasion: Implications for the Pathogenesis of Intrauterine Growth Retardation and Preeclampsia[J]. Biology of Reproduction, 2003,69(1): 1-7.
- [10] Georgiades P, Ferguson-Smith A C , Burton G J . Comparative Developmental Anatomy of the Murine and Human Definitive Placentae[J]. Placenta, 2002,23(1): 3-19.
- [11] Stafford I A, Dashe J S, Shivvers S A, et al. Ultrasonographic cervical length and risk of hemorrhage in pregnancies with placenta previa[J]. Obstetrics & Gynecology, 2010,116(3):595-600.
- [12] Meyer W W, Lind J. Iliac arteries in children with a single umbilical artery: Structure, calcifications, and early atherosclerotic lesions[J]. Archives of Disease in Childhood, 1974,49(9): 671-679.
- [13] Boyd P A. Quantitative structure of the normal human placenta from 10 weeks of gestation to term.[J]. Early Human Development, 1984,9(4): 297-307.
- [14] Hua K Q, Feng Y J. Practical obstetrics and gynecology (fine) [M]. Beijing:People's Health Publishing House, 2013.

- [15] Chen Z N, Du X G, Liu B N. Obstetrics and gynecology pathology [M]. Shanghai: Shanghai Medical University Press, 1996.
- [16] Milnor W, Hemodynamics[M]. Williams & Wilkins, 1982.
- [17] Nichols W, O'Rourke M, Vlachopoulos C. McDonald's blood flow in arteries: theoretical, experimental, and clinical principles[M]. CRC Press, 2011.
- [18] Zamir M. The Physics of Coronary Blood Flow[M]. Springer US, 2005.
- [19] Qin T W. Fundamentals of clinical biomechanics. Beijing: Military Medical Science Press, 2015: 51-52.
- [20] Segers P, Rietzschel E R, De Buyzere M L, et al. Noninvasive (input) impedance, pulse wave velocity, and wave reflection in healthy middle-aged men and women[J]. Hypertension, 2007,49(6): 1248-1255.
- [21] Adamson S L, Whiteley K J, Langille B L. Pulsatile pressure-flow relations and pulse-wave propagation in the umbilical circulation of fetal sheep[J]. Circulation Research, 1992,70(4): 761-772.
- [22] Serge Vulliémoz, Stergiopoulos N, Meuli R. Estimation of local aortic elastic properties with MRI[J]. Magnetic Resonance in Medicine, 2002,47(4): 649-654.
- [23] Guo F J, Fan Z P, Tian J Y, et al. Clinical value of uterine artery Doppler flow monitoring in pregnant women with hypertensive disorders during pregnancy[J]. China Maternal and Child Health Care, 2016,31(13):2592-2593.
- [24] Lin Q H. Difficult obstetrics and gynecology [M]. Wuhan: Hubei Science and Technology Press, 2002: 198-199.
- [25] Zhang Y P, Yu J H, Wang X, et al. Correlation analysis of ultrasound detection of fetal hemodynamic changes in pregnant women with gestational hypertension and pregnancy outcome[J]. Journal of Medical Imaging, 2018,28(2): 308-312.
- [26] Zhang H L. Theoretical acoustics [M]. Beijing: Higher Education Press, 2007: 303-304.
- [27] Tang S H. Fetal ultrasound Doppler umbilical cord flowmetry detection principles and maintenance[J]. China Medical Device Information, 2012(12): 68-70.
- [28] Xu J F, Lu Y S. Study of fetal umbilical blood flow detection circuit[J]. Medical and Health Equipment, 2014, 35(2): 4-7.

Chapter 3

Fractal characterization of umbilical artery blood signal

In this chapter, the fractal dimension of the umbilical artery blood signal is calculated and analyzed to investigate the differences between normal and abnormal umbilical artery blood signals based on the non-linear theory and to reveal the fractal characteristics of the umbilical artery blood signal.

3.1 Foundations of fractal theory

Smooth geometric shapes are mathematically continuous and differentiable everywhere and are the object of classical Euclidean geometry. But things that exist in nature have the everywhere continuous but non-differentiable nature of nature, such as colorful clouds, complex intertwined blood vessels, undulating mountains, leafy trees, rough and uneven surfaces, flying snowflakes and fluctuating stock markets. The creation of fractal geometry has made it possible to explain and solve many of nature's complex phenomena, as traditional classical mathematical tools are no longer able to describe nature's physical objects with certainty.

Fractal geometry has had a profound impact on the development of the natural and social sciences, with applications covering the fields of medicine, biology, management, philosophy, computing, chemistry, architecture, materials, physics, economics, and mathematics, in addition to the sciences, and even the arts such as music, art and film [1].

3.1.1 Definition of fractal

In 1967, the American mathematician Mandelbrot published the article "How long is the coastline of Britain" in *Science*, marking the birth of the concept of fractals [2], and in 1973 and 1975 Mandelbrot introduced the idea of fractal geometry and the term "Fractal" [3]. In 1977 and 1982, Mandelbrot's two classic books on fractal theory marked the birth of fractal geometry as a separate discipline [4-5].

Fractal geometry is closer to the nature of the world, it is a science that studies infinitely complex figures of nature with a certain self-similarity as well as structures.

Falconner describes fractals as follows [6]:

1. The fractal dimension is greater than its topological dimension.
2. Have approximate or statistically significant self-similarity.
3. Have arbitrarily small ratios of detailed and fine structure.
4. Cannot be expressed both locally and comprehensively in terms of traditional geometric languages.

5. Can be generated in most cases by iteration, recursion, etc.

Also, there are many researchers who believe that fractals are visually detected, and it is difficult to make a rigorous proof of them. There is also a widely accepted view in domestic and international research that, based on a qualitative understanding of the self-similarity of the object of study, determines whether it is a fractal based on the presence or absence of a series of scale-free intervals in a double logarithmic curve $\ln N(\varepsilon) - \ln \varepsilon$. Figure 3-1 below shows a typical self-similarity graph.

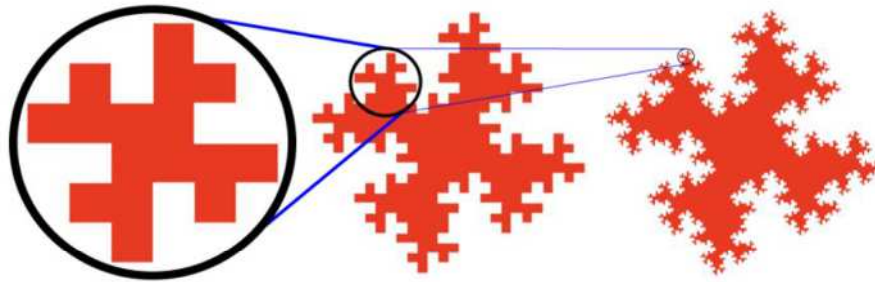


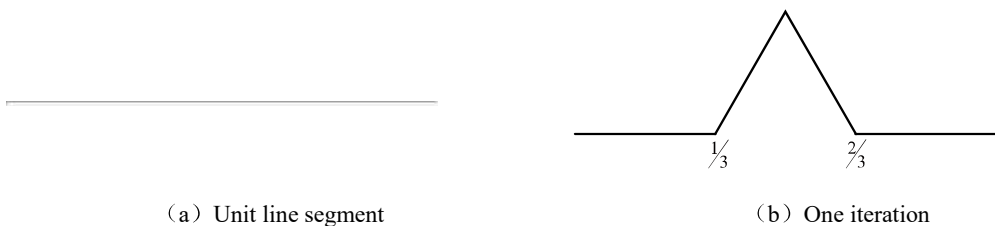
Fig. 3-1 Self-similar graph

3.1.2 Classical fractal structure

Fractal research subjects are typically discovered in the natural world. Koch curves, Cantor sets, Sierpinski triangular cushions, and other typical symmetric fractals are listed here. They are also referred to as “regular” fractals because deterministic mathematical techniques were used to create each one. The next sections will use two examples of traditional fractal structures to further clarify the idea of fractals.

1. Koch Curve

The Koch curve is built as depicted in Figure 3-2 and was discovered by the Swedish physicist Helge von Koch. A line segment of length unit 1 in the two-dimensional plane is illustrated in Figure 3-2(a); in step 1, the segment is trisected, the middle third is removed, and is then replaced with the other two sides of an equilateral triangle with a side length of $1/3$, yielding Figure 3-2. (b); in step 2, each line segment in Figure 3-2(b) is trisected again according to step 1 and continues to be replaced with the other two sides of an equilateral triangle of side length $1/3^2$, resulting in Figure 3-2(c). the process is then repeated numerous times to obtain a Koch curve with numerous turning points, continuous at all points but not derivable at all.



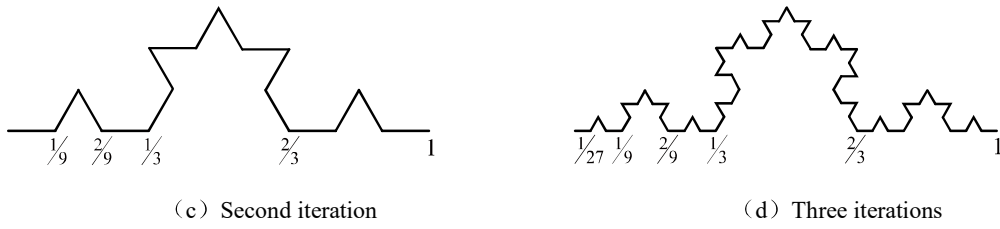


Fig. 3-2 Koch Curve

2. Sierpinski shim

In 1916, the Polish mathematician Sierpinski proposed a method of fractal generation[7]. The iterative operation was repeated for the equilateral triangle shown in Figure 3-3(a): connecting the midpoints of each side of the equilateral triangle, dividing it equally into four smaller equilateral triangles, removing the smaller triangle at the centre (shown in Figure 3-3(b)), and repeating the above operation over and over again, the final figure obtained was the Sierpinski shim.

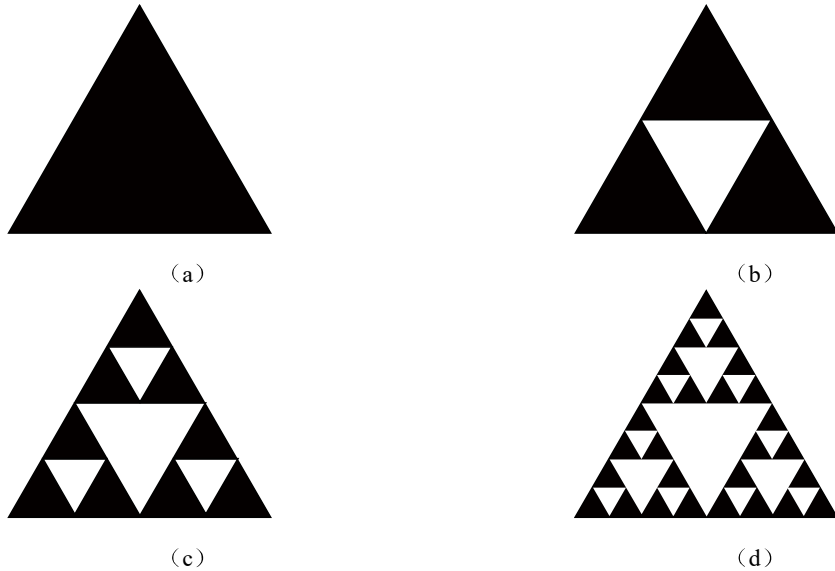


Figure 3-3 Sierpinski shims

Both sets of figures above have the characteristic that each part is similar in shape to the figure itself, which is called self-similarity. The formation of such figures is characterized by the fact that they can be generated iteratively by a certain defined rule. However, objects in nature are by no means truly and simply symmetrical, and therefore the above figures are not truly representative of objects in nature. Nonetheless, they adequately represent the basic features of fractal things, such as self-similarity and scale-invariance.

3.1.3 Fractal dimension

Dimension is the number of independent coordinates needed to determine the position of a point in a geometric object, and it is an important characteristic quantity for describing geometric objects. In Euclidean space, dimension is a natural number [9], while the fundamental covariate for quantitatively describing a fractal

in a non-linear system is the fractal dimension, which is a fraction or decimal between integers, usually exceeding its topological dimension, and is an invariant under the scalar transformation [10]. The topological dimension of a curve is 1, as shown in Figure 3-4, and the size of the fractal dimension varies for different types of curves as the complexity of the curve increases.

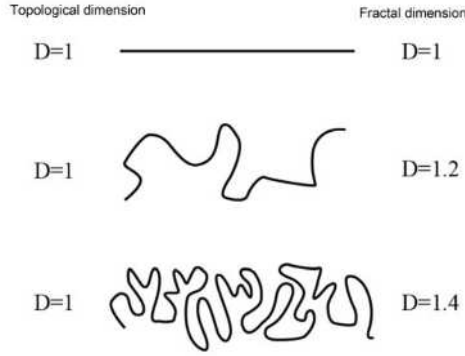


Figure 3-4 Fractal dimension of different types of curves with increasing complexity

Fractal dimension describes the fractal characteristics of complex things in numerical form, which is convenient, concise, and intuitive. One can make quantitative judgments and distinctions about the fractal characteristics of things by means of numerical values as well as analyze the fractal characteristics of different things by means of specific numerical values [11].

Definitions of fractal dimensions include Hausdorff dimension, self-similarity dimension, information dimension, correlation dimension, box dimension and Lyapunov dimension [12]. Among them, box dimension and correlation dimension are most used in time series nonlinear analysis [13].

1. Hausdorff dimension

The theoretical basis for the measurement of fractal dimensionality is the theory of Hausdorff's dimensionality, founded by F. Hausdorff.

Let a subset class on a metric space (X, ρ) of finite diameter not exceeding δ be $\{U_i\}$ and Y be a subset on X , if $Y \subset \bigcup_{i=1}^{\infty} U_i$, then the subset class $\{U_i\}$ is said to be a δ cover of the set Y .

Let Y be any bounded subset of the metric space (\mathbb{R}^d, ρ_E) , $s \geq 0$, and for any $s \geq 0$, define:

$$H_{\delta}^s(Y) = \inf \left\{ \sum |U_i|^s : \{U_i\} \right\} \quad (3-1)$$

where $\{U_i\}$ is a δ cover of the set Y , which denotes the diameter of the set U_i . As the value of δ becomes smaller, the coverage class of δ - that can cover Y becomes smaller. Thus the value of $H_{\delta}^s(Y)$ is non-decreasing, so the limit is the Hausdorff dimension.

$$H^s(Y) = \lim_{\delta \rightarrow \infty} H_\delta^s(Y) \quad (3-2)$$

Theorem 3-1 Let the set Y be a finite subset of the metric space (\mathbb{R}^d, ρ_E) , then there exists a unique real value $s_0 \in [0, d]$ such that:

$$H^s(Y) = \begin{cases} \infty, & s < s_0 \\ 0, & s > s_0 \end{cases} \quad (3-3)$$

Definition 3-2 Let the set Y be a subset of the metric space (\mathbb{R}^d, ρ_E) , the unique real number s_0 determined by Theorem 3-1 is called a Hausdorff dimension and is denoted $\dim_H Y = s_0$.

2. Self-similarity dimension

Self-similarity can be assessed in a quantitative way by using the fractal dimension. In the finer resolution case, the self-similarity dimension describes how many new fractals are observed that are geometrically like the whole object. This fractal dimension can be defined by extending one of the classical self-similarity sets, such as line segments, planes, or cubes.

If we use a factor F to change the scale and have N segments similar to the original, then give the self-similarity dimension D_{self} as:

$$N = F^{D_{self}} \quad (3-4)$$

$$D_{self} = \ln N / \ln F \quad (3-5)$$

3. Information dimension

Let p_i represent the probability that a fractal set belongs in the cover U_i , then the information dimension is:

$$\dim_I = \lim_{\delta \rightarrow 0} \frac{\sum_{i=1}^N p_i \ln p_i}{\ln \delta} \quad (3-6)$$

From the definition of the information dimension \dim_I it follows that:

$$S(\delta) = - \sum_{i=1}^N p_i \ln p_i \quad (3-7)$$

3-7 is the Shannon entropy of the system, then the information dimension \dim_I can also be written as:

$$\dim_f = -\lim_{\delta \rightarrow 0} \frac{S(\delta)}{\ln \delta} \quad (3-8)$$

4. Box dimension

Box dimension is a metric parameter used to describe the irregularity of complex images. It can be applied not only to one-dimensional time series analysis, but also to two-dimensional images, which has become a widely used method to calculate fractal dimension [14]. The box counting method proposed by Chaudhuri and Sarkar expressed the fractal dimension as [15]:

$$D = \ln(N_r) / \ln(1/r) \quad (3-9)$$

Where: D is fractal dimension, r is grid scale, N_r is total number of boxes.

The calculation principle of box dimension is as follows: divide the image with squares of different scales to obtain the effective number of covering squares of the image, and constantly change the size of the squares to count the number of covering squares of the corresponding size to form a series of points. The fractal box dimension of the image is the slope of the line obtained by linear fitting of these points. The calculation principle is shown in Fig.3-5: set the side length of the square box as 1, which contains the whole Sierpinski triangle gasket. The triangle gaskets are covered by 1/2, 1/4, and 1/8... square boxes with side length respectively, and boxes with side length r_i are obtained one by one, r_i is called grid scale.

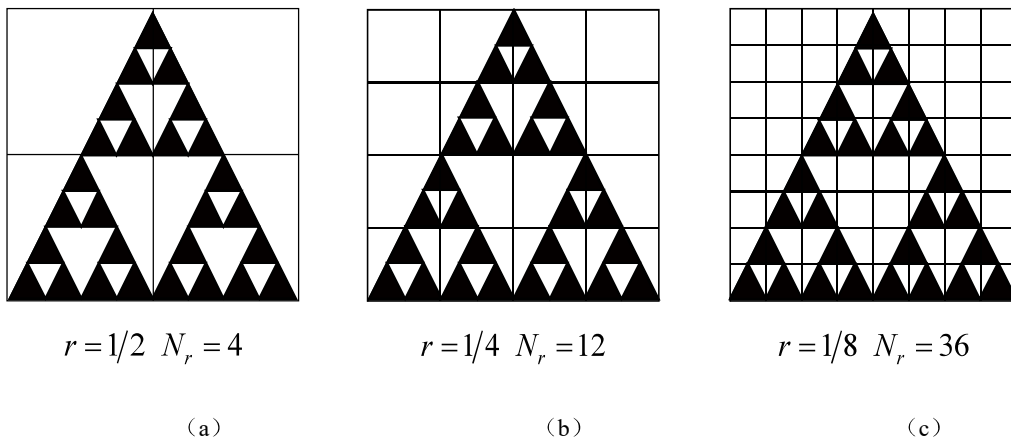


Fig.3-5 Sierpinski triangle gasket box counting method

The box counting algorithm is as follows: first, determine a series of side lengths and sizes as r_i and then calculate the number of boxes covering the full form with this series of boxes $N(r_i)$, and finally $\ln(1/r_i)$ and $\ln(N_r)$ corresponding to different grid scales r_i are obtained, namely, the fractal dimension. The results are shown in Table 3-1.

Tab.3-1 Calculation statistical table for box dimension method

| i | 0 | 1 | 2 | ... | n |
|---------------|---------------|---------------|---------------|-----|---------------|
| r_i | r_0 | r_1 | r_2 | ... | r_n |
| $N(r_i)$ | $N(r_0)$ | $N(r_1)$ | $N(r_2)$ | ... | $N(r_n)$ |
| $\ln(1/r_i)$ | $\ln(1/r_0)$ | $\ln(1/r_1)$ | $\ln(1/r_2)$ | ... | $\ln(1/r_n)$ |
| $\ln(N(r_i))$ | $\ln(N(r_0))$ | $\ln(N(r_1))$ | $\ln(N(r_2))$ | ... | $\ln(N(r_n))$ |

The least square method is used to linearly fit the data set $(\ln(1/r_i), \ln(N(r_i)))$, and the straight line as shown in Figure 3-6 is drawn in the logarithmic coordinates. The slope obtained is the fractal dimension D . $\ln(1/r_i) \ln(N(r_i))$, the algorithm process of calculating fractal dimension of image based on MATLAB is as follows: the image file is read for image gray processing; After edge picking and binarization, the box counting method calculates a series of “square grids with side length (r_i)” and the logarithmic data group $(\ln(1/r_i), \ln(N_r))$ corresponding to “number of covered grids ($N(r_i)$)”. After linear fitting, its slope is the fractal dimension (D) of the image. The calculation process is shown in Figure 3-7.

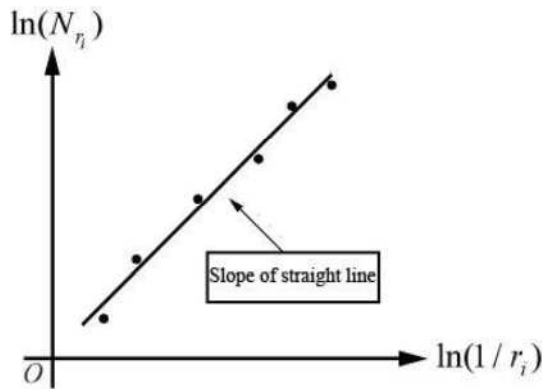


Fig.3-6 Diagram of box dimension calculation

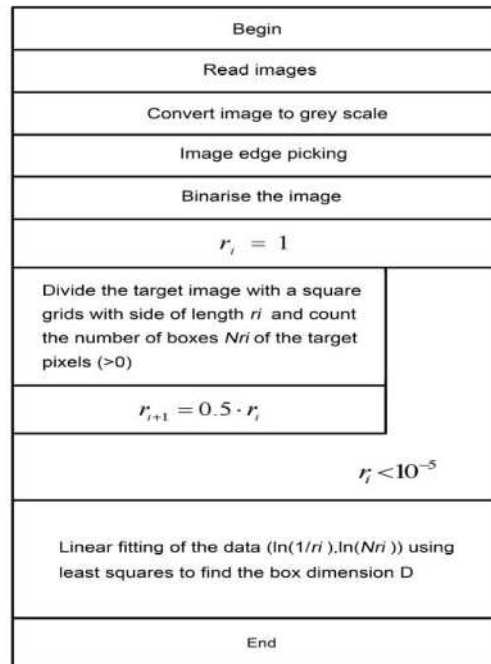


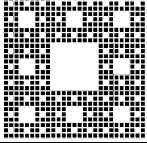
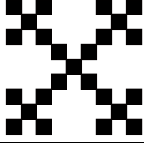
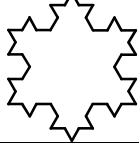



Fig.3-7 Box dimensional program running N-S flow

Although the principle of box counting is very mature and widely used, the dimension in the algorithm is more delicate. Because of the large number of iterations and loops in the program compilation, a small error at one step will lead to a large difference between the final calculation result and the actual result. A regular fractal image with known theoretical fractal dimension is used to calculate its fractal

dimension by the box counting method and compare it with the theoretical fractal dimension to check the accuracy of the box counting method, and the results are shown in Table 3-2 below.

Table 3-2 Fractal dimensions of regular fractal geometry

| Images |  |  |  |  |  |  |
|------------------------|---|---|---|--|---|---|
| Name | Straight line | Square | Sierpinski spacers | Vicsek graphics | Koch Snowflake | Sierpinski triangular shims |
| Theoretical dimension | 1 | 2 | 1.8928 | 1.4650 | 1.2618 | 1.5850 |
| Calculating dimensions | 0.9938 | 1.9422 | 1.7430 | 1.4452 | 1.3468 | 1.6289 |
| Error | 0.0062 | 0.0289 | 0.0791 | 0.0135 | 0.0674 | 0.0277 |

Comparing the theoretical and computed values of the dimensional box dimensions of the graphs in Table 3-2 above shows that there is some error in the computed values. There are two reasons for the error: (1) the limited amount of computation makes the calculated values only exist as an approximation to the theoretical ones; (2) the theoretical fractal image contains infinite details, while the specific fractal image has limited details, thus causing some error.

5. Correlation dimension

The correlation dimension (CD) is an important parameter for describing the non-linear characteristics of a system and is used to characterize the fractal complexity of attractors in phase space. The CD reflects the correlation of the data points in the set in terms of point-to-point correlation. The CD has the advantage that the attractor dimension of a non-linear time series can be calculated directly from the time series data obtained from systematic observations alone, which makes it very useful for a wide range of practical applications.

Complex dynamical systems in a multi-degree-of-freedom space can only measure a single variable in practice, although the motion characteristics are determined by multiple variables. One possible way to understand non-linear dynamical systems is to obtain the geometry of the phase space of the system from real measured one-dimensional time series data, Packard et al. performed phase space reconstruction with time delay technique [16]. Takens reconstruction theorem has proved that the reconstructed system is equivalent to the original system, i.e.: there are intrinsic interactions and connections between the components of a dynamical system during its evolution.

In 1983, Grassberger and Procaccia published an article entitled 'measuring the singularity of strange attractors' [17]. They proposed a method to directly calculate the correlation dimension from time series according to the embedding theory and the idea of phase space reconstruction when analyzing and studying the singularity of attractors, which is G-P algorithm [18]. The principle of the algorithm is as follows:

Let the original signal time series be $\{x_1, x_2, \dots, x_N\}$, then it can be formed a phase space of length N_m and dimension m . m is the embedding dimension of the reconstructed phase space, and the reconstructed phase space matrix can be expressed as:

$$X_i = [x_i, x_{i+\tau}, x_{i+2\tau}, \dots, x_{i+(m-1)\tau}]^T \quad (3-10)$$

Where: τ is the delay time; $i = 1, 2, \dots, N_m$, N_m is the number of vectors in the reconstructed phase space and $N_m = N - (m-1)\tau$. Then:

$$C_r = \frac{1}{N_m^2} \sum_{i=1}^{N_m} \sum_{j=1}^{N_m} H(r - \|X_i - X_j\|) \quad (3-11)$$

where: H is the Heaviside step function, $i \neq j$; $H(x) = \begin{cases} 0 & x \leq 0 \\ 1 & x > 0 \end{cases}$; r is the radius of the hypersphere in phase space and $\|X_i - X_j\|$ is Euclidean distance between the two vectors. C_r is the correlation integral, i.e., the proportion of the total number of point pairs in which the distance is less than r to the total number of point pairs. When $r \rightarrow 0$, the correlation integral C_r has the following relationship with r :

$$\lim_{r \rightarrow 0} C_r \propto r^{D_m} \quad (3-12)$$

where: D_m is CD:

$$D_m = \lim_{r \rightarrow 0} (\ln C_r / \ln r) \quad (3-13)$$

Choosing different embedding dimension m means that one-dimensional time series are embedded into different phase spaces, and the development degree of the system is different.

Therefore, for the same signal sequence, the calculated CD is also different under different embedding dimensions. D_m increases continuously with the increase of m and does not tend to saturation. For deterministic systems, when the embedding dimension increases to a certain value, D_m tends to saturation. In other words, the double logarithm curve of $\ln C_r \sim \ln r$ has a scale-free interval, which indicates that such a time series has fractal characteristics and is the CD of the time series when reaching saturation. At

the same time, the corresponding embedding dimension m_∞ is called saturated embedding dimension, which represents the number of degrees of freedom of the system.

The feasibility analysis and verification of the G-P algorithm is carried out below using the Lorenz system as an example. The Lorenz equation:

$$\begin{cases} dx/dt = \sigma(y - x) \\ dy/dt = x(\rho - z) - y \\ dz/dt = xy - \beta z \end{cases} \quad (3-14)$$

The equation is solved using the fourth-order Runge-Kutta method, with the parameters $\delta=10$, $b = 8/3$, $r = 28$ and initial values $(-1,0,1)$, the sampling time and step size $t = 50\text{ s}$ and $\Delta t = 0.01\text{ s}$ respectively, and the X directional time series with sample length $N = 5000$, which is analyzed for feasibility using the correlation dimension method, and the time series fluctuations are shown in Figure 3-8.

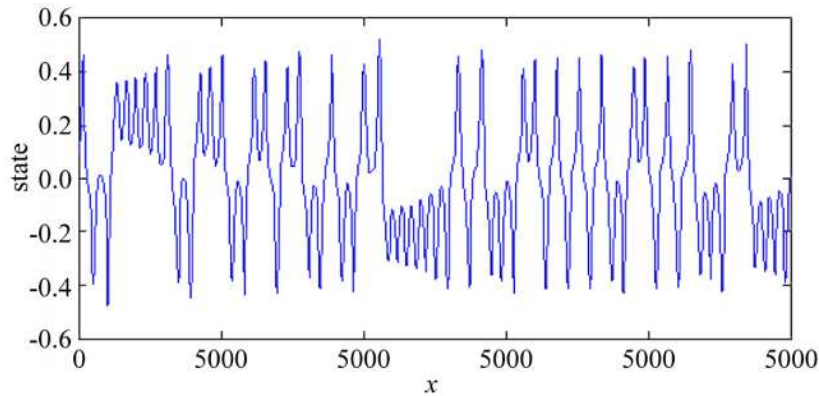
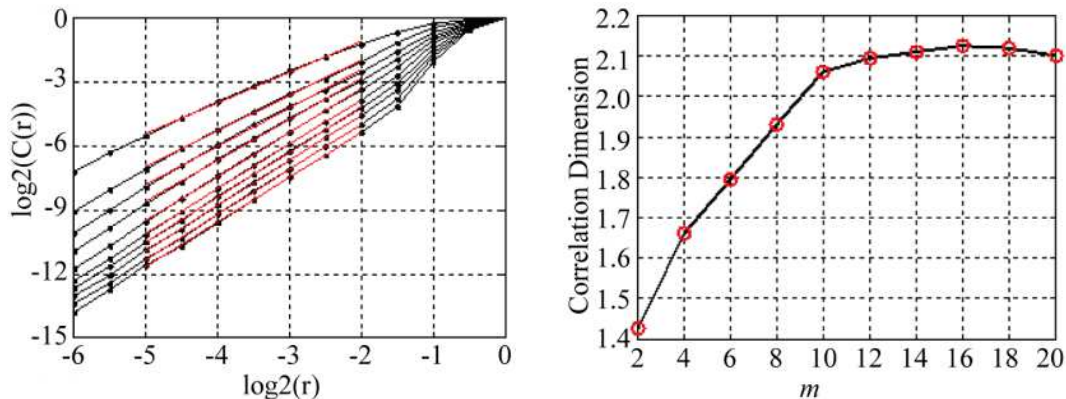


Fig. 3-8 Lorenz system x-direction time series

Based on the G-P algorithm, the embedding dimensions $m = 4, 6, \dots$ and 20 were chosen for the CD analysis of the X-direction time series of the Lorenz system, respectively. Figure 3-9(a) shows the corresponding double logarithmic curves of the association integral C_r versus the scale r when different embedding dimensions are chosen.



(a) Double logarithmic curves (b) The variation relationship of D_m with m
 Fig.3-9 Correlation dimension Analysis for the X-direction time series of the Lorenz system

In Figure 3-9(a), the correlation integral C_r remains constant at $\ln r > -0.5$ and the double logarithmic curve forms a straight line parallel to the scale axis; $-5 \leq \ln r \leq -2$, as shown in Figure 3-9(a), the red diagonal region is the scale-free interval, and the double logarithmic curve in the interval is a series of approximately parallel tilted straight lines. At this embedding dimension, the value of the slope of the sloping curve obtained by linear fitting with least squares is the correlation dimension. In Figure 3-9(b), the horizontal and vertical coordinates are the embedding dimension and the correlation dimension respectively; when $m < 12$, the correlation dimension increases with the increase of the embedding dimension; and when $m \geq 12$, the correlation dimension becomes stable and reaches the saturation value of 2.1088, so the saturation embedding dimension of D_m is taken as 12. The correlation dimension of this time series is 2.1088, which is consistent with the non-integer dimension and the existence of scale-free interval characteristics, indicating that the signal time series has fractal characteristics. the G-P algorithm can well reflect this characteristic and realize the saturation phenomenon of correlation dimension calculation, so the algorithm is feasible.

3.2 Fractal dimensions of umbilical artery blood signal

3.2.1 Box dimensional analysis of umbilical artery blood signal

1. Data sources and calculations

Clinical Data were collected in Ehu Branch of Xishan People's Hospital, Wuxi, Jiangsu Province, China, using the MDF-OBM umbilical blood detecting device (Fig. 2-15). According to the principle and method of umbilical artery blood signal acquisition, umbilical artery blood signals of 104 pregnant women aged between 22 and 43 years old and between 26 and 40 weeks of gestation were collected from March to July 2020. Umbilical artery blood signal spectrogram and detection parameters were obtained. Figure 3-10 shows the acoustic spectrum of the umbilical artery blood signal in a normal pregnant woman at 30 weeks. Figure 3-11 shows the acoustic spectrum of the umbilical artery blood signal in a abnormal pregnant woman at 32 weeks.

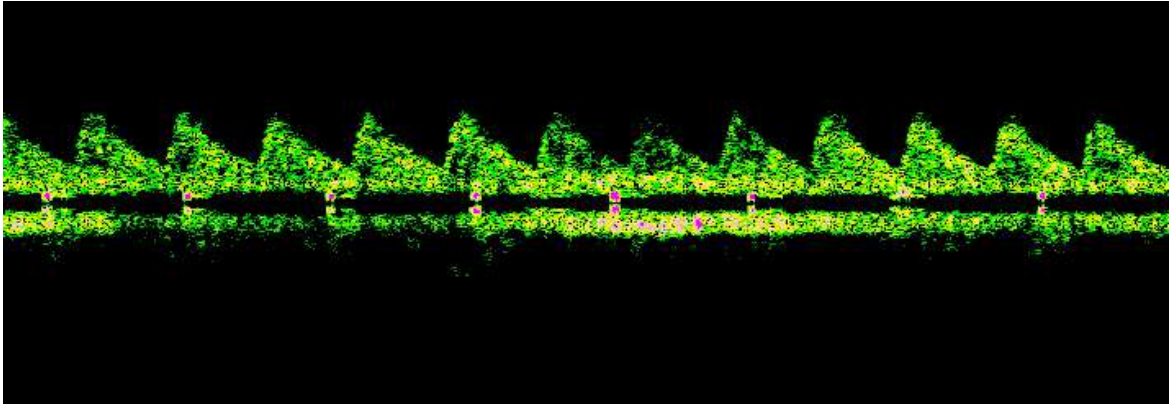


Fig. 3-10 Acoustic spectrum of normal umbilical artery blood with 30 gestational weeks

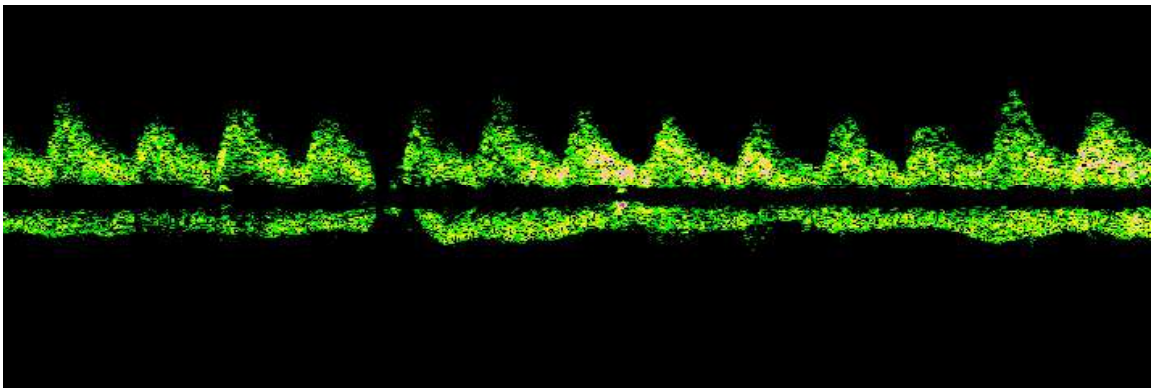
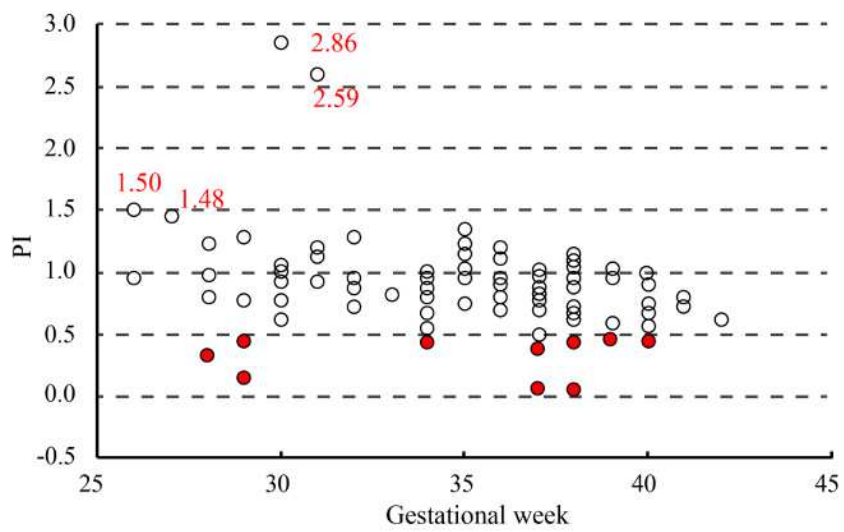


Fig. 3-11 Acoustic spectrum of abnormal umbilical artery blood with 32 gestational weeks

Figure 3-12 displays the results of the analysis and recording of 104 umbilical artery blood S/D value, pulsatile index (PI), and resistance index (RI).



(a) PI results

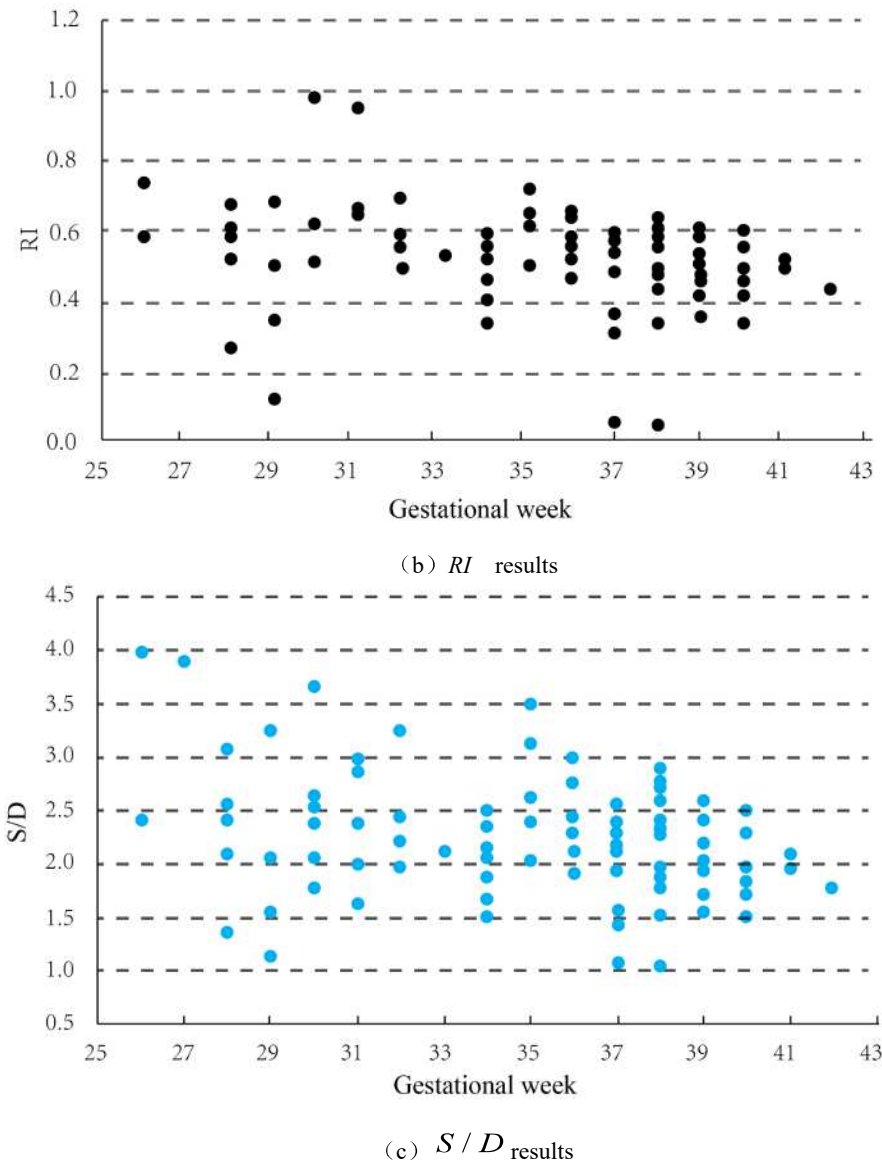


Fig. 3-12 Umbilical artery blood signal indexes of fetus at different gestational weeks

According to Figure 3-12, 104 fetal umbilical artery blood signals were clinically diagnosed and analyzed, and the results were as follows: 61 cases were normal, and 43 cases were abnormal. According to the values, there are 28 exceptions S/D . According to the normal range of pulse index PI , 14 cases had abnormal PI , among which 4 cases had higher PI . Nine patients presented with other clinical symptoms and low PI index. According to the diagnosis of normal RI value range, there were 18 cases of abnormal umbilical artery blood signal, mainly manifested as low umbilical artery flow resistance.

2. Box dimensional calculation and results of umbilical artery blood signal

The box dimension of 104 umbilical artery blood acoustic spectrograms were calculated and analyzed using the box dimension algorithm. Figure 3-13 below shows the results of the box dimension calculation for the acoustic spectrogram of umbilical artery blood signal in 61 normal signals.

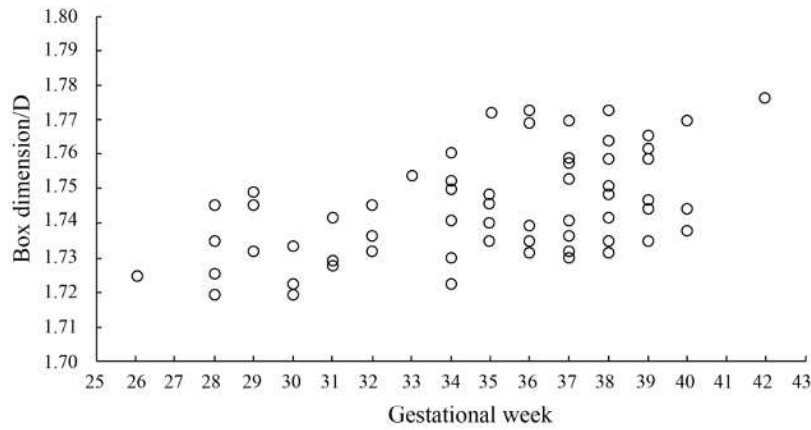


Fig. 3-13 Box dimension of normal umbilical artery blood acoustic spectrogram

The box dimension of umbilical artery blood acoustic spectrograms were calculated and analyzed in 43 abnormal pregnancy group, and the results were shown in Figure 3-14 .

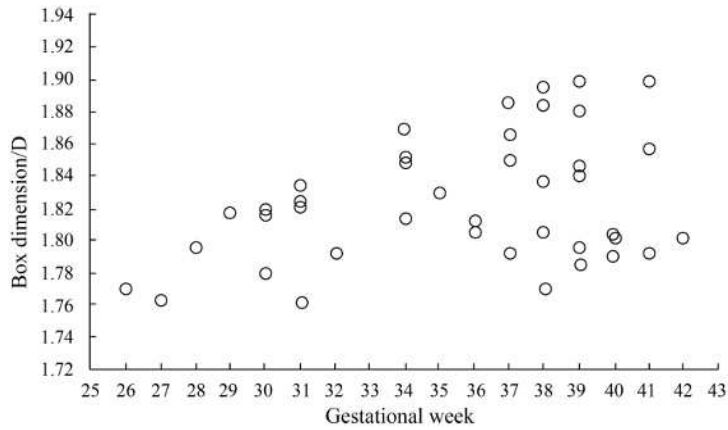


Fig.3-14 Box dimension of abnormal or doubtful umbilical artery blood acoustic spectrogram

According to the Figure 3-13 above, the fractal dimension of acoustic spectrogram of umbilical artery blood in normal group is between 1.718 and 1.776, indicating that gestational week is correlated with box dimension, that is, the box dimension generally increases with the increase of gestational week.

As can be seen from Figure 3-14, the box dimension of acoustic spectrogram of umbilical artery blood in abnormal group ranged from 1.753 to 1.901. It can be obtained that the box dimension of the abnormal umbilical artery blood sonogram is more sensitive than the conventional sonogram parameters by comparing with the clinical diagnostic results. The box dimension of umbilical artery blood acoustic spectrogram increased with gestational week, which was similar to that of normal gestational group.

2. Analysis and conclusions

Figures 3-13 and 3-14 can be compared to observe that, overall, the abnormal group's umbilical artery blood acoustic spectrogram box dimension is larger than that of the normal group. The reasons are as follows:

the fetus blood supply is insufficient or unstable in the abnormal pregnancy group due to pathological defects, which causes the umbilical artery blood signal to fluctuate and result in a larger box dimension. The normal pregnancy group had a more stable umbilical artery blood supply, which consequently led to a more stable umbilical artery blood signal.

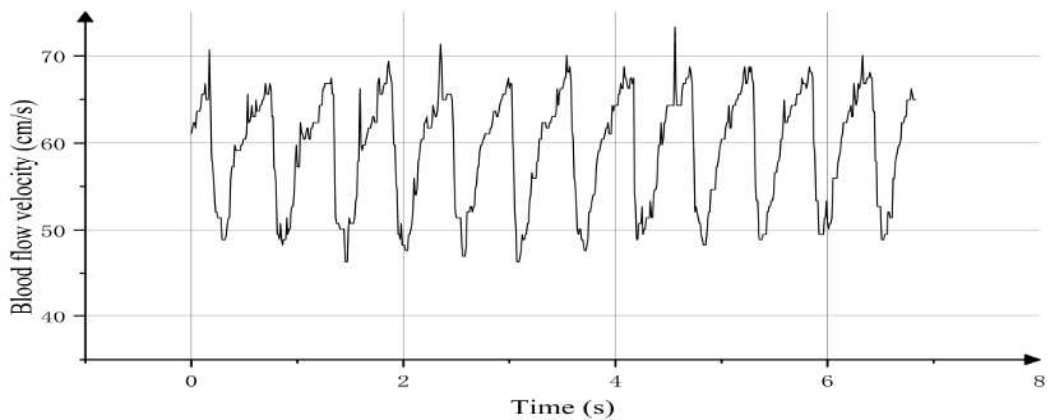
The fractal characteristics of the umbilical artery blood acoustic spectrogram were analyzed and the correlation between the box dimension of the umbilical artery blood acoustic spectrogram and the gestational weeks and the fetal health status were obtained. The main conclusions are as follows:

- (1) Box dimension can be used as an indicator for quantitative detection of fetal health status. The results show that the box dimension increases with the gestational week and therefore there is a positive correlation between the box dimension and the gestational week.
- (2) The box dimension of the umbilical artery blood acoustic spectrogram can reflect the maternal blood supply to the fetus, specifically: the box dimension of abnormal umbilical artery blood signal is higher than that of the normal signal, so the fluctuation of the umbilical artery blood in abnormal pregnant women is more complicated and more intense.

3.2.2 Correlation dimensional analysis of umbilical artery blood signal

1. Data sources

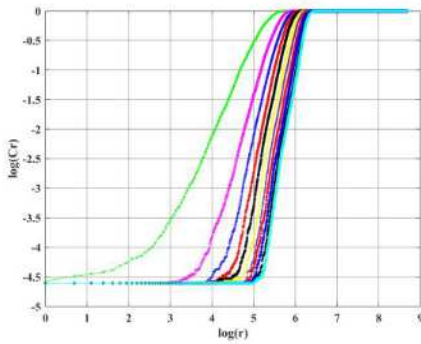
According to the principles and methods of umbilical artery blood signal acquisition, fetal umbilical artery blood signals were acquired from 198 pregnant women aged between 22 and 38 years between Jan and July 2021, and umbilical artery blood sonograms and test parameters were obtained. The signal acquisition method can be found in 2.5.2. From these acoustic spectrograms, 36 normal signals and 36 abnormal signals with good graphical effects were selected and their envelopes were extracted. Thus, the obtained umbilical artery blood time series signal is shown in Figure 3-15.



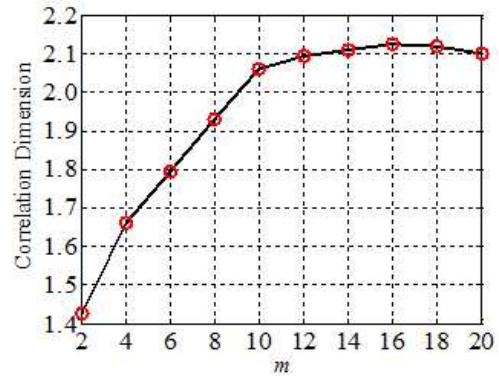
3-15 Umbilical artery blood time series signal

2. Correlation dimension calculation of umbilical artery blood signal

Thirty-six abnormal umbilical artery blood flow signals were selected to form the abnormal group and thirty-six normal umbilical artery blood signals to form the normal group, and the correlation dimension of the two groups was calculated separately. Figure 3-16 shows the double logarithmic curve and the slope of the curve for the correlation dimension of a normal umbilical artery time series signal.



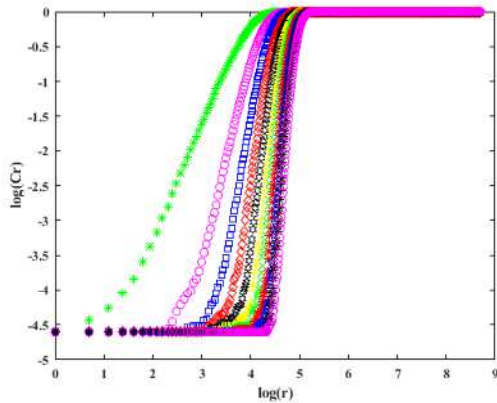
(a) Double logarithmic curves



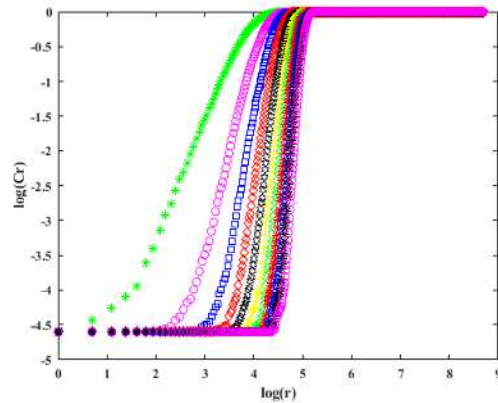
(b) Variation of D_m with m

Fig.3-16 Correlation dimension analysis of a normal umbilical artery signal

Thirty-six umbilical artery blood signal correlation dimensions were calculated for the normal group, and part of the double logarithmic plots were obtained separately as shown in Figures 3-17 below.



(a) Double logarithmic curve No.1



(b) Double logarithmic curve No.2

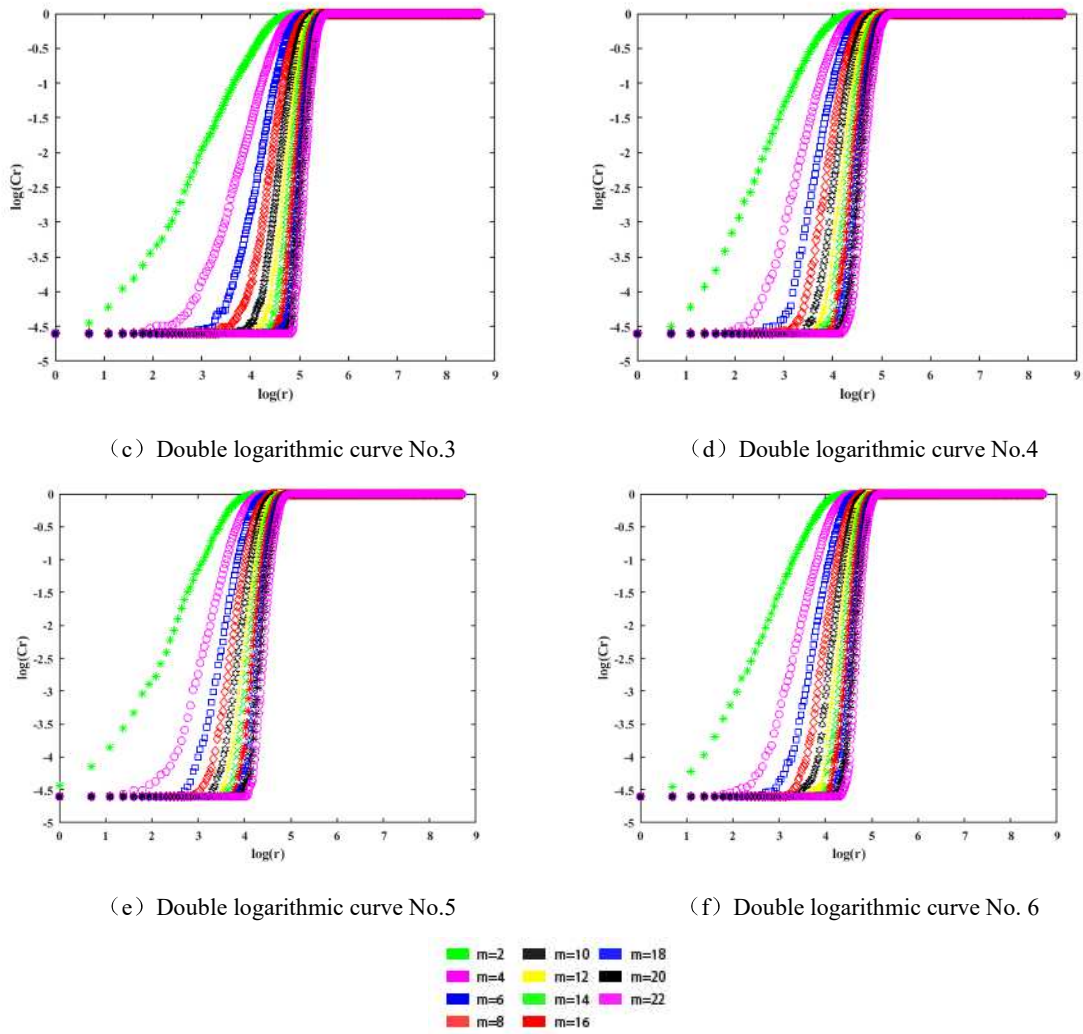


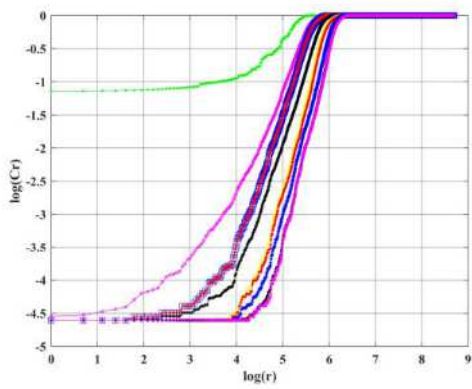
Fig. 3-17 Double logarithmic curve of CD for the normal group of umbilical artery blood signal

The partial corresponding CD are shown in Table 3-3 below.

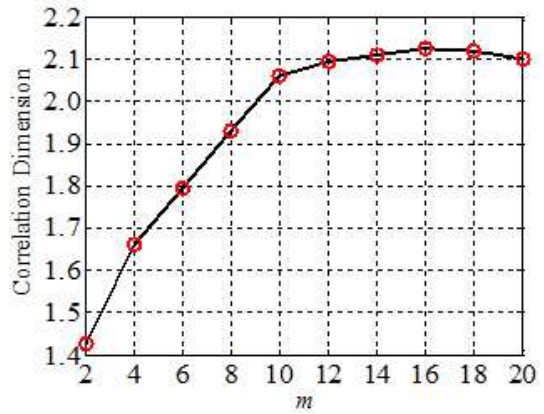
Table 3-3 CD of umbilical artery blood signal for the normal group

| | | | | | | |
|---------------|-----|-----|------|-----|-------|-----|
| Serial number | 1 | 2 | 3 | 4 | 5 | 6 |
| CD | 9.2 | 9.7 | 10.1 | 9.5 | 10. 2 | 8.8 |
| Serial number | 7 | 8 | 9 | 10 | 11 | 12 |
| CD | 9.3 | 9.9 | 8.9 | 9.1 | 10.1 | 9.4 |

Figure 3-18 shows the double logarithmic curve and slope of the curve for the correlation dimension of the time series signal of an abnormal umbilical artery blood.



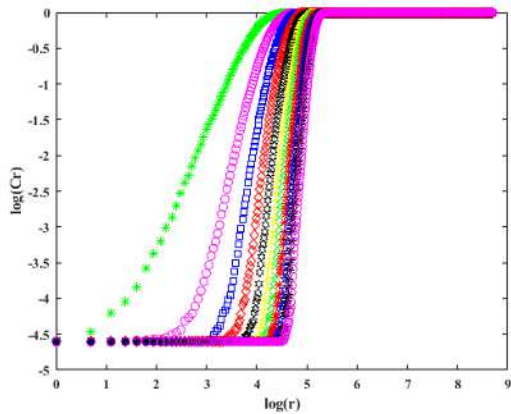
(a) Double logarithmic curve



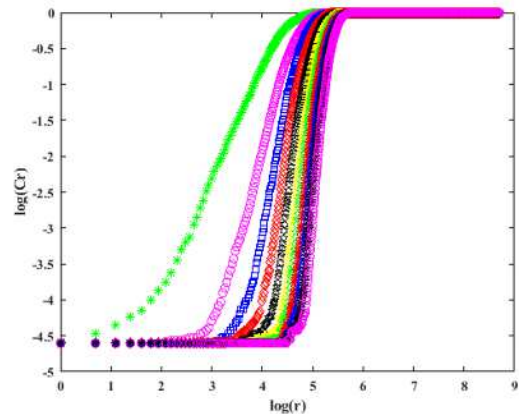
(b) Variation of D_m with m

Fig.3-18 Correlation dimensional analysis of the abnormal umbilical artery blood signal

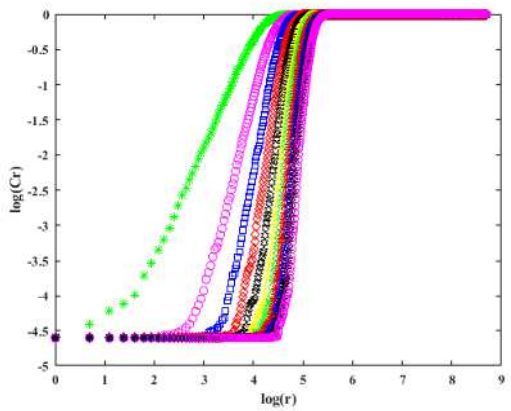
The correlation dimension of the six umbilical artery blood signals in the abnormal group was calculated and a double logarithmic plot was obtained separately as shown in Figure 3-19 below.



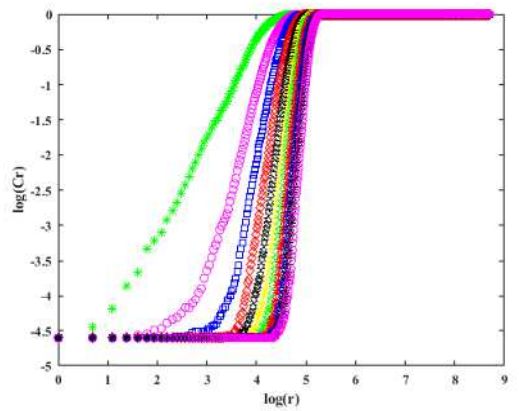
(a) Double logarithmic curve No.7



(b) Double logarithmic curve No.8



(c) Double logarithmic curve No.9



(d) Double logarithmic curve No.10

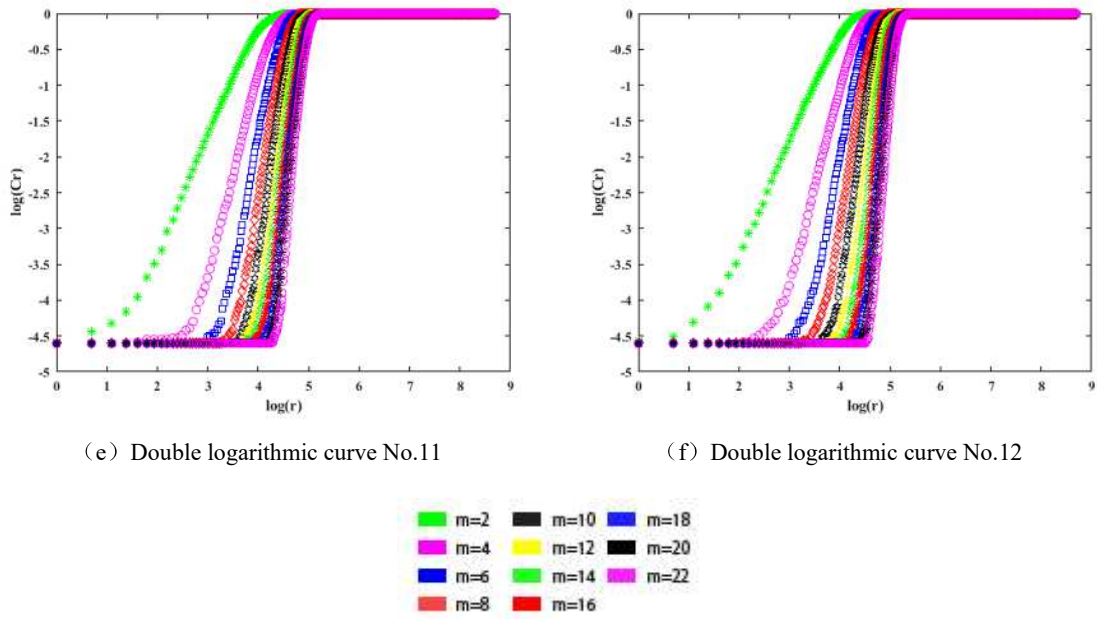


Fig. 3-19 Double logarithmic curve of the correlation dimension of the umbilical artery signal in the abnormal group

The partial corresponding abnormal group CD values are shown in Table 3-4 below.

Table 3-4 CD of umbilical artery blood signal for the abnormal group

| | | | | | | |
|---------------|-----|-----|-----|-----|-----|-----|
| Serial number | 1 | 2 | 3 | 4 | 5 | 6 |
| CD | 8.3 | 8.4 | 8.9 | 8.5 | 7.7 | 8.2 |
| Serial number | 7 | 8 | 9 | 10 | 11 | 12 |
| CD | 9.3 | 8.6 | 9.7 | 8.4 | 7.7 | 7.9 |

The CD of the abnormal umbilical artery blood signal is significantly reduced compared to the normal umbilical artery signal.

The correlation dimension of umbilical artery blood time series signal shows that the embedding dimension m and correlation dimension D_m of abnormal umbilical artery blood signal are significantly reduced, which indicates that there is an obvious nonlinear dynamic difference between abnormal umbilical artery blood signal and normal umbilical artery blood signal, The complexity of time series signals of abnormal umbilical artery blood is higher than that of normal signals.

3. Analysis and conclusions

The box plot and ROC curves of the calculations are shown in Figure 3-20 and Figure 3-21 below.

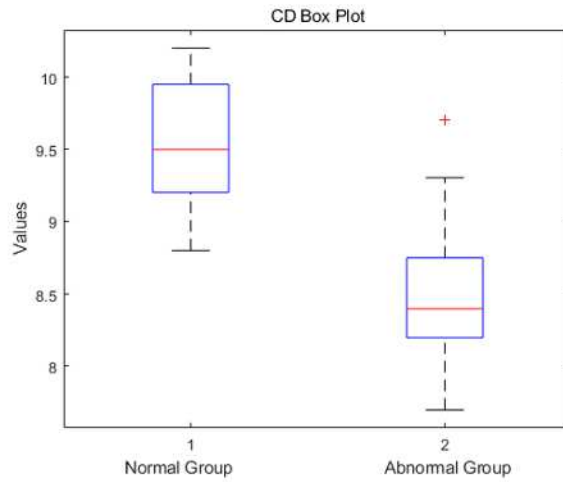


Fig.3-20 Box plot of correlation dimension

In Figure 3-20, it is evident that the median CD values of the normal group and the abnormal group exhibit a significant difference of approximately around ten percent. This observation is of paramount importance as it suggests that CD values may serve as an effective indicator for distinguishing data between the normal and abnormal groups in clinical practice. Furthermore, an in-depth analysis of the box plot reveals additional insights into the performance of CD values in distinguishing between these two data groups. The positions of the 25th and 75th percentile lines indicate the distribution range of CD values and the distribution of data points within this range. This aids in understanding the relative distribution of CD values in the abnormal group as compared to the normal group. However, it is important to note that the maximum CD value in the abnormal group exceeds the 75th percentile line of the normal group, implying a certain degree of overlap. This overlap could potentially lead to some misdiagnoses when using CD for disease diagnosis. Therefore, a more in-depth examination of the performance and accuracy of CD values is necessary to determine optimal thresholds or standards, with the goal of minimizing misdiagnosis.

On the other hand, there are some values in the abnormal group that are close to those of the normal group. This may have a significant impact on the diagnostic results, especially when using CD values for diagnosis. These outliers close to the normal group may interfere with the modelling, making it difficult to accurately predict the state. Therefore, it is necessary to perform screening and elimination operations on these outliers before building the diagnostic model to ensure the robustness and reliability of the model. This step is essential to maintain the accuracy of diagnosis and the effectiveness of treatment decisions.

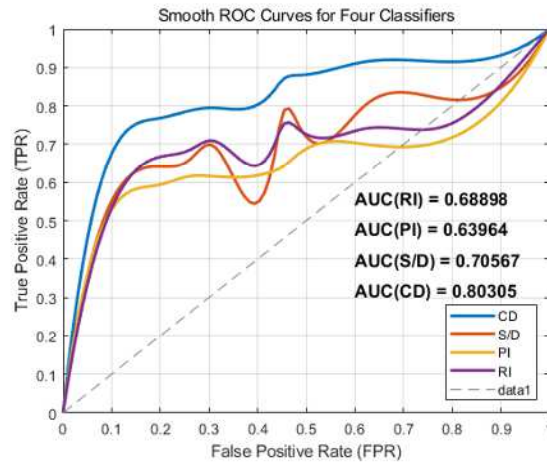


Fig.3-21 ROC of correlation dimension

Through the observation of Figure 3-21, the excellent performance of the CD method in ROC analysis becomes distinctly evident. Specifically, the ROC area under the curve (AUC) for CD reaches 0.80305, a value that significantly surpasses that of other methods, including S/D with an AUC of 0.70567, RI with an AUC of 0.68898, and PI with an AUC of 0.63964. It is worth emphasizing that the CD method exhibits a significantly higher true positive rate (TPR) compared to other methods, underscoring its lower misdiagnosis rates and heightened accuracy in terms of diagnostic performance.

These results clearly highlight the excellent performance of the CD method in the diagnosis of umbilical artery blood, especially when compared with other methods under ROC analysis. This result emphasises the low misdiagnosis rate of the CD method, which is essential to ensure accurate diagnosis and effective therapeutic decisions.

3.3 Signal analysis of umbilical artery blood based on Hurst index

Hurst exponent, as an important indicator of nonlinear characteristic analysis of data signals, is widely used in time series data analysis in the middle of the 20th century [19]. The Hurst exponent can be calculated by R/S method, Whittle method, period graph method and aggregation scale absolute value method. As a non-parametric analysis method, R / S analysis method has been applied to the study of nonlinear systems in many fields [20]. The biggest advantage of this method is that it is not necessary to assume whether the measure of time series is normally distributed or not, and the R/S method can obtain effective and reliable results. R/S analysis method can analyze the fractal characteristics and long-range correlation of time series signals based on Hurst exponent, to distinguish the randomness and non-randomness of the time series [21]. Fetal umbilical artery blood signals do not have random non-linear time series signals. Therefore, Hurst exponent is used to study them to explore the signal characteristics and

predictability of umbilical artery blood, which can provide early theoretical reference for using umbilical artery blood signal time series to carry out fetal early diagnosis, disease monitoring and early treatment.

3.3.1 Hurst Index

Hurst exponent (H) is a statistic between 0 and 1. H values in different ranges represent different meanings. It can be used to measure the long-term correlation and self-similarity of time series. Long range correlation reflects the statistical correlation of two time series data within a period, while self-similarity reflects the similarity of time series fluctuations. For a time series:

(1) $H > 1$ indicates that the time series is an unstable signal; The time series is a random signal similar to Brownian noise when $H=1.5$.

(2) $H \approx 1$ indicates that the process is “ $1/f$ fluctuation”. This time series is highly predictable, and data signals in the future can be predicted based on current data signals when $H \approx 1$.

(3) $1/2 < H < 1$ indicates that the time series has long-term positive correlation, that is, if the fluctuation characteristic of a time series signal increases in a certain interval, the probability of the next interval also shows an increasing trend, and vice versa; When the H value is between $1/2$ and 1 , the larger the H value is, the stronger the long range correlation of time series signal is, and vice versa.

(4) $H \approx 1/2$ indicates that the time series signal has no long-range correlation and is a random process like “white noise”. The time series shows the characteristics of normal distribution, which obey the standard geometric Brownian motion. The variables are completely random and unrelated. The current data signal has no influence on the future data signal, and the predictability is poor.

(5) $0 < H < 1/2$ indicates that time series has long-term negative correlation, that is, if time series shows a downward trend in a certain interval, it is highly likely to show an increasing trend in the next interval, and vice versa.

3.3.2 R/S analysis method

1. CR/S analysis method

H E Hurst proposed CRS analysis method [22], the CRS analysis principle is as follows:

(1) The length of time series $\{P(t)\}$ is N , which is divided into non-overlapping continuous sub-intervals with growth degree of N , $I_a (a = 1, 2, \dots, A)$, where each element is $I_a P_{k,a}, k = 1, 2, \dots, n$.

(2) For each sub-interval, calculate its standard deviation S_I , cumulative mean deviation $\{x_{k,a}\}$ and range R_I respectively.

$$S_I = \sqrt{\frac{1}{n} \sum_{k=1}^n (P_{k,a} - e_a)^2} \quad (3-15)$$

$$x_{k,a} = \sum_{i=1}^k (P_{i,a} - e_a) \quad (3-16)$$

$$R_l = \max_{1 \leq k \leq n} (x_{k,a}) - \min_{1 \leq k \leq n} (x_{k,a}) \quad (3-17)$$

Where: e_a is the mean value of the sequence I_a .

(3) Calculate the rescale range (R_l / S_l) of each sub-interval and the average rescale range $(R/S)_n$ of A interval:

$$\frac{R}{S}(n) = \frac{1}{A} \sum_{a=1}^A (R_l / S_l) \quad (3-18)$$

(4) Change the length n in step (1) and repeat Step (1)-(3) to calculate the range $(R/S)_n$ under different sub-interval lengths n . There is a linear relationship between $(R/S)_n$ and $\lg(R/S)_n$:

$$\lg(R/S)_n = \lg \theta + H \lg n \quad (3-19)$$

(5) The slope H is obtained by linear fitting the sub-interval length and average range drawn on the lg-lg-coordinate graph by the least square method, which is the Hurst exponent.

4. Method of Lo

In 1991, Lo considered that the CRS analysis method will be biased if the time series show strong short-term correlation [23]. Therefore, Lo revised CRS analysis by introducing covariance:

$$\frac{R}{S}(n) = \frac{1}{A} \sum_{a=1}^A \frac{1}{\hat{S}_{a,q}} ([\max_{1 \leq k \leq n} (x_{k,a}) - \min_{1 \leq k \leq n} (x_{k,a})]) = \frac{1}{A} \sum_{a=1}^A \frac{R_l}{\hat{S}_{a,q}} \quad (3-20)$$

$$\begin{aligned} \hat{S}_a^2(q) &= \frac{1}{n} \sum_{k=1}^n (m_{k,a} - \bar{X}_a)^2 + \frac{2}{n} \sum_{j=1}^q \omega_j(q) [\sum_{k=1}^n (m_{k,a} - \bar{X}_a)(m_{k-j,a} - \bar{X}_a)] \\ &= S_a^2 + 2 \sum_{j=1}^q \omega_j(q) \gamma_j \end{aligned} \quad (3-21)$$

In the Equation, $S_a^2 = \frac{1}{n} \sum_{k=1}^n (m_{k,a} - \bar{X}_a)^2$, $\omega_j(q) \equiv 1 - \frac{j}{q+1}$ ($q < n$) is called Bartlett weight, σ_a^2 is the variance of the a -th a ($a = 1, 2, 3 \dots A$) sub sample $\{m_{k,a}\}_{k=1}^n$, and γ_j is the sample autocovariance of order j . $\{m_{k,a}\}_{k=1}^n$. How to select q value directly affects the accuracy of R/S analysis results. Therefore, Lo provides the optimal selection equation of q :

$$q_{opt} = \text{int}[(\frac{3n}{2})^{1/3} (\frac{2\hat{\rho}}{1-\hat{\rho}})^{2/3}] \quad (3-22)$$

$$\frac{R}{S}(n) = \frac{1}{A} \sum_{a=1}^A \left(\frac{1}{A} \frac{Var(S_1^*, \dots, S_a^*)}{\hat{S}_{a,q}^2} \right) \quad (3-23)$$

Where: $\hat{\rho}$ is the estimated value of the first-order auto-correlation function. Lo method is CRS method when $q = 0$. Because the short-term correlation of time series signals is removed, Lo method is better for detecting the long-term correlation of time series.

$$S_k^* = \sum_{j=1}^a (m_{k,j} - \bar{X}_j) \quad (3-24)$$

$$Var(S_1^*, \dots, S_a^*) = \frac{1}{a} \sum_{n=1}^N (S_j^* - \bar{S}_a^*)^2 \quad (3-25)$$

5. V/S method

Some scholars believe that time series with significant long-term correlation cannot be accurately dealt with by Lo analysis method [24]. Therefore, V/S analysis method based on Lo analysis method is proposed:

$$(R/S)_n = \frac{1}{A} \sum_{a=1}^A \left(\frac{1}{A} \frac{Var(S_{k,M_1}, \dots, S_{k,M_a})}{\hat{S}_{a,q}^2} \right) \quad (3-26)$$

3.3.3 A comparative study of R/S classic analysis method

To determine the optimal exponential analysis method of umbilical artery blood signal, the power spectrum Fast Fourier Transform (FFT) method is used to generate the sequence data of Fractional Gaussian Noise (FGN) with known exponent. Three R/S analysis methods were compared to determine the best method to calculate the Hurst exponent of umbilical artery time series in our research.

1.FGN

J.w. Vanness and Mandelbrot put forward the complete long memory model in 1968 [25]. The sequence of fractal Gaussian noise (FGN) is defined as the first-order difference process of fractal Brownian motion with Hurst exponent $B_H(t)$:

$$\{y_t | y_t = B_H(t+1) - B_H(t)\}_{t=0}^{\infty} \quad (3-27)$$

and its self-covariance function of order k is:

$$\gamma_y(k) = \frac{\sigma^2}{2} (|k+1|^{2H} - 2|k|^{2H} + |k-1|^{2H}) \quad (3-28)$$

Where: $k = \dots, -1, 0, 1, \dots$, $\sigma^2 = \text{Var}(y_i)$ is any positive number, and H is the Hurst exponent between 0 and 1.

FGN sequence can be generated by power spectrum FFT: firstly, the density function of Fractional Brownian Motion (FBM) is constructed, and the corresponding FBM sequence is obtained by inverse transformation of the density function. Then the first order difference is adopted for FBM sequence and the Hurst exponent (H) is selected reasonably to realize the simulation of FGN sequence.

Flandrin [26] proved that the time-averaged power spectrum of the H-sssi process is:

$$R_x(F) = \frac{\sigma_H^2}{|F|^{2H+1}} \quad (3-29)$$

In the Equation (3-29), F is the frequency of the H-sssi process, H is the Hurst index, and σ_H^2 is the intensity of the process.

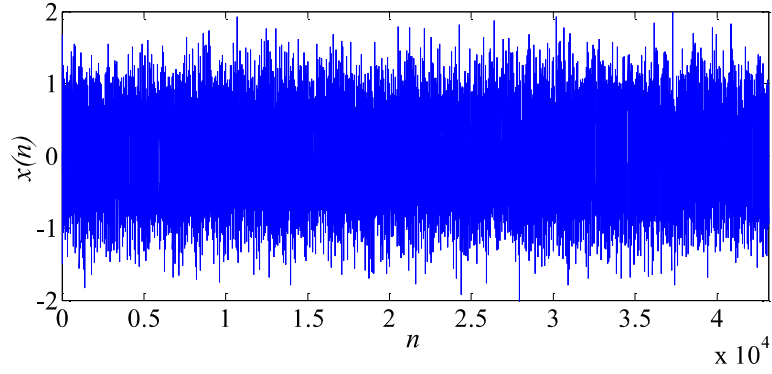
The periodogram belongs to an estimate of the power spectrum [27], defining the periodogram of the data segment $\{x(n)\}_0^{N-1}$ as:

$$\hat{R}_x(e^{j\omega}) = \frac{1}{N} \left| \sum_{n=0}^{N-1} v(n) e^{-j\omega n} \right|^2 = \frac{1}{N} |V(e^{j\omega})|^2 \quad (3-30)$$

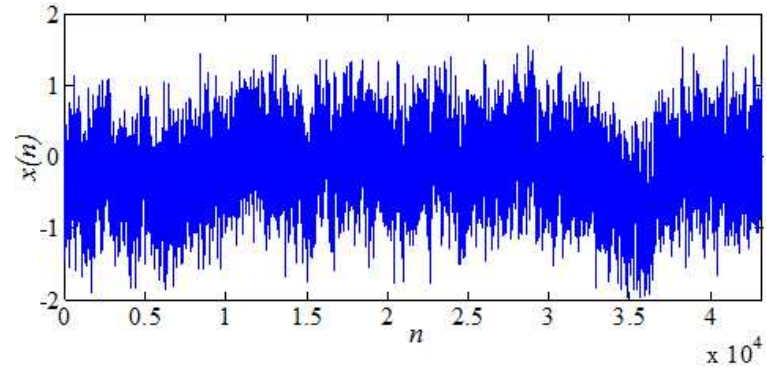
Where: $v(n) = x(n)w(n)$, $w(n)$ indicates a rectangular window and $V(e^{j\omega})$ is the DTFT of the window. Using Equation (3-29) with Equation (3-30) we get:

$$X(e^{j\omega}) = \sqrt{\frac{N\sigma_H^2}{\omega^{2H+1}}} \quad (3-31)$$

The above equation constitutes a sufficient condition for the synthesis of fractal Brownian motion, which allows the establishment of a frequency domain relationship for FBM sampling with Hurst exponent between 0 and 1. The FGN sequence is then obtained by first order differencing of the FBM sequence. Since the length of the 4-second ($f_s = 11025H_z$) umbilical artery time series in this study is 44000, the length of the simulated FGN series is also set to 44000. Figure 3-20 (a) and (b) show the FGN time series for different Hurst indices in the FFT simulation, respectively.



(a) $H=0.6$



(b) $H=0.9$

Fig.3-20 FGN time series under FFT simulation

2. Evaluation results of R/S analysis method based on FGN sequence

In our research, FGN time series with known Hurst exponent is reverse-generated to simulate real umbilical artery blood signals, and the three methods are verified to obtain the best method for analyzing Hurst exponent of umbilical artery blood signals. Five kinds of FGN time series with H values between 0.5 and 0.9 are generated by power spectrum FFT method, and the accuracy of Hurst exponent calculation of three kinds of analytical methods is compared and studied. In our research, the time series length of each umbilical artery signal is 44,000, so FFT simulation is used to generate FGN sequences of the same length. Since FGN sequences are randomly generated, 100 FGN sequences are generated under each specific H value to evaluate the three R/S analysis methods respectively. Then calculate the mean value of Hurst exponent of these 100 FGN sequences, and the calculation formula is as follows:

$$\bar{H} = \frac{1}{100} \sum_{i=1}^{100} \hat{H}_i \quad (3-32)$$

Where: \hat{H}_i is the Hurst estimation value of 100 randomly generated FGN sequences.

The FGN time series with each particular Hurst index were first simulated five times to obtain 100 sets

of FGN series each time, then the series were analyzed for Hurst index using three R/S class analysis methods, and finally the Hurst index was calculated for the 100 sets of FGN series obtained from each run and the mean value was calculated (\bar{H}), the results of which are shown in Figure 3-21.

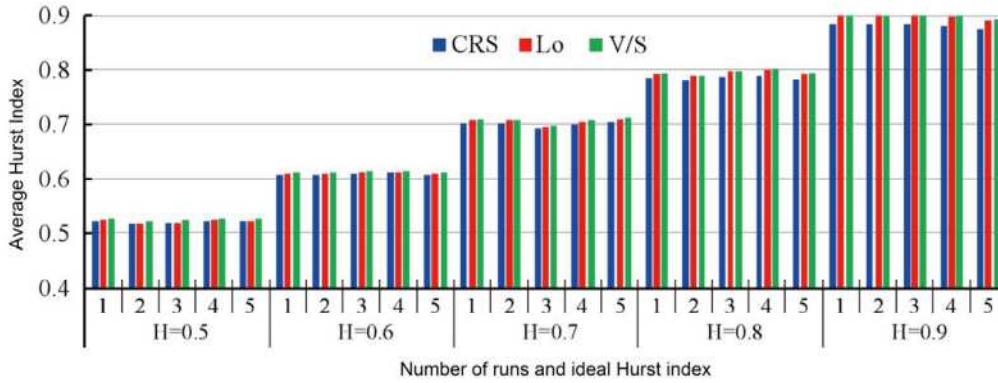


Figure 3-21 Calculated average values of Hurst index for FGN series (\bar{H})

In the above figure, the X coordinate is the number of runs and the ideal Hurst exponent, and the Y coordinate is the average Hurst exponent. The Hurst exponent obtained by three R/S analysis methods is as follows: when $H=0.5$ and $H=0.6$, the average Hurst exponent obtained by the three methods is slightly larger than the true value, but CRS method is the closest to the true value. Lo method and V/S method both have large errors, among which V/S method has the largest error. When $H=0.7$, the Hurst exponent of the three methods are both lower than the true value and greater than the true value, but the calculation results of CRS method are still better and closer to the true value, when $H=0.8$ and $H=0.9$, the Hurst exponent of CRS method are both smaller than the true value and have the largest error, while the calculation results of Lo method and V/S method are close to the true value and there is little difference between the two methods, that is to say: If the Hurst exponent of the time series of umbilical artery blood signal is between 0.5 and 0.7, the CRS method is used to analyze the Hurst exponent. However, if the Hurst exponent of the time series of umbilical artery blood signal is around 0.8~0.9, the Lo method is more accurate. When calculating Hurst exponent of time series of umbilical artery blood signal with length of 44,000, it is found that its value is around 1. Therefore, Lo method is selected in this research.

3.3.4 Hurst exponent analysis of umbilical artery blood signals

Based on the above FGN time series and the verification results of three R/S analysis methods, Lo method is more accurate for Hurst index analysis of 44000-length umbilical artery signal time series. Therefore, Lo method was adopted in this section to study umbilical artery blood signals and goodness-of-fit tests of the calculation process to ensure the accuracy of the calculation results.

As a statistic for linear regression analysis, the goodness of fit (R^2) is an important indicator of the goodness of fit of linear regression [28]. The value of goodness of fit ranges from 0 to 1. The closer the value to 1, the more accurate the calculated Hurst index is, indicating a better fit and the stronger the self-similarity of the umbilical artery blood signal time series. The calculation principle is as follows:

$$R^2 = \frac{\sum (\hat{y}_i - \bar{y})^2}{\sum (y_i - \bar{y})^2} \quad (3-33)$$

Where: $\hat{y}_i = H \cdot \lg(S) + \lg\theta$, y_i is the log rescaled polar deviation for each subinterval $\lg(R_i / S_i)$, H is the Hurst index, \bar{y} is the average log rescaled polar deviation value for all subintervals $\lg(R/S)_n$, $\lg\theta$ is a constant.

The correlation degree of the umbilical artery blood time series was analyzed by the Lo method, and the Hurst index was obtained by calculating a linear fit to the double logarithmic coordinates and testing the goodness of fit over all subinterval lengths. The linear regression of a particular umbilical artery blood time series is shown in Figure 3-22, with a goodness of fit R^2 of 0.9976; slope 1.0992 (Hurst index).

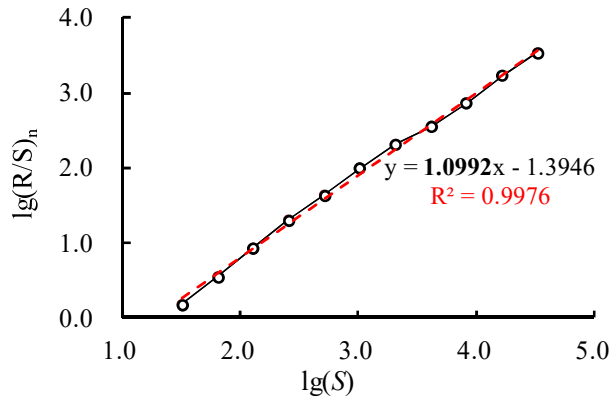


Fig.3-22 Double logarithmic plot of extreme deviation versus subinterval length

According to the Hurst exponent analysis and goodness-of-fit tests mentioned above, Hurst exponent analysis was performed on time series of 12 normal umbilical artery blood, and the results are shown in Figure 3-23.

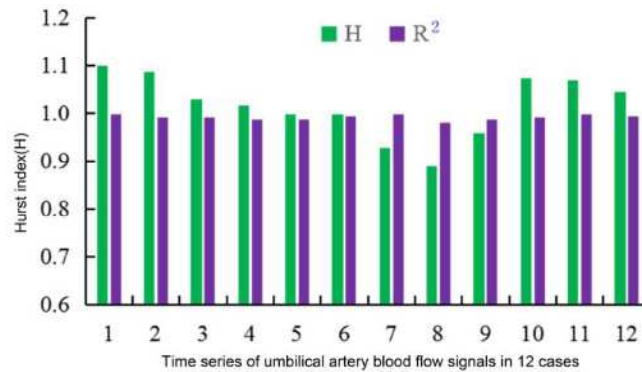


Fig.3-23 R/S analysis and goodness-of-fit test results

In Figure 3-23, the X coordinate is the 12 umbilical artery blood time series, and the Y coordinate is the results of Hurst exponent. It can be seen from Figure 3-23 that the Hurst exponent of time series of umbilical artery blood signal based on Lo method is different from each other, the maximum is 1.0898, the minimum is 0.87919. However, the Hurst index of all the time series of umbilical artery signals is close to 1. The results showed that the time series of signal of umbilical artery blood showed a long-range positive correlation and was consistent with the characteristics of “ $1/f$ fluctuation”. In addition, goodness-of-fit test was carried out for 12 umbilical artery blood samples. If the fitting results of Hurst exponent calculation process were better, the value of R^2 is between 0.990 and 0.999. It indicates that the time series of umbilical artery signal has obvious self-similarity.

3.4 Summary

In this chapter, the basic concepts of fractal and fractal dimension are explained, the self-similarity and scale-invariance of fractal are described, and the algorithms for counting box dimension and correlation dimension are introduced in detail.

The box dimension of the umbilical artery blood signals and detection data of 104 pregnant women are calculated, and the fractal and nonlinear characteristics of those signals are analyzed. The results indicate that there is a positive correlation between the box dimension of umbilical artery blood signals and gestational weeks. Secondly, thirty-six time series signals of abnormal umbilical artery blood and 36 time series signals of normal umbilical artery blood are composed into the abnormal group and the normal group. The CD of abnormal umbilical artery blood signal decreased significantly. CD is significantly superior to conventional parameters in distinguishing the normality of umbilical artery blood signals. The results show that the time series signals of umbilical artery belonged to non-stationary signal and show obvious “ $1/f$ fluctuation” characteristic.

3.5 References

- [1] Lv J H, Lu J A, Chen S H. Chaotic time series analysis and its applications [M]. Wuhan: Wuhan University Press, 2002.
- [2] Mandelbrot B B. “How Long Is the Coast of Britain?”[J]. Science, 1967,156 (3775): 636–638.
- [3] Mandelbrot B B. Stochastic models for the Earth's relief, the shape and the fractal dimension of the coastlines, and the number-area rule for islands[J]. Proceedings of the National Academy of Sciences, 1975,72(10): 3825-3828.
- [4] Mandelbrot B B. Fractals: form, chance and dimension[M]. San Francisco: W. H. Freeman, 1977.
- [5] Mandelbrot B B. The Fractal Geometry of Nature [M]. New York: W.H. Freeman, 1983.
- [6] Falconer K J, Zeng W Z. Fractal geometry: mathematical foundations and their applications[M]. People's Post and Telecommunications Publishing House, 2007.
- [7] Mandelbrot B B, Wheeler J A. The Fractal Geometry of Nature[J]. Journal of the Royal Statistical Society, 1982,147(4): 468-476.
- [8] Manabu Tanaka, Atsushi Kayama, Ryuichi katu, et al. Estimation of the fractal dimension of fracture surface patterns by box-counting method[J]. Fractals-complex Geometry Patterns & Scaling in Nature & Society, 2011,7(7): 335-340.
- [9] Hao, B L. Chaos and fractals [M]. Shanghai: Shanghai Science and Technology Press, 2015.
- [10] Zhao J, Lei L, Pu S Q. Fractal theory and its applications in signal processing [M]. Beijing: Tsinghua University Press, 2008.
- [11] Falconer K J. Fractal Geometry: Mathematical Foundations and Applications[M]. Wiley, 2003.
- [12] Jin, N D. Nonlinear information processing techniques [M]. Tianjin: Tianjin University Press, 2017.
- [13] Yuan Q Y, Li C H, Yang Y, et al. Comparative study of turbulent wind spectrum properties based on fractal science[J]. Thermal Power Engineering, 2017(5): 118-124.
- [14] Zhang Y Z, Ji H G, Xiang P, et al. Analysis of impact ground pressure precursors based on the temporal fractal characteristics of mine borehole strain observation data[J]. Journal of Rock Mechanics and Engineering, 2016,35(S1): 3222-3231.
- [15] Patil P S. IRIS Classification based on Fractal Dimension Box Counting Method[J]. International Journal of Computer Applications, 2015, 112(11): 21-27.
- [16] Packard N H, Crutchfield J P, Farmer R S. Geometry from a Time Series[J]. Physical Review Letters, 1980,45: 712.
- [17] Grassberger P, Procaccia I. Estimation of the Kolmogorov entropy from a chaotic signal[J]. Physical Review A, 1983,28(4): 2591-2593.
- [18] Dong C J, Shao C F, Zhang H, et al. Phase space reconstruction of expressway traffic flow parameters based on G-P algorithm[J]. Journal of Jilin University (Engineering Edition), 2012,42(3): 594-599.
- [19] Shu Y T, YANG O, Zhang H F. Estimation of Hurst parameter by variance-time plots, Proceedings of

- the IEEE Pacrim, 1997, 2: 883-886.
- [20] Zhao Y N. ECG pathological signal analysis based on MF-DFA and Hurst index, doctoral diss., Nanjing University of Posts and telecommunications, Nanjing, 2011.
- [21] G. Poveda, O. J. Mesa. Estimation of the Hurst Exponent h and Geos Diagrams for a Non-Stationary Stochastic Process[M]. Netherlands: Springer, 1994.
- [22] Hurst H. E. The problem of long-term storage in reservoirs[J]. International Association of Scientific Hydrology Bulletin, 1956, 1(3):13-27.
- [23] Lo A W. Long-Term Memory in Stock Market Prices[J]. Econometrica, 1991,59(5): 1279-1313.
- [24] Giraitis L, Kokoszka P, Leipus R, et al. Rescaled variance and related tests for long memory in volatility and levels[J]. CORE Discussion Papers RP, 2003,112(2): 265-294.
- [25] Mandelbrot B B, Ness J W V. Fractional Brownian Motions, Fractional Noises and Applications[J]. Siam Review, 1968,10(4): 422-437.
- [26] Flandrin P. On the spectrum of fractional Brownian motions[J]. IEEE Transactions On Information Theory, 1989,35(1): 197-199.
- [27] Figueiredo R J P D. The Volterra and Wiener theories of nonlinear systems[J]. Proceedings of the IEEE, 1982, 70(3): 316-317.
- [28] Zhao S S. Influencing factors and evaluation of adaptation to R^2 superiority[J]. Journal of Northeast University of Finance and Economics, 2003,16(3): 56-58.

Chapter 4

Chaotic characterization of umbilical artery blood signal

4.1 Chaos theory

Systems in which the equations of time evolution are non-linear are defined as non-linear systems, i.e. systems in which the dynamic variables describing the properties of the system (i.e. position, velocity, acceleration and pressure etc.) appear in the equations in a nonlinear form are non-linear systems. In various fields of research, non-linear systems are more appropriately referred to as non-linear dynamics, i.e. the study of the dynamical behavior of non-linear systems.

Chaos is a complex and irregular behavior arising from nonlinear systems prevalent in nature. In deterministic systems, chaos is both seemingly random and similarly irregular [1], a new form of existence in nonlinear systems [2]. Chaotic systems are predictable in the short term but unpredictable in the long term and are an important tool for quantitative analysis of nonlinear systems [3].

At present, the application of chaos theory in biomedicine is still in its infancy compared to other fields, and although the scope of its application is still relatively narrow, it has expanded new ideas and provided new ways for the analysis of biomedical signals.

4.1.1 Origin and development of Chaos

Dynamics is considered as an important conceptual scheme between mathematics and other sciences, and under a common geometric model, dynamics unifies physical, biological, and social sciences, and mathematics, applied sciences and experimental sciences are the three branches of disciplines developed by dynamics. In 1903, Poincaré [4] combined the study of topology with dynamical systems to formulate the Poincaré conjecture, which dominated the field of dynamical systems research. A dynamical system is defined as anything that moves, changes, or evolves over time. A dynamical system is considered “deterministic” if each state has a specific outcome, and “non-deterministic” if multiple outcomes can be chosen from a probability distribution.

In the 19th century, a few classical physicists and mathematicians considered dynamical systems. In 1898, Hadamard [5] first observed previously proposed solutions to initial condition sensitivity in a special system known as geodesic flow. Poincaré [6] initially highlighted the sensitivity to initial conditions and the unpredictability of the philosophical aspect of science in 1908. In 1954 Kolmogorov [7] published “The preservation of conditional periodic motion in the Hamilton function at small changes” which established that conservative and dissipative systems are both chaotic, giving rise to the prototype of the KAM theorem.

In 1963, Lorenz [8] rediscovered “chaos” and he derived in an equation in dissipative systems. In 1964, the French astronomer Héno [9] discovered the Hénon map, which led to the theory of thermal gravitational collapse. With the development of mathematics, in 1971, the French mathematician and physicist Ruelle and the Dutch scholar Takens [10] were the first to propose a new argument for describing the mechanism of turbulence formation in terms of chaos, finding that dynamical systems have singular attractors, such as limit cycles leading to periodic solutions, and ring surfaces leading to quasi-periodic solutions, a study that stimulated the interest of researchers in different fields in chaos. Since 1975, chaos-related publications have developed very rapidly, with Hao Berlin [11] compiling several reference papers on chaos into one reference. Campbell [12] and Marek and Schreiber [13] having extensive reviews of chaos theory in their literature. In 1975, the Chinese-American scholar Li Tianyan and the mathematician Yorke [14] proposed the Li- Yorke’s theorem related to chaos. 1976, a comprehensive analysis of the dynamical response of the logistic equations by American mathematical ecologists led to a joint study of chaos in various fields [15]. The first international chaos symposium held in Italy in 1977 further laid the foundation for chaos research [16]. The Feigenbaum number discovered by Feigenbaum in 1978 implies the emergence of a universal theory of one-dimensional mapping chaos phenomena [17].

In the early 1980s, Farne, Packard and Takens et al. proposed a delayed method for the calculation of phase space reconfigurations by dynamical orbits; Grassberger and Procaccia calculated the statistical characteristics of singular attractors based on experimental systems, thus evolving chaos analysis from the theoretical to the practical application stage. Since the mid-1990s, chaos science has permeated other sciences. Chaos theory and nonlinear dynamical theory have been used in a wide range of fields, including turbulence research in physics [18], epileptic brain research in biology [19], epidemiological mechanisms of disease occurrence [20], simulated economic dynamics [21], ocean water level predictability in geology [22], and halo laser research in communications [23].

Researchers in the biomedical community disagree on the application of chaos, with Glass et al. [24] arguing that physiological rhythms in healthy bodies are regular and that chaotic phenomena cannot represent regular disease, while Goldberger et al. [25] argue that physiological rhythms in normal bodies are chaotic and that a disease state is a lack of variability in physiological rhythms.

The linear and non-linear behavior of biomedical signals reflects the normality of human physiological parameters. In recent years, the study of nonlinear characteristics of biomedical signal time series has attracted great interest from a wide range of scholars [26-27]. Chaos is widely used in research areas such as the identification and parameter extraction of ECG signals, heart sound signals and breath sounds, EEG signals, biofeedback systems, EMG signals, neonatal respiratory dynamics, and cellular metabolism [28].

4.1.2 Basic concept of Chaos

It is possible to trace the origin of the concept of chaos in physics to a related work written by L. Boltzmann in the 19th century. Chaos is currently characterized by the following characteristics, even though there is no clear definition of it [29]: ① initial condition sensitivity; ② chaotic attractor property; ③ dimensional property; ④ long-term unpredictability; ⑤ positive Lyapunov exponent; ⑥ ergodicity and boundedness; ⑦ power spectral density property; and ⑧ bifurcation property.

Tianyan Li and Yorke jointly proposed the LI-Yorke theorem [30].

Definition 4-1: Let $f : M \rightarrow M$ be a continuous self-map on the closed interval M if the following requirements are met.

- (1) No upper bound on the period of the f cycle point.
- (2) There exist uncountable sets S on M , S containing no periodic points and satisfying:
 - 1) Same as $\forall x, y \in S, x \neq y$, with $\limsup_{n \rightarrow \infty} |f^n(x) - f^n(y)| > 0$.
 - 2) $\forall x, y \in S, x = y$, with $\limsup_{n \rightarrow \infty} |f^n(x) - f^n(y)| = 0$.
 - 3) $\forall x \in S$ and the cycle point $y \in M$ with $\limsup_{n \rightarrow \infty} |f^n(x) - f^n(y)| > 0$.

In the above equations, $f^n(\bullet)$ denotes the n iteration of the function f , then $f : M \rightarrow M$ is said to be chaotic on S .

Devaney's definition of chaos from a topological perspective in 1989 is as follows:

Definition 4-2 A map $N : X \rightarrow X$ over a bounded closed domain X is chaotic if the following requirements are met.

- (1) It is initial value sensitive and there exists $\delta > 0$ such that for any $x \in X$ and any neighborhood B of x , there exists $y \in B$ and a natural number k satisfying: $|N^k(x) - N^k(y)| > \delta$.
- (2) It is topologically transmitted, i.e. for any two open sets $L, M \in X$, there exists a natural number k such that $N^k(L) \cap M \neq \emptyset$.
- (3) It has dense periodic orbits in X .

4.2 Phase space reconstruction

A phase space is the set of every state of a dynamical system, which is a vector space with embedded dimensions. An important marker of the transition from theoretical to applied chaos science is the development of phase space reconstruction theory, which focuses on the characterization of various "singular attractors", in other words, the study of the chaotic properties of nonlinear dynamical systems by obtaining the structure of their attractors. The theory of phase space reconstruction makes it possible to obtain indirectly the

approximate trajectories of the attractors of evolving systems.

4.2.1 Takens' theorem and reconstructed phase space

The recovery of attractors in higher dimensions is the aim of phase space reconstruction. Although all chaotic attractors are singular, not all singular attractors are chaotic. In other words, the chaos condition is necessary non-sufficient for the singularity condition of attractors. Attractors eventually fall into specified trajectories in chaotic systems as they change in time. The basic idea of reconstructing phase space is that the evolution of a component of a dynamical system is influenced by other components that are interconnected with it [31]. The relevant components can be characterized by a single component, and this single variable leads to a new multidimensional phase space, which contains many of the properties of the original phase space. Therefore, the state of the system trajectory in the 3D phase space can be used as a theoretical basis for qualitatively determining the characteristics of Chaos [32].

The delay coordinate approach is the most used phase space reconstruction technique in the study of nonlinear time series Chaos [33]. In 1981, Takens [34] proved that a reasonable choice of delay time and embedding dimension can reconstruct the regular trajectory of the time series in the phase space, i.e.: embedding the m -dimensional metric space [35] and constructing the phase space structure of the original system based on the one-dimensional time series [36]. Let the nonlinear time series be $X = x_1, x_2, \dots, x_n$, embedding this series into the m -dimensional space and reconstructing the phase space to obtain a sequence of phase points R^m as:

$$R^m = \begin{bmatrix} X_1 \\ X_2 \\ \vdots \\ X_N \end{bmatrix} = \begin{bmatrix} x_1 & x_{1+\tau} & \dots & x_{1+(m-1)\tau} \\ x_2 & x_{2+\tau} & \dots & x_{2+(m-1)\tau} \\ \vdots & \vdots & \ddots & \vdots \\ x_N & x_{N+\tau} & \dots & x_{N+(m-1)\tau} \end{bmatrix} \quad (4-1)$$

Where, τ is the delay time, m is the embedding dimension ($m \geq 2d + 1$ and the dimension of original dynamic system is d), and $N = n - (m - 1)$ indicates that the n phase points become N phase points when the m dimension time series is reconstructed from the time series.

4.2.2 Determination of phase space reconstruction parameters

The morphological characteristics of chaotic attractors in phase space reconstruction are influenced by the delay time τ and the embedding dimension m . Among them, the delay time τ is selected by C-C algorithm, autocorrelation function method and average mutual information method [37], while the autocorrelation function method is simple to calculate but prone to error, which is not suitable for nonlinear

time series. The average mutual information method is cumbersome to calculate and less applied [38]. In this paper, a correlation-integration-based C-C algorithm is used to reconstruct the phase space of the umbilical artery flow Doppler signal time series, which can calculate the embedding dimension and delay time simultaneously, and is easy to operate, computationally compact and noise-resistant.

The C-C algorithm [39] constitutes a statistic through the correlation integral of a time series with delay times τ and time windows τ_m satisfying $\tau_m = (m-1)\tau$, which can be obtained from the relationship between the correlation integral and the delay times to determine the embedding dimension m . The correlation integral is defined as:

$$C(m, r, \tau) = \frac{2}{M(M-1)} \sum_{1 \leq i < j \leq M} H(r - d_{ij}) \quad (4-2)$$

where: r is the neighborhood radius; M is the number of phase points; $d_{ij} = \|X_i - X_j\|$ is the hypersphere radius in phase space and $H(\theta)$ is the Heaviside step function, defined as:

$$H(\theta) = \begin{cases} 1 & (\theta > 0) \\ 0 & (\theta < 0) \end{cases} \quad (4-3)$$

Dividing the umbilical artery blood signal time series $\{x(t), t = 1, 2, \dots, N\}$ into t non-overlapping subseries, get:

$$S(m, N, r, t) = \frac{1}{t} \sum_{s=1}^t [C_s(m, N/t, r, t) - C_s^m(1, N/t, r, t)] \quad (4-4)$$

Take the mean value of all $S(m, N, r, t)$.

$$\bar{S} = \frac{1}{M \cdot J} \sum_{m=1}^M \sum_{j=1}^J S(m, r_j, t) \quad (4-5)$$

where: M, J are the embedding dimension and the number of r , respectively. Defining $\Delta S(m, t)$ as the maximum deviation from the value of r , then:

$$\Delta S(m, t) = \max \{S(m, r_j, t)\} - \min \{S(m, r_j, t)\} \quad (4-6)$$

where: $m = 2, 3, 4, 5, r_i = i\sigma/2, i = 1, 2, 3, 4, \sigma$ is the standard deviation of the time series [40]. The following three variables are calculated separately:

$$\bar{S}(t) = \frac{1}{16} \sum_{m=2}^5 \sum_{j=1}^4 S(m, r_j, t) \quad (4-7)$$

$$\Delta \bar{S}(t) = \frac{1}{4} \sum_{m=2}^5 \Delta S(m, t) \quad (4-8)$$

$$S_{\text{cor}}(t) = \Delta \bar{S}(t) - |\bar{S}(t)| \quad (4-9)$$

From the above three equations, the optimal delay time τ is the time corresponding to the first zero of $\bar{S}(t)$ in Equation (4-7) or the time corresponding to the first local minima of $\Delta \bar{S}(t)$ in Equation (4-8); the time corresponding to the minimum of $S_{\text{cor}}(t)$ in equation (4-9) is the time window τ_m and the embedding dimension $m = \tau_m / \tau + 1$.

4.3 Chaotic characteristic recognition of umbilical artery blood signal

Umbilical artery blood signal time series chaotic characteristics recognition methods can be divided into qualitative and quantitative recognition. The qualitative method of identifying chaos can be distinguished from other signals, such as random, periodic, and quasi-periodic signals, by revealing the special spatial structure of the time series in the time or frequency domain. The quantitative identification method identifies chaotic behavior by calculating the characteristic values of the singular attractors of the time series. The main parameters for characterizing the singular attractors are the proximity orbit dispersion, which characterizes the dispersion rate of the proximity orbit, and the Kolmogorov entropy, which reflects the complexity of the information [41]. In the following, both qualitative and quantitative chaotic characteristics of the umbilical artery blood flow signal will be identified using the phase diagram method and the Maximum Lyapunov Exponent (MLE) index method.

4.3.1 Phase diagram method

For nonlinear systems, the time series phase diagram can be described as the trend of state change over time and reflects the spatial structure of the system's attractors. If the motion of the trajectory in the phase space of the system shows repeated folding, extension and non-periodic motion that never intersects in a finite space, the system can be qualitatively determined as chaotic with singular attractors and has chaotic characteristics [42-43]. The phase diagram method can be used to qualitatively determine the chaotic of the umbilical artery blood signal based on the specificity of the time series in space. To visualize the attractor morphology and structure, the phase diagram method usually determines the optimal delay time for phase space reconstruction and then reconstructs the time series into a three-dimensional phase space to observe the attractor characteristics. The time series with chaotic characteristics are transformed into points in the

three-dimensional phase space, which will form a certain regular trajectory and form singular attractors, while the random time series transformed into points in the three-dimensional phase space are only scattered throughout the phase space without any regularity and will not form a specific trajectory, i.e., no attractors will be formed.

The phase diagram method was used to qualitatively identify chaotic features in the normal umbilical artery blood time series signals collected in 2021. One umbilical artery blood signal from the normal group was taken. Firstly, the C-C algorithm was used to calculate the delay time of each umbilical artery blood signal time series, as shown in Figure 4-1, which shows the variation curve of each statistic of the C-C algorithm for a fetal umbilical artery blood signal time series. As can be seen from the graph, the first local minima of the correlation integral $\Delta\bar{S}(t)$ occurs at $\tau = 48ms$ and therefore the best delay time is taken $\tau = 48ms$.

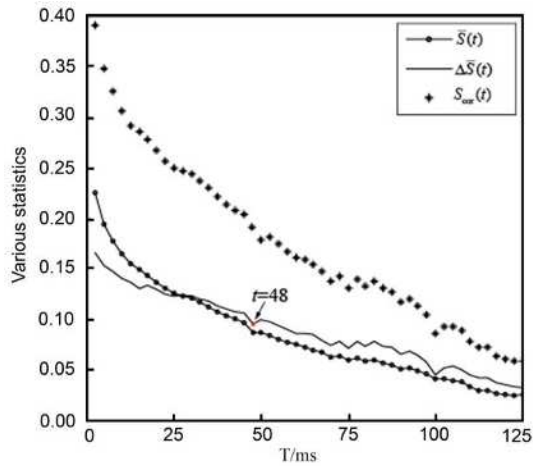
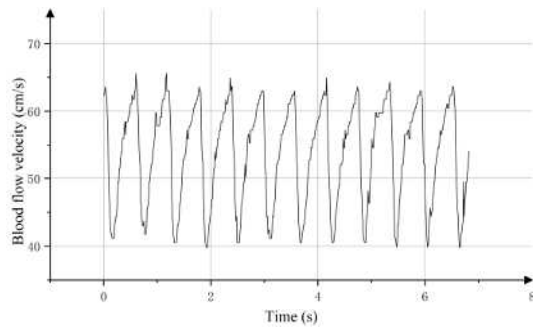
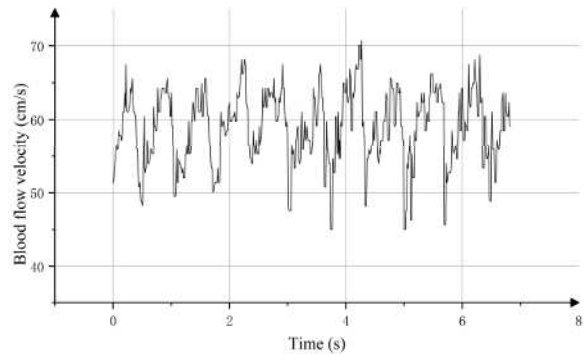


Figure 4-1 Time series C-C algorithm plot of umbilical artery blood signal

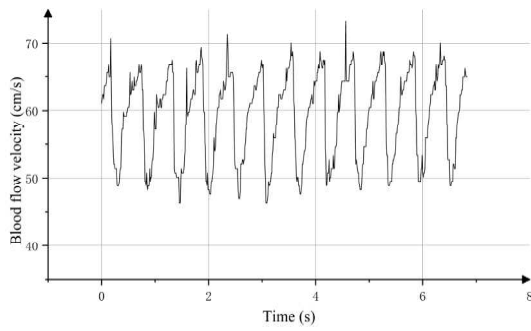
In my research, thirty-six normal umbilical artery blood signals were selected, and 36 abnormal umbilical artery blood signals were selected. Figure 4-2 shows part of normal umbilical artery blood signals, while Figure 4-3 shows part of abnormal umbilical artery blood signals.



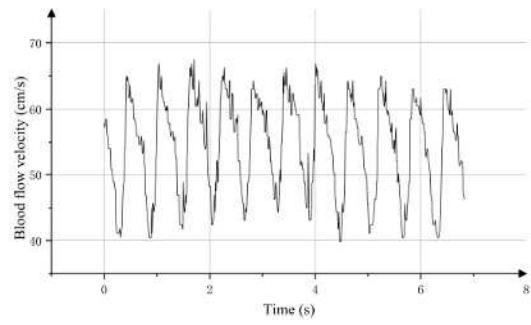
(a) Normal sample No. 1



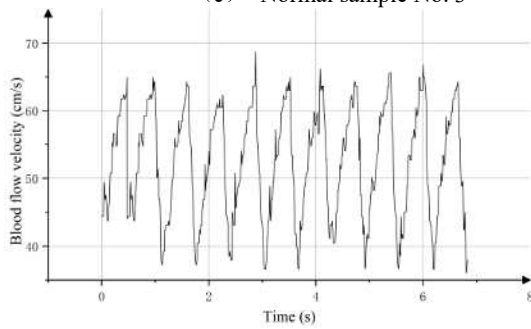
(b) Normal sample No. 2



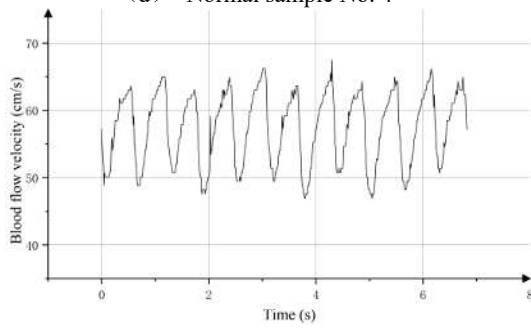
(c) Normal sample No. 3



(d) Normal sample No. 4

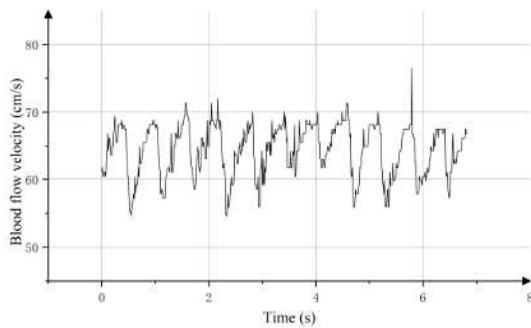


(e) Normal sample No. 5

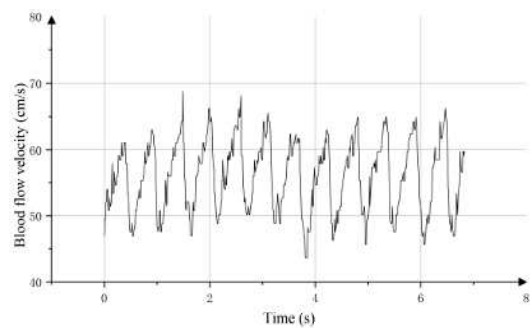


(f) Normal sample No. 6

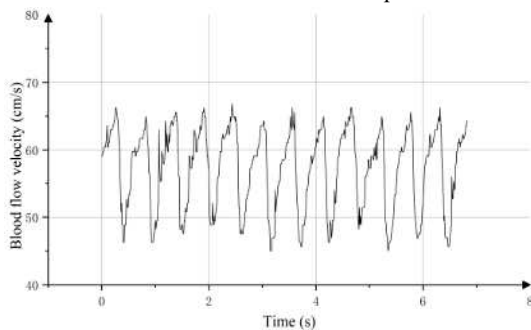
Figure 4-2 The time series of umbilical artery signals in the normal group



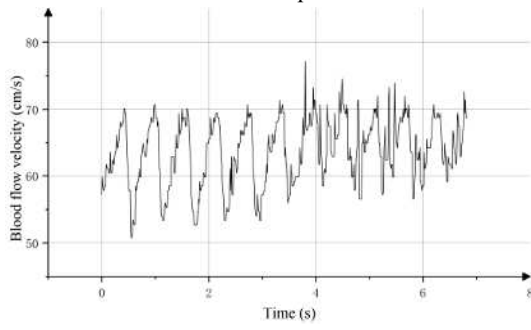
(a) Normal sample No. 7



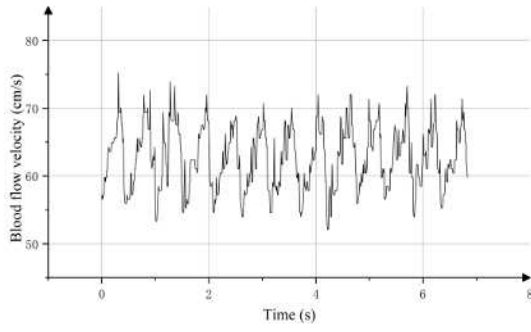
(b) Normal sample No. 8



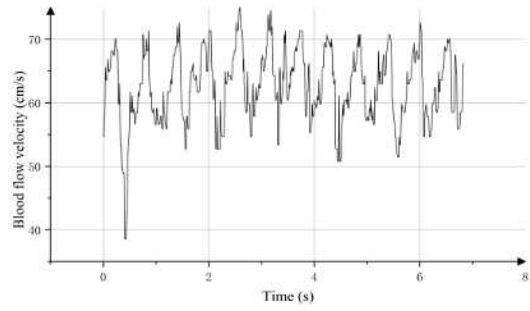
(c) Normal sample No. 9



(d) Normal sample No. 10



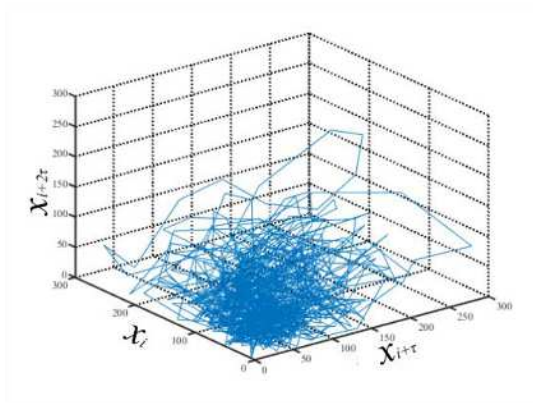
(e) Normal sample No.11



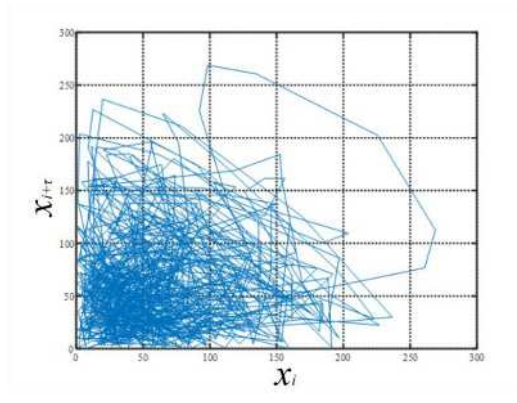
(f) Normal sample No. 12

Figure 4-3 The time series of umbilical artery signals in the abnormal group

Using $\tau=48s$ as the optimal delay time for phase space reconstruction, the umbilical artery blood signal time series was embedded into the three-dimensional phase space, and its phase diagram is shown in Figure 4-4, where Figure (a) is the three-dimensional phase diagram and Figure (b) is the two-dimensional phase diagram.



(a) Three-dimensional phase diagram

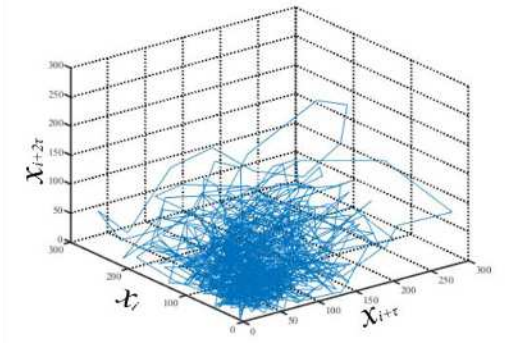


(b) x-y two-dimensional phase diagram

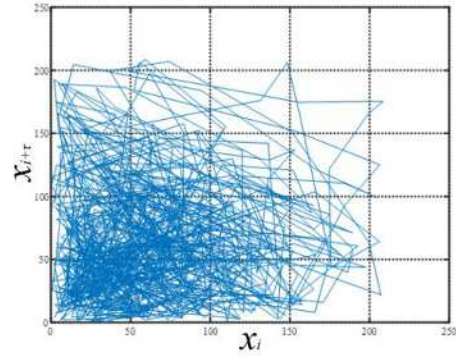
Fig. 4-4 Time series phase diagram of umbilical artery blood signal of normal sample No.1

From the phase diagram, the time series are locally folded and repeatedly entangled in space to form singular attractors, and their phase trajectories are neither reciprocal nor random motion of periodic functions, which can determine that the umbilical artery blood signal time series have chaotic characteristics. The phase space reconstruction of the remaining 11 samples showed a similar pattern of singular attractors, indicating that the time series of umbilical artery blood signals were chaotic.

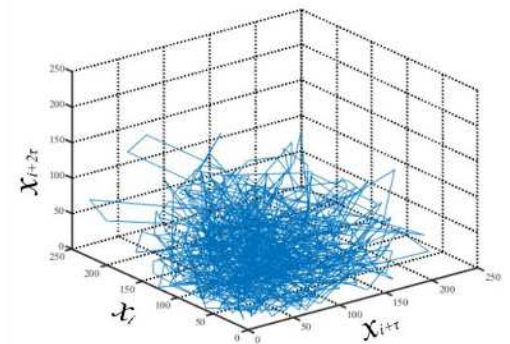
Another five normal umbilical artery blood time series are shown in Figure 4-5 as three-dimensional phase diagrams as well as two-dimensional phase diagrams.



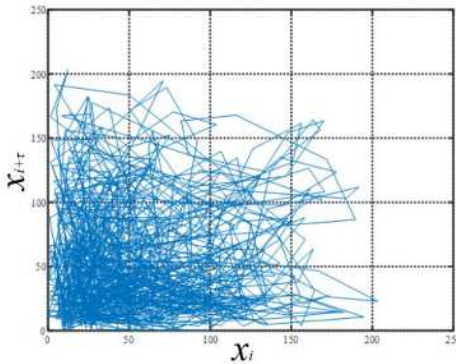
(a-1) Three-dimensional phase diagram of normal sample No. 2



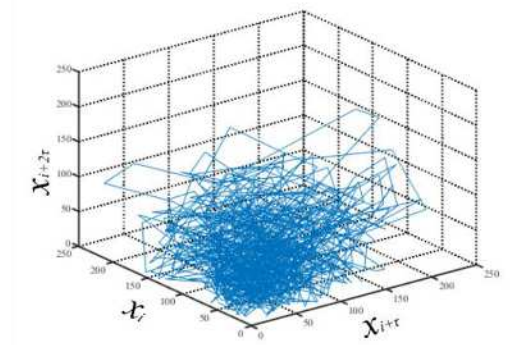
(a-2) x-y two-dimensional phase diagram of normal sample No. 2



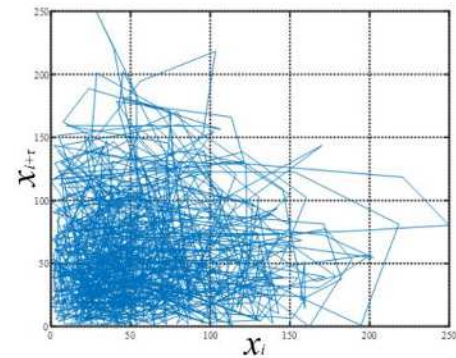
(b-1) Three-dimensional phase diagram of normal sample No. 3



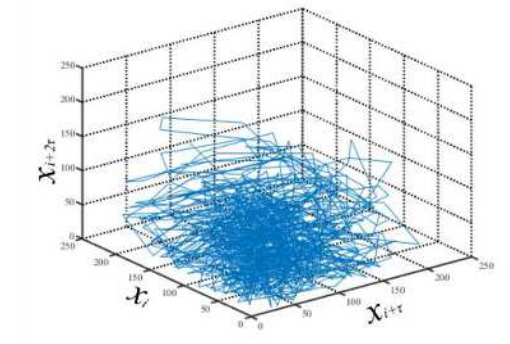
(b-2) x-y two-dimensional phase diagram of normal sample No. 3



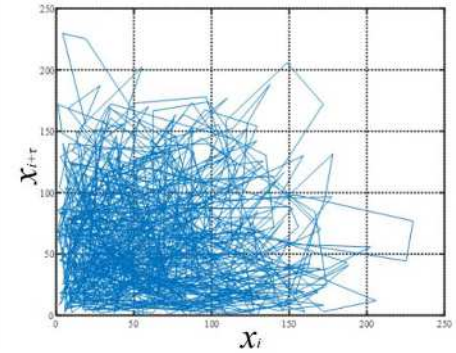
(c-1) Three-dimensional phase diagram of normal sample No. 4



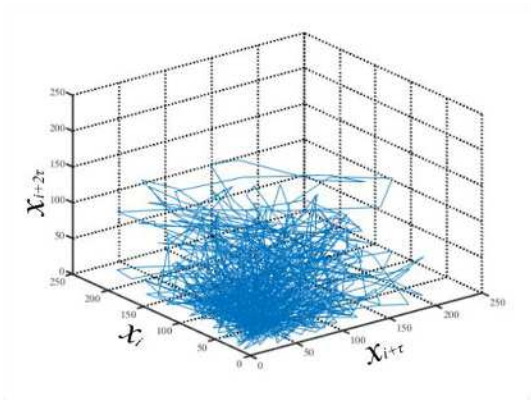
(c-2) x-y two-dimensional phase diagram of normal sample No. 4



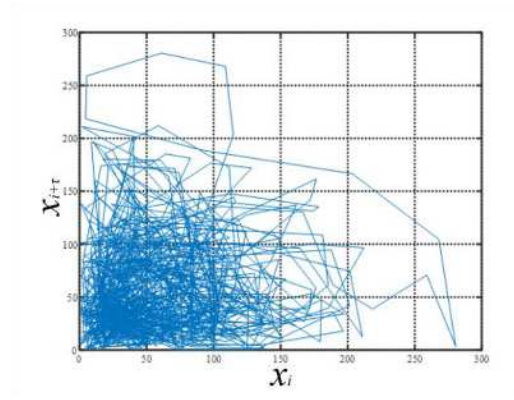
(d-1) Three-dimensional phase diagram of normal sample No. 5



(d-2) x-y two-dimensional phase diagram of normal sample No. 5



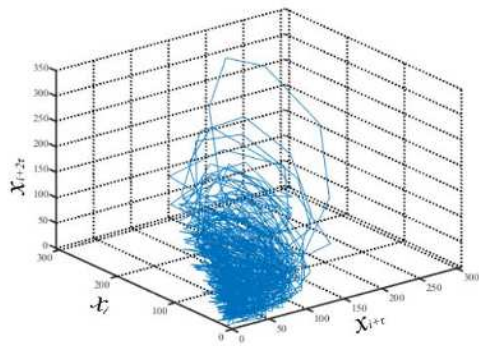
(e-1) Three-dimensional phase diagram of normal sample No. 6



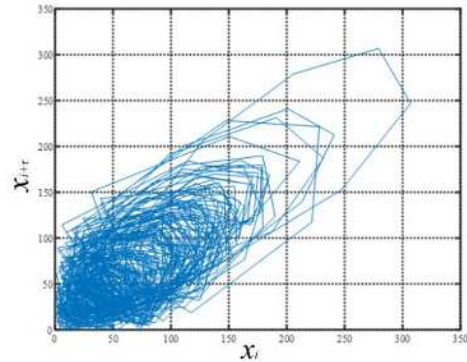
(e-2) x-y two-dimensional phase diagram of normal sample No. 6

Fig 4-5 Three-dimensional phase diagram and two-dimensional phase diagram of umbilical artery blood signal time series in normal group

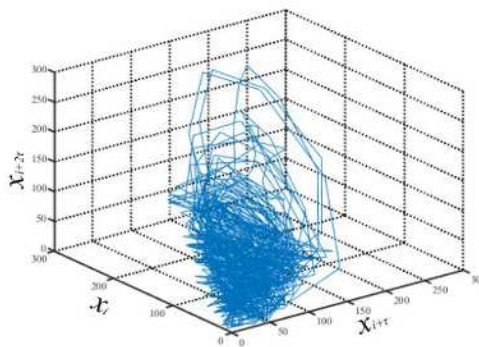
The phase diagram method was used to reconstruct the phase space for the abnormal umbilical artery blood time series to obtain chaotic phase diagrams for each umbilical artery blood signal time series, part results are shown in Figures 4-6 below for abnormal three-dimensional phase diagrams and two-dimensional phase diagrams of the umbilical artery blood time series, tagged as abnormal samples No. 7-12.



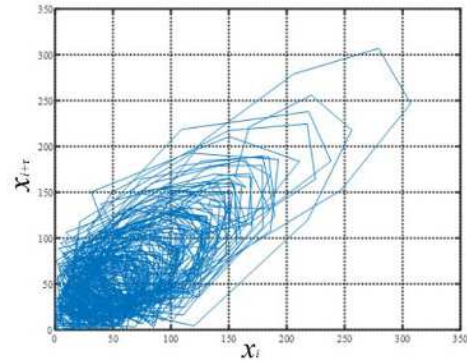
(a-1) Three-dimensional phase diagram of abnormal sample No. 7



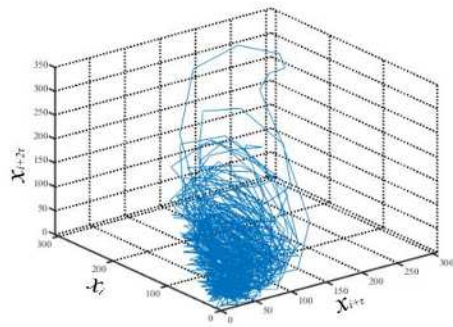
(a-2) x-y two-dimensional phase diagram of abnormal sample No. 7



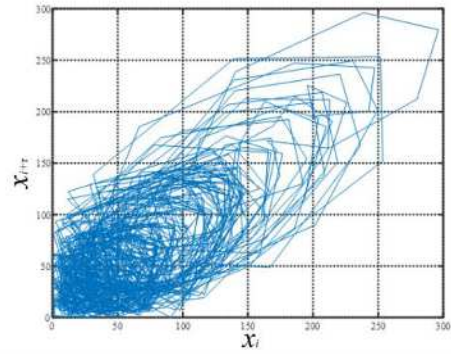
(b-1) Three-dimensional phase diagram of abnormal sample No. 8



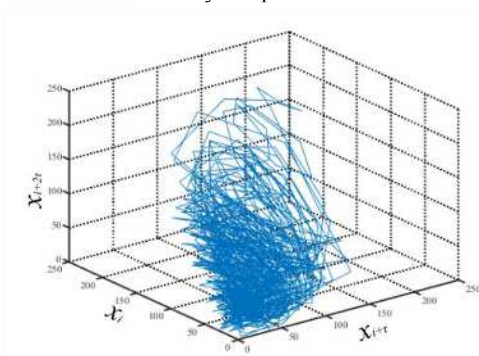
(b-2) x-y two-dimensional phase diagram of abnormal sample No. 8



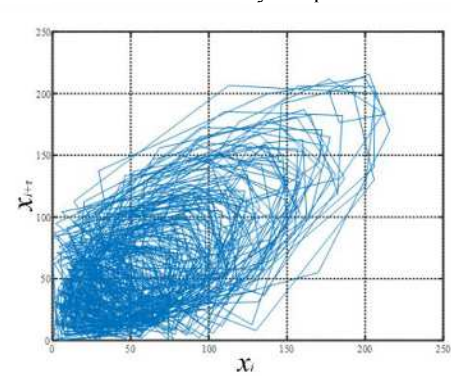
(c-1) Three-dimensional phase diagram of anomaly sample No. 9



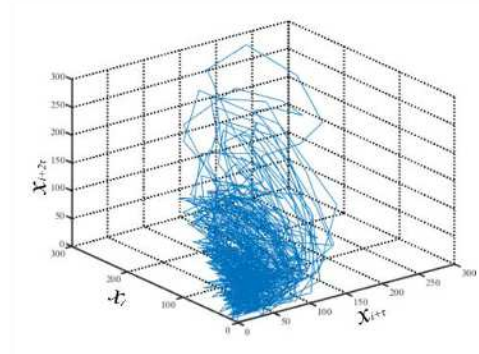
(c-2) x-y two-dimensional phase diagram of anomaly sample No. 9



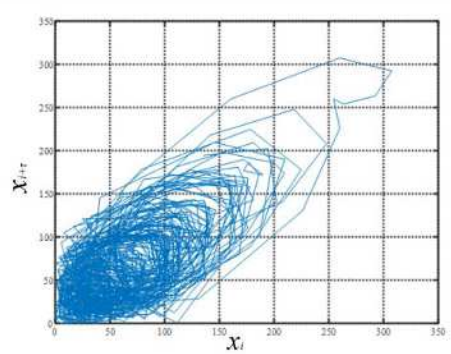
(d-1) Three-dimensional phase diagram of abnormal sample No. 10



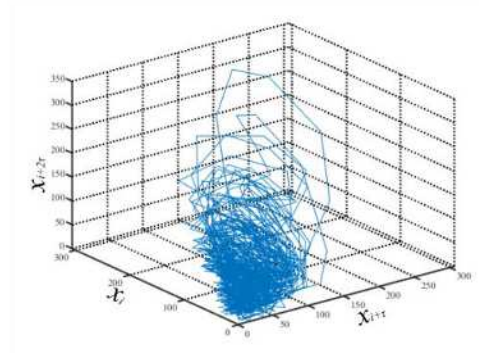
(d-2) x-y two-dimensional phase diagram of abnormal sample No. 10



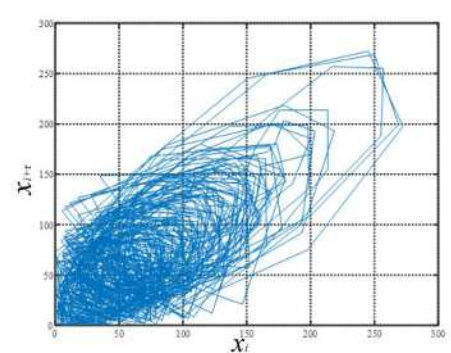
(e-1) Three-dimensional phase diagram of abnormal sample No. 11



(e-2) x-y two-dimensional phase diagram of abnormal sample No. 11



(f-1) Three-dimensional phase diagram of abnormal sample No. 12



(f-2) x-y two-dimensional phase diagram of abnormal sample No. 12

Figure 4-6 Three-dimensional phase diagram and two-dimensional phase diagram of umbilical artery blood signal time series in abnormal group

Compared to Figure 4-5, the chaotic 2-D phase diagram of the abnormal umbilical artery blood signal time series shown in Figure 4-6 is more dense in the form of a redundant ‘hairball’, which indicates that the time series is moving from orderly to chaotic. The chaotic ‘phase shape’ appears to be clustered due to the randomness of the signal caused by the heterogeneity of the flow fluctuations due to different pathologies. Chaotic phase diagrams can therefore qualitatively determine the abnormality of umbilical artery blood fluctuations.

4.3.2 Maximum Lyapunov Exponent method

In the last two decades of dynamical systems theory, the Lyapunov exponent has been widely used to identify chaotic behaviour. When the initial state of a system changes slightly, the trajectory lines resulting from two extremely close initial values separate exponentially in phase space over time, a phenomenon that can be described quantitatively by the Lyapunov exponent [44]. For n -dimensional systems with n Lyapunov exponents in the state space, there must be at least one positive Lyapunov exponent to determine that the system is chaotic.

In 1983, Gribo proved that whether the Maximum Lyapunov Exponent (MLE) is greater than 0 can be used as a basis for determining whether a time series is chaotic [45]. The basic idea is that after phase space reconstruction, a positive Lyapunov exponent measures the average divergence exponent of two neighboring trajectories, which are initially close and gradually separate over time. The more positive the Lyapunov exponent, the faster they move, then the distance between nearby orbits increases exponentially in time and the system exhibits a sensitive dependence on the initial conditions; while a negative Lyapunov exponent measures the convergence index of two neighboring trajectories, the trajectories converge in time and the dynamical system is insensitive to the initial conditions. If for a time series, this indicates that it is stochastic or periodic. Therefore, whether the MLE can be greater than 0 is an important criterion for the presence of chaotic behaviors of the system.

Although Abarbanel et al. [46], Iasemidis [47] and Mccaffrey et al. [48] have proposed improved algorithms for calculating Lyapunov indices from observations, Wolf's method [49] is still considered the most classical MLE algorithm.

Let the chaotic time series be $x(t_1), x(t_2), \dots, x(t_i), \dots$, the embedding dimension is m , the delay time is τ , and the phase space reconstruction of the time series be $R^m = X(t_i) = [X(t_1), X(t_2), \dots, X(t_{N+(m-1)\tau})]^T$. Take the initial point $X(t_0)$, set its distance from

the nearest neighbor $X_0(t_0)$ to L_0 , trace the time evolution of these two points until the distance between them exceeds a certain fixed value ε at the moment t_1 , i.e. $L'_0 = |X(t_0) - X(t_1)| > \varepsilon$, keep $X(t_1)$, and find the other nearest neighbor $X_1(t_1)$ of $X(t_1)$, making $L_1 = |X(t_1) - X_1(t_1)| < \varepsilon$, and continue the above process as shown in the schematic diagram in Figure 4-7.

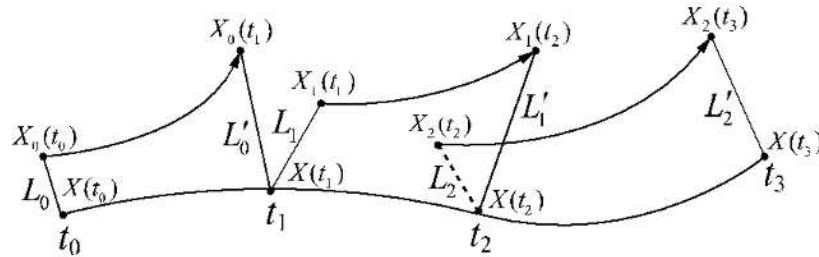


Fig.4-7 Schematic diagram of the Wolf method

Until $X(t)$ reaches the end of the time series, the total number of iterations M of the tracking evolution process is counted, and the MLE is expressed as:

$$\lambda = \frac{1}{t_M - t_0} \sum_{i=0}^M \ln \frac{L'_i}{L_i} \quad (4-10)$$

For the 36 normal and 36 abnormal umbilical artery blood signals, the MLE was computed based on the MLE calculation concept, and part results are displayed in Tables 4-1 and 4-2, respectively.

Table 4-1 Part results of the MLE for the normal group

| Serial number | 1 | 2 | 3 | 4 | 5 | 6 |
|---------------|---------|---------|---------|---------|---------|---------|
| MLE | -0.3884 | -0.2703 | -0.2429 | -0.1690 | -0.5396 | -0.0605 |
| Serial number | 7 | 8 | 9 | 10 | 11 | 12 |
| MLE | -0.0378 | -0.7557 | -0.5874 | -0.5936 | 0.0116 | -0.4869 |

Table4-2 Part results of the MLE for the abnormal group

| Serial number | 1 | 2 | 3 | 4 | 5 | 6 |
|---------------|--------|---------|---------|--------|--------|--------|
| MLE | 0.6173 | -0.0054 | 0.2937 | 0.6715 | 0.7844 | 0.3288 |
| Serial number | 7 | 8 | 9 | 10 | 11 | 12 |
| MLE | 0.3730 | 0.1427 | -0.0197 | 0.2061 | 0.9310 | 0.9249 |

4.3.3 Box plot and ROC of MLE

The box plot and ROC curves of MLE are shown in Figures 4-8 and Figure 4-9.

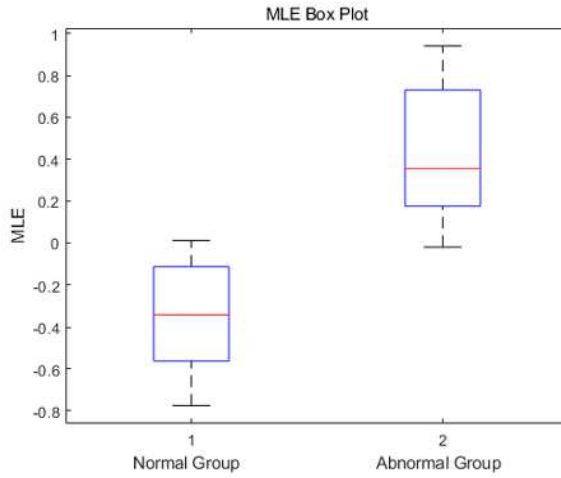


Fig.4-8 Box plot of MLE

Through Figures 4-8, we can clearly see the significant difference in MLE values between the normal and abnormal groups. Specifically, the median MLE value for the abnormal group is greater than zero, indicating that more than half of the data points in the abnormal group are located at or above zero. Conversely, the median MLE value for the normal group is below zero, signifying that over half of the data points in the normal group are positioned at or below zero. This observation is of paramount importance, as it has the potential to serve as a potential parameter, aiding in the differentiation of individuals between normal and abnormal states.

However, it is important to note that despite the conspicuous median difference, the maximum MLE value in the normal group still exceeds zero, while the minimum MLE value in the abnormal group falls below zero. This implies the presence of an overlap, which could potentially result in a certain degree of misdiagnosis when employing MLE for diagnosis. Therefore, in practical applications, it is imperative to conduct a more comprehensive exploration of the distribution characteristics of MLE values to determine suitable thresholds and standards, thereby mitigating the potential risk of misdiagnosis.

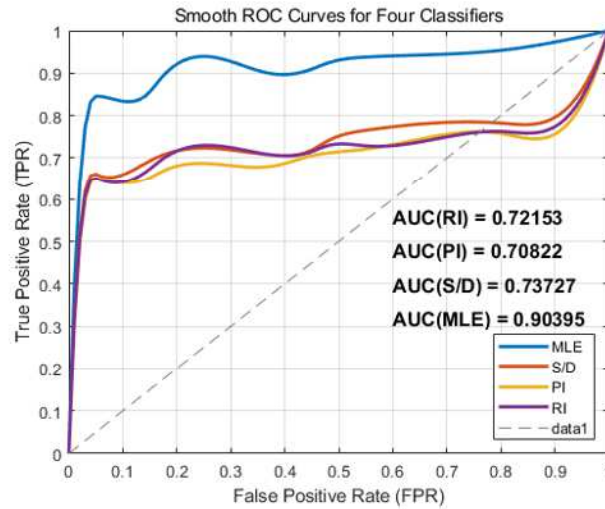


Fig.4-9 ROC of MLE and conventional parameters

A more detailed examination of Figure 4-9 reveals that the Receiver Operating Characteristic (ROC) area under the curve (AUC) for the Maximum Likelihood Estimation (MLE) method is 0.90395. This result is significantly superior to other methods, such as S/D with an ROC AUC of 0.73727, RI with an ROC AUC of 0.72153, and PI with an ROC AUC of 0.70822. This indicates that the MLE method demonstrates exceptional diagnostic accuracy, enabling a more precise differentiation between healthy and abnormal states. It is particularly noteworthy that the MLE method exhibits a significantly higher true positive rate (TPR) compared to other methods, signifying its heightened sensitivity in correctly diagnosing patients with the disease. This is of paramount importance, especially for diagnosis and treatment decision-making, as a high TPR aids in capturing status promptly, facilitating timely intervention.

These experimental findings underscore the immense potential of the MLE method in umbilical artery blood diagnosis, especially when compared to other methods. In ROC analysis, it demonstrates a larger area under the curve and superior diagnostic performance. This highlights the significance of the MLE method in achieving accurate disease diagnosis and improving the quality and timeliness of medical decision-making.

4.4 Summary

Through introducing the background, development process and basic concepts of chaos theory and phase space reconstruction theory, we focus on the calculation methods of phase space reconstruction parameters. On this basis, the chaotic characteristics of the signal time series of umbilical artery blood are identified using qualitative and quantitative methods.

1. The time series of the umbilical artery blood signal is reconstructed in three and two-dimensional phase space based on delay time attractors, and the chaotic characteristics of the time series of the umbilical artery blood signal are determined qualitatively.

2. The chaotic characteristics of the umbilical artery blood signal time series were determined quantitatively by studying the Wolf method of Lyapunov index and calculating the MLE of the umbilical artery blood signal time series. Receiver Operating Characteristic Curve (ROC) of MLE shows that MLE is significantly superior to conventional parameters in distinguishing the normality of umbilical artery blood signals.

4.5 References

-
- [1] Stermann J D. Deterministic chaos in models of human behavior: Methodological issues and experimental results[J]. *System Dynamics Review*, 1988,4(1-2): 148-178.
 - [2] Lv J H. Chaotic time series analysis and its applications [M]. Wuhan: Wuhan University Press, 2002.
 - [3] Wang W K. Shanghai Jiao Tong University Video Open Course: A Mathematical Journey - Chaos and Fractals [EB/OL]. (2013-03-06)[2016-10-18].http://open.163.com/movie/2013/3/T/5/M8PTB0GHI_M8PTB0GHI_M8S520LT5.html.
 - [4] Poincaré H. *Science and Method (Classic Reprint)* [J]. 2010.
 - [5] Hadamard J. Les surfaces a courbures opposees et leurs lignes geodesiques. *J. Math. Pures Appl.* 1898(4): 27-73.
 - [6] Poincaré H. *Science et Méthode* [J]. *La Revue Scientifique*, 1998(5).
 - [7] Broer H. KAM theory: The legacy of Kolmogorov's 1954 paper [J]. *Bulletin of the American Mathematical Society*, 2004,41(4): 16-28.
 - [8] Lorenz E N. Deterministic nonperiodic flow[J]. *Journal of Atmospheric Sciences*, 1963,20(2): 130-141.
 - [9] Grassberger P, Procaccia I. Measuring the strangeness of strange attractors[J]. *Physica D Nonlinear Phenomena*, 1983,9(1): 189-208.
 - [10] Ruelle D, Takens F. On the nature of turbulence[J]. *Communications in Mathematical Physics*, 1971,20(3): 167-192.
 - [11] Hao B L. *Chaos* [M]. World scientific publishing co singapore, 1984.
 - [12] Campbell D K, Peyrard M. *Chaos and order in non-integrable model field theories* [C]//Aip Chaos Conference. 1989.
 - [13] Marek M, Schreiber I. *Chaotic Behaviour of Deterministic Dissipative Systems* [M]. Cambridge University Press, 1991.
 - [14] Li T Y, Yorke J A. Period Three Implies Chaos[J]. *American Mathematical Monthly*, 1975, 82(10): 985-992.

- [15] May R. The best possible time to be alive: The logistic map [J]. *It Must Be Beautiful*, 1976: 28-45.
- [16] Casati G , Ford J . Stochastic behavior in classical and quantum hamiltonian Systems[J]. *Lecture Notes in Physics*, 1979, 93(93):1045-1058.
- [17] Feigenbaum M J. Quantitative universality for a class of nonlinear transformations [J]. *Journal of Statistical Physics*, 1978,19(1): 25-52.
- [18] Eckmann J P, Ruelle D. Ergodic-theory of chaos and strange attractors[J]. *Reviews of Modern Physics*,1985,57(3): 617-656.
- [19] Iasemidis, L D. Epileptic seizure prediction and control[J]. *IEEE Transactions on Biomedical Engineering*, 2003, 50(5): 549-558.
- [20] Sugihara G. Nonlinear forecasting as a way of distinguishing chaos from measurement error in time series[J]. *Nature*, 1990, (344): 734-741.
- [21] Scheinkman J A. Nonlinearities in economic dynamics[J]. *The Economic Journal*, 1990,100(400): 33-48.
- [22] Frison T W, Abarbanel H D I, Earle M D, et al. Chaos and predictability in ocean water levels[J]. *Journal of Geophysical Research*, 1999,104(C4): 7935-7951.
- [23] Abarbanel H D I, Kennel M B. Synchronizing High-Dimensional Chaotic Optical Ring Dynamics[J]. *Physical Review Letters*, 1998,80(14): 3153-3156.
- [24] Glass L, Guevara M R, Shrier A, et al. Bifurcation and chaos in a periodically stimulated cardiac oscillator[J]. *Physica D Nonlinear Phenomena*, 1983,7(1): 89-101.
- [25] Goldberger A L, Rigney D R, West B J. Chaos and Fractals in Human Physiology[J]. *Scientific American*, 1990,262(2): 42-49.
- [26] Guzzetti S, Signorini M G, Cogliati C, et al. Non-linear dynamics and chaotic indices in heart rate variability of normal subjects and heart- transplanted patients[J]. *Cardiovascular Research*, 1996,31(3): 441-446.
- [27] Notley S V, Elliott S J. Efficient estimation of a time-varying dimension parameter and its application to EEG analysis[J]. *IEEE Transactions on Biomedical Engineering*, 2003,50(5): 594-602.
- [28] Peng J, Peng C L. Application of chaos theory and methods in medical signal processing[J]. *International Journal of Biomedical Engineering*, 2006,29(02): 124-127.
- [29] Fang J Q. *Harnessing Chaos and Developing High Technology* [M]. Beijing: Atomic Energy Press, 2002.
- [30] Cao J F. *Theory and applications of nonlinear systems* [M]. Xi an: Xi an Jiao Tong University Press, 2001.
- [31] Li Q. *Application of integrated evaluation and non-linear prediction in post-project evaluation* [D]. Tianjin University, 2009.
- [32] Liu, S. D. *Fractals in physics* [M]. Beijing: Peking University Press, 2014.
- [33] Jaqueline L, Donner R V. Phase space reconstruction for non-uniformly sampled noisy time series[J]. *Chaos: An Interdisciplinary Journal of Nonlinear Science*, 2018, 28(8): 085702.

- [34] Takens F. Detecting strange attractors in turbulence [C]//Rsand D A, Young L S. Dynamical systems and turbulence, Lecture Notes in Mathematics. New York: spriger-verlay, 1981,16(6): 366-381.
- [35] Stine, Robert A. Analysis of Observed Chaotic Data[J]. Technometrics, 1997,39(3): 334-335.
- [36] Zhu H, Ji C C. Fractal theory and its applications [M]. Beijing: Science Press, 2011.
- [37] Jiang A H, Zhou P, Zhang Y, et al. Research on the improvement algorithm of mutual information of phase space reconstruction delay time[J]. Vibration and Shock, 2015,34(2): 79-84.
- [38] Xiu C B, Liu X D, Zhang Y H. Selection of delay time and embedding dimension for phase space reconstruction[J]. Journal of Beijing University of Technology, 2003,23(2): 219-224.
- [39] Kim H S, Eykholt R, Salas J D. Nonlinear dynamics, delay times, and embedding windows [M]. Elsevier Science Publishers B. V, 1999.
- [40] Hsieh, David A. Nonlinear dynamics, chaos, and instability[M]. MIT Press, 1993.
- [41] Li Y M, Cheng Y, Liu X T. Research on wind speed time series hybrid prediction method[J]. Journal of Tianjin University of Technology, 2013,32(5): 47-50.
- [42] Berrou C, Glavieux A, Thitimaishima P. Near Shannon limit error-correcting coding and decoding: turbo-codes (1) [C]//Communications, 1993:1064- 1070.
- [43] Fu Y. Extraction and analysis of the chaotic characteristics of the stock market[J]. Chinese & Foreign Entrepreneurs, 2015,46(4): 99-101.
- [44] Ma H G, Han C Z. Chaos and Fault Diagnosis in Circuits [M]. Beijing: National Defense Industry Press, 2006.
- [45] Guo B H. Chaotic time series analysis of oil-water two-phase flow patterns[D]. Tianjin: Tianjin University, 2005.
- [46] Abarbanel H D I, Brown R, Kennel M B. Lyapunov exponents in chaotic systems: their importance and their evaluation using observed data[J]. International Journal of Modern Physics B, 1991,5(09): 1347-1375.
- [47] Iasemidis L. On the dynamics of the human brain in temporal lobe epilepsy [D]. PhD thesis, University of Michigan, Ann Arbor, 1991.
- [48] Mccaffrey D F, Ellner S, Gallant A R, et al. Estimating the Lyapunov Exponent of a Chaotic System with Nonparametric Regression[J]. Publications of the American Statistical Association, 1992,87(419): 682-695.
- [49] Wolf A, Swift J B, Swinney H L, et al. Determining Lyapunov exponents from a time series[J]. Physica D Nonlinear Phenomena, 1985,16(3): 285-317.

Chapter 5

Composite multi-scale feature extraction and diagnosis for umbilical artery blood

In the age of digital medical technology, biomedical data is exploding and the era of big biomedical data has arrived [1]. It is a huge challenge for researchers to handle and interpret the huge amount of biomedical data. In recent years, Artificial Intelligence (AI) technology, with machine learning at its core, has impacted a wide range of fields, such as unmanned driving, face recognition, machine vision, expert systems, bioinformatics, intelligent search and computer-aided medical diagnosis [2-3]. AI in the biomedical field will play a significant role in uncovering hidden information in biomolecular data, improving the accuracy of pathological diagnosis, enhancing clinical diagnosis and improving personalized health management [4].

Two important research directions in the application of artificial intelligence technology to the biomedical field are: clinical diagnosis and bioinformatics data mining. For the field of clinical diagnosis, through the extraction and pre-processing of diagnostic data to form diagnostic datasets, machine learning algorithms and feature selection are used to construct disease classification and prediction models to provide decision support for doctors' clinical aids to diagnostic tools and rational treatment plans.

5.1 Introduction to machine learning

Artificial intelligence is the study of the acquisition of knowledge and its use by machines, based on machine learning (ML) algorithms that give computers the ability to generalize and build intelligent models to achieve artificial intelligence [5-6]. Machine learning can perform a variety of tasks, including complex tasks such as classification, regression and clustering [7].

Although deep learning (DL), which extends machine learning with feature engineering, has a strong learning capability and is an end-to-end approach, it has some application limitations due to the large number of learning samples required, for this reason, traditional machine learning and achieving intelligent classification tasks by virtue of human experience is more in line with engineering needs in medical applications [8-9].

Multi-label learning (MLL) is also part of machine learning [10-11], where a new sample input to a model trained on a multi-semantic sample outputs all possible related one-semantic sets, and it is widely used in genetic engineering and medical diagnosis [12]. The relationship between artificial intelligence, machine learning, deep learning and multi-tagged learning is shown in Figure 5-1.

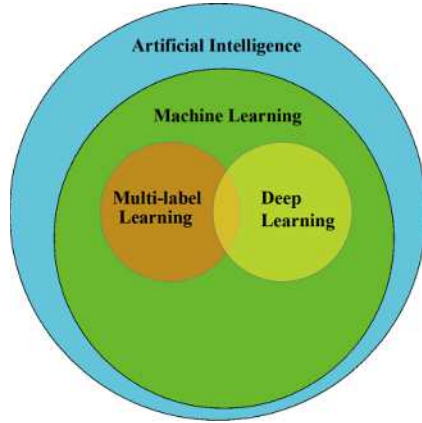


Figure 5-1 Relationships between AI, ML, DL and MLL

5.2 Datasets and classifiers

5.2.1 Definition

Definition 5-1 Data set

The dataset is a two-dimensional data table with rows as records and columns of features, represented by the triad $D = \langle I, X, Y \rangle$, where (1) I is the record identifier, used to uniquely identify a sample; (2) X is the set of classification features, consisting of N features, noted as $X = \{X_1, X_2, \dots, X_N\}$; and (3) Y is the target feature, used to identify the category of the sample.

Definition 5-2 Classifier

A classifier is defined as: for a given data set, a function whose independent variable is the categorical feature and whose dependent variable is the target feature $y = h(x)$, for a given sample $x = \{x_1, x_2, \dots, x_n\}$, whose category can be determined by the classifier y , where $x \in X, y \in Y$.

5.2.2 Classifier performance

Accuracy, Specificity and Sensitivity are three common metrics used to evaluate the performance of classifiers, which can be calculated using a confusion matrix that represents the relationship between the true class attributes and the predicted class attributes. The confusion matrix for a binary classification problem is shown in Table 5-1 below.

Table 5-1 Confusion matrix for binary classification

| | | Predicted classes | |
|--------------|----|---------------------|---------------------|
| | | C1 | C2 |
| Actual class | C1 | True Positive (TP) | False negative (FN) |
| | C2 | False Positive (FP) | True Negative (TN) |

In Table 5-1, given two classes of positive samples (Positives, C1) and negative samples (Negatives, C2), True positives (TP) refers to the number of positive samples that were correctly labeled (predicted to be positive and actually positive), False positives (FP) refers to the number of incorrectly labeled negative samples (predicted positive, actual negative), True negatives (TN) refers to the number of correctly labeled negative samples (predicted negative, actual negative), and False negatives (FN) refers to the number of incorrectly labeled positive samples (predicted negative, actual positive).

Definition 5-3 Accuracy

Labeled Accuracy represents the recognition rate of the classifier for the total sample and is calculated as shown in Equation 5-1.

$$Accuracy = (TP + TN) / (TP + FP + FN + TN) \quad (5-1)$$

Definition 5-4 Specificity

labeled Specificity, indicates the recognition rate of the classifier for negative samples and is calculated as shown in Equation 5-2.

$$Specificity = TN / (TN + FP) \quad (5-2)$$

Definition 5-5 Sensitivity

labeled Sensitivity, indicates the classifier's ability to identify positive samples and is calculated as shown in Equation 5-3.

$$Sensitivity = TP / (TP + FN) \quad (5-3)$$

Definition 5-6 Checking completeness rate

The check-all rate, noted as Recall, represents the ratio of correctly classified positive samples to all positive samples, and the formula is shown in 5-4.

$$Recall = TP / (TP + FN) \quad (5-4)$$

Definition 5-7 Precision

The precision represents the proportion of correctly classified positive samples out of the sum of incorrectly classified negative samples and correctly classified positive samples and is calculated as shown in Equation 5-5.

$$Precision = TP / (TP + FP) \quad (5-5)$$

Definition 5-8 True Rate

The true rate represents the ratio of samples of a category (positive or negative) to all samples of that category that are correctly classified. For positive samples (minority samples), the true rate is labelled $TPRMin$ and for negative samples (majority samples), the true rate is labelled $TPRMaj$. The calculations are shown in equations 5-6 and 5-7 respectively as follows.

$$TPRMin = TP / (TP + FN) \quad (5-6)$$

$$TPRMaj = TN / (TN + FP) \quad (5-7)$$

As can be seen from the definitions, $TPRMin$ is equivalent to Recall and Sensitivity, while $TPRMaj$ is equivalent to *Specificity*.

5.3 Multi-scale feature extraction and diagnosis for umbilical artery blood signal

5.3.1 SVM

In 1995, Professors Cortse and VAPNIK of Bell labs proposed the theory of Support Vector Machines (SVM) [13-14], which is a machine learning algorithm based on structural risk minimization to solve small samples with high-dimensional space recognition. The aim of the SVM method is to transform non-separable on problems in low-dimensional space into separable problems in high-dimensional space [15-16], thus solving the non-linear classification problem and solving the problem of model complexity due to high-dimensional patterns by introducing kernel functions [17].

1. Optimal classification hyperplane

The classification principle of SVM is to find an optimal classification hyperplane that satisfies the classification accuracy while maximizing the blank area on both sides of the plane, based on the premise that the classification is correct. SVM classification problems can be classified as: linearly divisible, linearly indivisible, and approximately linearly divisible.

The basic idea of SVM can be illustrated by two types of linearly divisible cases as shown in Figure 5-2 [18].

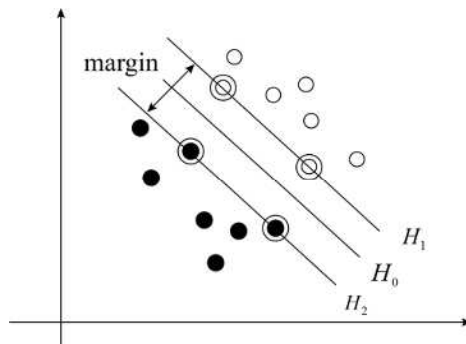


Fig.5-2 Optimal classification hyperplane

In Figure 5-2, solid and hollow circles are used to represent negative and positive class samples respectively. Assume that the two types of samples can be correctly separated by a line of analytical formula $\omega \cdot x + b = 0$ with ω as the normal vector and b as the intercept. The lines H_1, H_2 respectively, are the sample points passing through the closest of the two classes of samples to the classification line, and their analytical formula are $\omega \cdot x + b = -1$ and $\omega \cdot x + b = 1$, respectively, such that H_0 is the bisector between H_1 and H_2 respectively. The classification interval that can be maximized by adjusting ω and b is known as the unique optimal hyperplane H_0 [19]. The size of the classification interval depends on the samples of the straight lines H_1 and H_2 , which are called Support Vector.

2. linear support vector machines

(1) Linear support vector classifier

For a sample set of linear data:

$$\{(x_1, y_1), (x_2, y_2), \dots, (x_n, y_n)\} \quad (5-8)$$

Where: $x \in R^n, y \in \{-1, 1\}$.

Suppose there exists a discriminant function:

$$f(x) = \text{sgn}(\omega \cdot x + b) \quad (5-9)$$

The optimization problem needs to be constructed to maximize the distinction between the two types of samples:

$$\begin{aligned} \min \frac{1}{2} \|\omega\|^2 \\ \text{s.t. } y_i(\omega \cdot x + b) - 1 \geq 0 \quad i = 1, 2, \dots, n \end{aligned} \quad (5-10)$$

Solving the above equation yields:

$$\begin{aligned} \omega &= \sum_{i=1}^n \alpha_i y_i x_i \\ b &= y_i - \sum_{i=1}^n y_i \alpha_i (x_i \cdot x_j) \end{aligned} \quad (5-11)$$

A linear discriminant function is obtained as follows:

$$f(x) = \text{sgn}\left(\sum_{i=1}^n \alpha_i y_i (x \cdot x_i) + b\right) \quad (5-12)$$

(2) Linear support vector regression machine

Support vector machine regression algorithms for data regression prediction are an important branch of multivariate statistical analysis. For a set of linear data sample sets:

$$T = \{(x_1, y_1), (x_2, y_2), \dots, (x_n, y_n)\} \quad (5-13)$$

Construct the equation of the fitted curve of input x and output y as:

$$f(x) = W^T x + b \quad (5-14)$$

Where: W and b are the weighting factor and bias term respectively. Since the fitted curve is generally not a true curve equation and there is error, it is necessary to define an insensitive loss function to keep the error within the tolerance range, the mathematical expression is:

$$L^\varepsilon(x, y, f) = |y - f(x)|_\varepsilon = \max(0, |y - f(x)| - \varepsilon) \quad (5-15)$$

Where: ε is a small positive number. The insensitive loss function can also be represented graphically, see Figure 5-3.

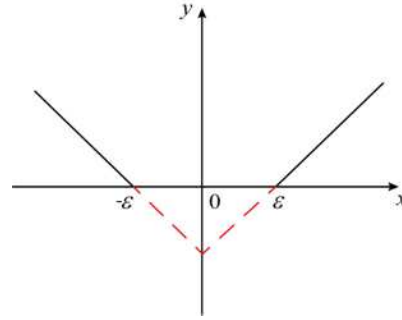


Fig. 5-3 ε Insensitive error function

When $\varepsilon = 0$, equation 5-15 is equivalent to the absolute error function; when $\varepsilon \neq 0$, equation 5-15 is equivalent to the two rays of the absolute error function shifted left and right by the distance of ε respectively.

Ideally, all training data should be in a pipeline with a radius of ε , which is the insensitive loss region or ε pipeline. Maximising this region allows the maximum possible number of unknown points to fall into this region, and the original regression problem is then transformed into an optimisation problem:

$$\min \frac{1}{2} \|W\|^2 = \|W\|^2 + 1 \quad (5-16)$$

3. Non-linear support vector machines

The linearly indistinguishable case is the most common problem in practical applications of pattern recognition, as shown in Figure 5-4.

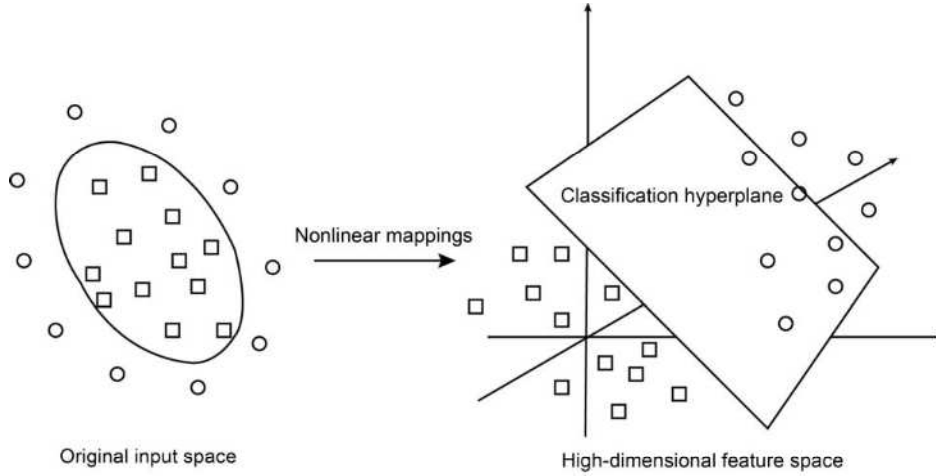


Fig. 5-4 Schematic diagram of a nonlinear mapping

In Figure 5-4, the non-linear problem in the low-dimensional original input space is transformed into a linear problem in the high-dimensional feature space by a nonlinear mapping, and then the optimal classification hyperplane is constructed.

When dealing with non-linear data sets, the training sample features need to be mapped to a high-dimensional linear space by means of the mapping function $\phi(x)$, bringing $\phi(x)$ into the optimization problem at:

$$\min \frac{1}{2} \sum_{i=1}^n \sum_{j=1}^n y_i y_j \alpha_i \alpha_j (\phi(x_i) \cdot \phi(x_j)) + \sum_{i=1}^n \alpha_i \quad (5-17)$$

$$\begin{aligned} \text{s.t. } & \sum_{i=1}^n y_i \alpha_i = 0 \\ & 0 \leq \alpha_i \leq C \quad i = 1, 2, \dots, n \end{aligned} \quad (5-18)$$

Let $K(x_i, x_j) = \phi(x_i) \phi(x_j)$, the original problem is transformed into:

$$\min \frac{1}{2} \sum_{i=1}^n \sum_{j=1}^n y_i y_j \alpha_i \alpha_j K(x_i \cdot x_j) + \sum_{i=1}^n \alpha_i \quad (5-19)$$

$$\begin{aligned} \text{s.t. } & \sum_{i=1}^n y_i \alpha_i = 0 \\ & 0 \leq \alpha_i \leq C \quad i = 1, 2, \dots, n \end{aligned} \quad (5-20)$$

The non-linear discriminant function is:

$$f(x) = \text{sgn}(\alpha_i y_i K(x \cdot x_i) + b) \quad (5-21)$$

Where: $K(x_i, x)$ is called the kernel function. In SVM, input features are mapped to the Point product eigenspace and the mapping function $\phi(x)$ is replaced with a kernel function that satisfies the Mercer condition.

4. Approximate divisibility problems

Such problems are approximately linearly divisible if a small number of linearly indivisible sample points can be removed from the training sample and the remaining sample points are linearly divisible, as shown in Figure 5-5.

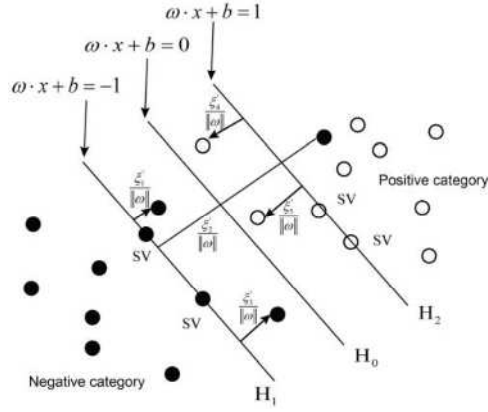


Fig. 5-5 Approximate linear divisibility problem

Since the linearly divisible problem, relaxation variables $\xi_i \ i = 1, 2, \dots, l$ are introduced to allow for the presence of misclassified samples. To keep the number of misclassified samples as small as possible, penalty factors $C \ (C > 0)$ are introduced to indicate the strength and importance of the penalty for misclassification cases. This gives the original optimization problem for an approximately linearly separable support vector machine, also known as a Soft Margin SVM.

$$\left\{ \begin{array}{l} \min \frac{1}{2} \|w\|^2 + C \sum_{i=1}^l \xi_i \\ s.t. y_i (w \cdot x_i + b) \geq 1 - \xi_i \ i = 1, 2, \dots, l \\ \xi_i \geq 0, i = 1, 2, \dots, l \end{array} \right. \quad (5-22)$$

Equation 5-22 also reflects the idea of the structural risk minimization principle, with the first term of the objective function reflecting the principle of maximizing the classification interval and the second term reflecting the minimization of the classification error. C is the weighting factor that regulates these two objectives. The pairwise problem for an approximate linearly separable support vector machine is:

$$\left\{ \begin{array}{l} \max_{\alpha} -\frac{1}{2} \sum_{i=1}^l \sum_{j=1}^l y_i y_j \alpha_i \alpha_j (x_i \cdot x_j) + \sum_{i=1}^l \alpha_i \\ s.t. \sum_{i=1}^l \alpha_i y_i = 0 \\ 0 \leq \alpha_i \leq C, i = 1, 2, \dots, l \end{array} \right. \quad (5-23)$$

Where α_i is the Lagrange multiplier corresponding to the i th sample and there is a unique optimal solution to the pairwise problem α^* . The linearly divisible and approximately linearly divisible dyadic problems are essentially the same, differing only in the constraints on the Lagrange multipliers. The expression of the optimal decision function and the computational procedure for the approximately linearly divisible case are the same as those for the linearly divisible case.

5.3.2 SVM classification of umbilical artery blood signal with conventional parameters

As described in the previous 5.3.1, SVM is a typical binary classification model whose aim is to find hyperplanes to partition the sample data, with the objective of maximizing the separation interval and transforming the separation problem into a convex quadratic programming problem. For when the samples are linearly inseparable, a non-linear SVM is learned by soft interval maximization with the kernel trick.

First, using the umbilical artery blood S/D value, pulsatility index (PI) and resistance index (RI) as features parameters, the data of 120 were divided into 30 groups for each of the four states of normal, oligohydramnios, umbilical cord around neck and fetal malposition, with labels 1, 2, 3 and 4 respectively. Label them and take 20, 5, 5 data from each group as training set, test set and validation set respectively. The training set, test set and validation set have 80, 20, 20 sets of data respectively.

To avoid the chance of sample selection affecting the accuracy, 20 of the 30 groups of samples were randomly selected as training samples. After completing for a total 10 experiments, the totally average accuracy rate is 68.75% and some of the experimental results are shown in Figure 5-6.

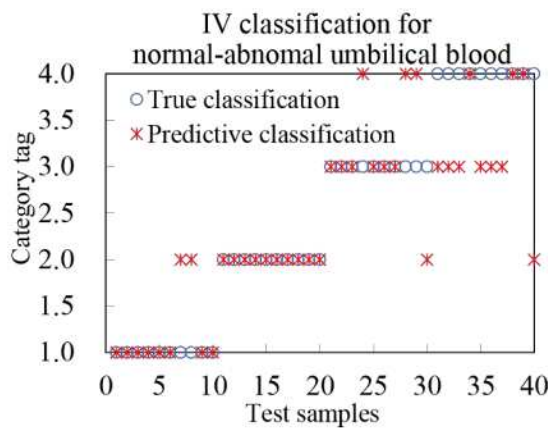


Fig.5-6 Results of SVM classification of umbilical artery blood with conventional parameters

As can be seen in Figure 5-6, the accuracy of the SVM classifier was not satisfactory for the quadruple classification of normal, oligohydramnios, umbilical cord around neck and malposition based on three-dimensional data samples with S/D, PI and RI as features of umbilical artery blood.

5.3.3 PSO-SVM classification of umbilical artery blood signal with conventional parameters

Considering that the selection of the kernel and normalization parameters has a large impact on the accuracy of the SVM, and that excellent parameter selection can enhance the generalization ability of the SVM, the Particle Swarm Optimization (PSO) algorithm is introduced to optimize the selection of the kernel and normalization parameters.

1. Particle Swarm Optimization

The Particle Swarm Optimization (PSO) algorithm was proposed by Eberhart et al. and was inspired by the foraging behavior of a flock of birds [20]. In the PSO algorithm, each particle has a corresponding velocity and position to adjust its own state, and the position of the particle represents a potential solution to the problem to be optimized. The PSO algorithm is described mathematically as follows:

In the D -dimensional space, there exists a population consisting of m particles, the position vector of the i th particle in D -dimensional space is $X_i = (x_{i1}, x_{i2}, \dots, x_{iD})^T$ and its velocity vector is $V_i = (v_{i1}, v_{i2}, \dots, v_{iD})^T$. The best position of the i th particle is represented by vector $P_i = (p_{i1}, p_{i2}, \dots, p_{iD})^T$, the best position of the population is represented by vector $P_g = (p_{g1}, p_{g2}, \dots, p_{gD})^T$, and the update of velocity and position is shown by Equation (5-24) and Equation (5-25) [21].

$$v_{id}^{k+1} = \omega v_{id}^k + c_1 \eta (p_{id} - x_{id}^k) + c_2 \eta (p_{gd} - x_{id}^k) \quad (5-24)$$

$$x_{id}^{k+1} = x_{id}^k + v_{id}^{k+1} \quad (5-25)$$

Where, $i = 1, 2, \dots, m$; $d = 1, 2, \dots, D$; k is the current evolutionary generation; c_1 and c_2 are learning factors; ω is inertia weights and η is random numbers within [0,1].

2. Optimization parameters

The optimization search process of the PSO kernel parameters and regularization parameters is shown in Figure 5-7. The initial position of the particle swarm is determined by the initial values of the kernel parameters and regularization parameters, and its optimization fitness function is determined by the accuracy of the SVM. The objective of the optimization search is the highest accuracy rate.

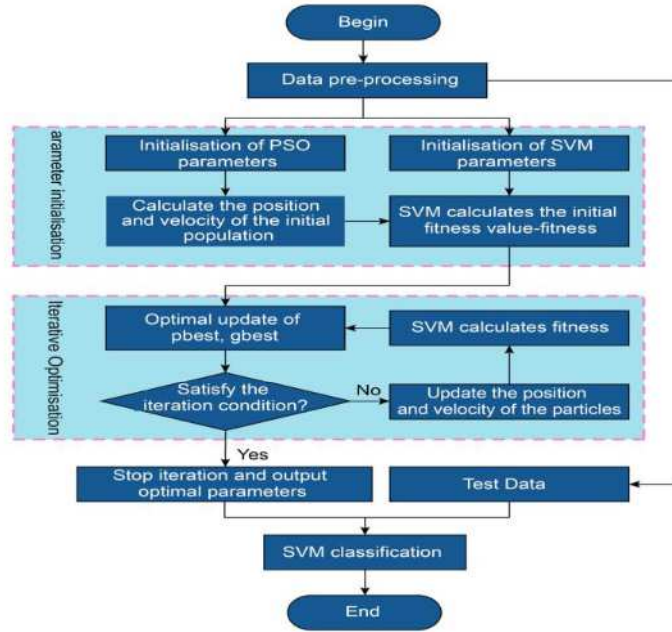


Fig. 5.7 PSO seeking flow diagram

S/D, PI and RI are still used as the feature parameters, and the sample division is the same as 5.3.2, and among the 30 groups of samples, 20 groups are randomly selected as the training samples, 5 groups as the test samples, and 5 groups as the validation samples, and the average accuracy of PSO-SVM reaches 72.75% after the adoption of PSO-SVM. Although the accuracy of the PSO-SVM classification method is improved by about 4% over the PSO classification method, the results are still not satisfactory.

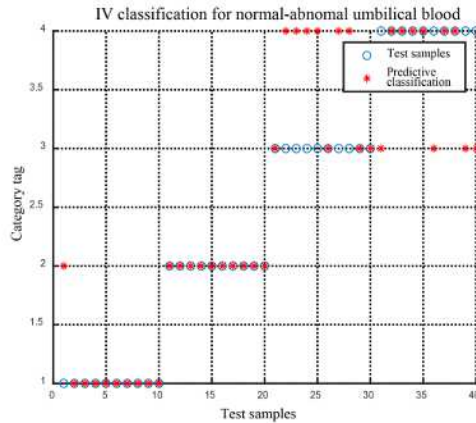


Fig.5-8 Results of PSO-SVM classification for umbilical artery blood with conventional parameters

The reason for this is that the features approach loses the original information of the data, resulting in a lower accuracy of the SVM test set performance. In the next section we consider a classification study using nonlinear feature classification.

5.3.4 PSO-SVM classification of umbilical artery blood signal with nonlinear parameters

In this section, the three features of S/D, PI, and RI in 5.3.3 were replaced by the fractal box dimension, correlation dimension and MLE as the new non-linear parameters proposed for PSO-SVM state classification.

The partial results of the normalization of the non-linear characteristics of the four states are shown in Table 5-2.

Table 5-2 Non-linear characteristics normalization matrix

| Lable | Status | Box dimension | Correlation dimension | MLE |
|-------|----------------------------|---------------|-----------------------|--------|
| 1 | Normal state | -0.170 | -0.549 | -0.254 |
| 2 | Umbilical cord around neck | -0.881 | 0.003 | 0.253 |
| 3 | Oligohydramnios | 0.120 | -0.396 | 0.965 |
| 4 | Fetal malposition | 0.130 | -0.533 | 0.210 |

The 120 clinical data were divided into 30 groups for each of the four states of normal status, oligohydramnios, umbilical cord around neck, and fetal malposition, corresponding to tags 1, 2, 3 and 4. The results showed that the PSO-SVM intelligent classification model with non-linear parameters performed better in diagnosing umbilical artery blood abnormalities. The classification accuracy based on non-linear parameter features is 9% higher with PSO-SVM compared to using S/D, PI and RI as feature parameters.

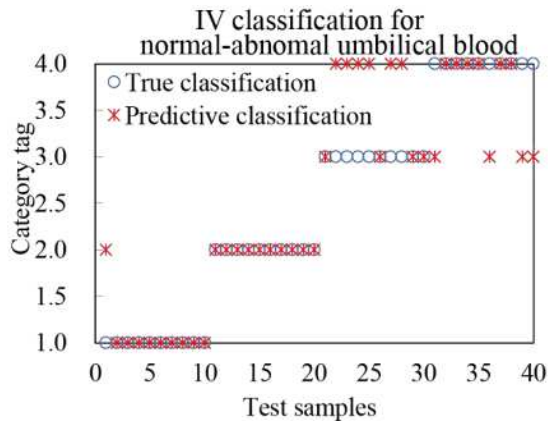


Fig.5-9 Results of PSO-SVM classification for umbilical artery blood with nonlinear parameters

Table 5-3 demonstrates that the SVM can classify umbilical artery blood time series, and that the PSO-SVM with can further improve state classification performance and increase the precision of the classification diagnosis. The PSO-SVM with non-linear parameters is more accurate because the feature parameters contain more representative characteristics of non-linear problems.

Table 5-3 Accuracy rates of different methods

| Model | Diagnostic accuracy/% |
|---------------------------|-----------------------|
| SVM (S/D、PI、RI) | 68.75 |
| PSO-SVM (S/D、PI、RI) | 72.75 |
| NC-PSO-SVM (BD、CD、MLE) | 77.5 |

5.4 Summary

The fundamental theory of SVM and PSO is introduced in this chapter. An intelligent diagnosis model based on the integration of an artificial intelligence algorithm is proposed to address the issue of low accuracy of early umbilical blood pathology diagnosis due to human experience.

The Support Vector Machine (SVM) classifying method is constructed based on the conventional parameters, S/D, PI and RI. The particle swarm optimization (PSO)-SVM classification of umbilical artery blood with conventional parameters was constructed. The box dimension, correlation dimension and MLE derived from Chapter 3 and Chapter 4 are used as feature parameters to construct nonlinear characteristic PSO-SVM classifying method. The results of the classification tests show that the PSO-SVM with nonlinear parameters classifying method has higher accuracy, which is confirmed that the proposed classifying method is useful and effective.

5.5 References

- [1] Ning K, Chen T. Current status and outlook of biomedical big data[J]. Science Bulletin, 2015,(Z1): 534-546.
- [2] Bishnoi L, Singh S N . Artificial Intelligence Techniques Used in Medical Sciences: A Review[C]// 2018:1-8.
- [3] Chakrobartty S, El-Gayar O F . Explainable Artificial Intelligence in the Medical Domain: A Systematic Review[C]// Americas Conference on Information Systems. 2021.
- [4] Li C Y, Zhang W W. Cluster analysis of global research hotspots on big data and health management[J]. China Hospital Management, 2016,36 (10): 63-65.
- [5] Lecun Y, Bengio Y, Hinton G. Deep learning[J]. Nature, 2015,521(7553): 436-444.
- [6] Schmidhuber J, rgen. Deep learning in neural networks[M]. Elsevier Science Ltd, 2015.
- [7] Zhou Z H. Machine learning [M]. Beijing: Tsinghua University Press, 2016.
- [8] Deng L , Yu D. Deep learning: methods and applications[J]. Foundations & Trends in Signal Processing, 2014,7(3): 197-387.
- [9] Bengio Y, Courville A, Vincent P. Representation Learning: A Review and New Perspectives[J]. IEEE

- Transactions on Pattern Analysis and Machine Intelligence, 2013,35(8): 1798-1828.
- [10] Feng X D. A review of multi-label classification problems[J]. Information Systems Engineering, 2016, (03): 137.
- [11] Yu Y. A review of multi-tagged learning research[J]. Computer Engineering and Applications, 2015,51(17): 20-27.
- [12] Li Z X, Zhuo Y Q, Zhang C L, et al. A review of multi-tagged learning research[J]. Computer Application Research, 2014,31(06): 1601-1605.
- [13] Vapnik V N. An overview of statistical learning theory[J]. IEEE Transactions on Neural Networks, 1999,10: 988-999, doi: 10.1109/72.788640.
- [14] Deng N Y, Tian Y J. New methods in data mining: support vector machines[M]. Beijing: Science Press, 2004.
- [15] Wahba G, Ling Y, Zhang H. Margin-like quantities and generalized approximate cross validation for support vector machines//Neural Networks for Signal Processing IX, IEEE Signal Processing Society Workshop. 2002.
- [16] Evgeniou T, Pontil M, Poggio T. Regularization Networks and Support Vector Machines[J]. Advances in Computational Mathematics, 2000,13(1): 1-50, doi:10.1023/A:1018946025316.
- [17] Cholkopf B, Smola A J. Learning with kernels: support vector machines, regularization, optimization, and beyond[M]. MIT press, 2001.
- [18] Cortes C, Vapnik V. Support Vector Networks[J]. Machine learning, 1995,20(3): 273- 297.
- [19] Liang J J. Research on Several Issues of Support Vector Machines and Support Vector Description [D] Xi'an University of Electronic Science and Technology, 2009.
- [20] Kennedy J, Eberhart R. Particle Swarm Optimization//Proceeding of IEEE International conference on neural network[M]. Boston. MA: Springer, 1995:1942-1948.
- [21] Y. Da, Xiurun G. An improved PSO-based ANN with simulated annealing technique[J]. 2005, 63(1): 527-533.

Chapter 6

Conclusions and Prospects

6.1 Conclusions

This thesis studies the signals of umbilical artery blood and the collected data by applying nonlinear analysis theory and machine learning approach to identify the relationship between umbilical artery signals and fetal health status. Based on the fractal theory, the box dimension, correlation dimension and Hurst index of umbilical artery signal are investigated; the chaotic characteristics of the time series of umbilical artery signal are identified from both qualitative and quantitative perspectives; on the basis of determining the chaotic characteristics of the time series of umbilical artery blood signal, SVM method is applied to the classification of umbilical artery signal.

The following are the key findings of the research and the conclusions of this dissertation:

1. The fractal dimension of umbilical artery blood signal was calculated by the box dimension method, and the umbilical artery blood signal was proved to have fractal characteristics, and it was found that: the greater the gestational week, the greater the box dimension, and there is a positive correlation between the fractal dimension and the gestational week; the health status of the pregnant woman and the fetus can be characterized by the box dimension of umbilical artery blood signal, and the box dimension can be used as a quantitative indicator of fetal health status; the box dimension of umbilical artery blood signal can reflect the maternal blood supply to the fetus to some extent. The CD of umbilical artery blood was studied, the overall CD of normal umbilical artery blood flow signals is greater than that of abnormal signals. CD is significantly superior to conventional detection parameters in distinguishing the normality of umbilical artery blood signals. The Hurst index of umbilical artery blood signal was calculated by Lo method, and the results showed that the time series of umbilical artery blood signal had obvious self-similarity, and the characteristics of “ $1/f$ fluctuation” and non-smoothness of umbilical artery blood signal were found.

2. Chaotic phase space diagram method and Maximum Lyapunov Exponents (MLE) are used to determine the chaotic characteristics of umbilical artery blood signals from qualitative and quantitative perspectives. The attractor reconstruction of umbilical artery blood signals has been performed in Three-Dimension (3D) and Two-Dimension (2D) phase space. The results indicate that the chaotic phase diagram of the time series of abnormal umbilical artery signals show a jumbled “ball of wool” state, and the chaotic “shape” appears to converge. MLE of normal group for umbilical artery blood signals and MLE of

abnormal group for umbilical artery blood signals are calculated, which can quantitatively distinguish between normal and abnormal umbilical artery blood signals. Receiver Operating Characteristic Curve (ROC) of MLE shows that MLE is significantly superior to traditional detection parameters in distinguishing the normality of umbilical artery blood signals.

3. An artificial intelligent classification method is proposed to categorize the four states of umbilical artery blood signals, which are: normal, Oligohydramnios, umbilical cord around neck and fetal malposition. The Support Vector Machine (SVM) classifying method is constructed based on the conventional parameters, S/D, PI and RI. The particle swarm optimization (PSO)-SVM classification of umbilical artery blood with conventional parameters was constructed. BD, CD and MLE derived from Chapter 3 and Chapter 4 are used as feature parameters to construct nonlinear characteristic PSO-SVM classifying method. The results of the classification tests show that the PSO-SVM with nonlinear parameters method has higher accuracy, which is confirmed that the proposed classifying method is useful and effective.

6.2 Prospects

Although some exploratory work was done in this thesis to apply nonlinear theory and machine learning methods to umbilical artery signals, some findings were obtained, but the research is still in its early stages, and the following difficulties warrant additional study and attention:

1. The fractal characteristics of umbilical artery blood signals were only analyzed using a single-fractal analysis method, but the umbilical artery blood signals still have multifractal characteristics. Therefore, further analysis of the multifractal characteristics should be carried out.

2. The WOA-BP intelligent diagnostic model using nonlinear parameters with good generalization capability is proposed in this thesis, and further research can be conducted to construct a more extrapolative diagnostic model for umbilical artery blood with deep learning, migration learning and reinforcement learning techniques.

3. Further attempts to study the combination of umbilical blood , fetal monitoring and ultrasound based on nonlinear theory. Clinical studies have shown that ultrasound, S/D values and NST have their own strengths in fetal monitoring, and their combined application can be an important adjunctive value as an optimal method to assess fetal health. Therefore, a multifractal dimension study considering the combination of fetal heart curve and non-linear analysis of umbilical artery signal is needed to develop a new efficient fetal monitoring diagnostic model.

Acknowledgment

I would like to express my deep and sincere gratitude to my supervisor, Professor Zhongwei Jiang. This dissertation was completed under the careful guidance of my supervisor and it would not have been completed without his encouragement. My supervisor, with its profound knowledge, rigorous and realistic attitude, keen academic insight and dedication to set up a scholarly style, so I benefited a lot, and as a lifelong model to emulate. All of which will have a great impact on my future career.

I would also like to express my sincere appreciation to Prof. Xian Chen, Prof. Minoru Morita, Prof. Junji OHGI, Prof. Mamiko KOSHIBA, for being my thesis committee members and providing invaluable feedback on this dissertation. Thank you very much for your invaluable comments and suggestions to revise this thesis better.

My sincere thanks also go to my fellow labmates: Xin Han, Lurui Wang, Yunjin Zhang, who provided their help and advice during my research.

Last but not least, I would like to express my deepest gratitude to my family, my wife Jin Li and my daughter Linhao Yu, who have been my constant support and reliance in my life.